Imaging the Soultz Enhanced Geothermal Reservoir Using Double-Difference Tomography and Microseismic Data

by

Diego Alvaro Piñeros Concha

B.S., Physics (2008)
Florida Institute of Technology

Submitted to the Department of Earth, Atmospheric and Planetary Sciences
in Partial Fulfillment of the Requirements for the Degree of

Master of Science in Geophysics

at the

Massachusetts Institute of Technology

June 2010

ARCHIVES

MASSACHUSETTS INSTITUTE OF TECHNOLOGY

JUN 28 2010

LIBRARIES

© 2010 Massachusetts Institute of Technology
All rights reserved

Signature of Author.....
Department of Earth, Atmospheric and Planetary Sciences
May 21, 2010

Certified by.....
Michael Fehler
Senior Research Scientist
Thesis Supervisor

Accepted by.....
Maria Zuber
E. A. Griswold Professor of Geophysics
Department Head

Imaging the Soultz Enhanced Geothermal Reservoir Using Double-Difference Tomography and Microseismic Data

by

Diego Alvaro Piñeros Concha

Submitted to the Department of Earth, Atmospheric and Planetary Sciences on May 21, 2010 in Partial Fulfillment of the Requirements for the Degree of Master of Science in Geophysics

ABSTRACT

We applied the double-difference tomography method to image the P and S-wave velocity structure of the European Hot Dry Rock geothermal reservoir (also known as the Soultz Enhanced Geothermal System) at Soultz-sous-Forets, France. We used absolute, differential catalog and differential cross-correlation times obtained from the reservoir's September and October 1993 hydraulic stimulations along with starting event locations obtained using Joint Hypocenter Determination and Collapsing methods. The stimulations produced over 12000 microseismic events of which we chose 8930 for further analysis. We obtained high accuracy cross-correlation differential times and then performed a double-difference tomographic inversion to jointly invert for velocity structure and event locations.

It is shown through a detailed analysis of model and data residuals vs smoothing weight, ray path derivative weighted sums, and a synthetic checkerboard test that the double-difference inversion is able to produce interpretable results despite the poor source-receiver geometry employed in the study.

The results show that velocity structure for S-waves correlates well with seismicity and show the expected low velocity zones at depths between 2900 and 3600 meters, where fluid was believed to have infiltrated the reservoir. P-wave velocity structure shows less of a correlation with seismicity and shows low velocity zones at shallow depths where no water was believed to have entered the reservoir. Between 2900 and 3600 meters the P-wave velocity structure shows high velocity zones near the injection well. The results also show the NNW-SSE trend of event location clusters and velocity structure which lines up with the maximum horizontal stress orientation. Lastly, we show that using the double-difference tomographic method to relocate events produces locations that come close to rivaling those of collapsing methods.

Thesis Supervisor: Michael Fehler
Title: Senior Research Scientist

AKNOWLEDGEMENTS

This thesis and the completion of my Master's degree at MIT are dedicated to my loving mother, Georgina Pineros Concha. Her devotion to my sisters and me ensured that we became the successful individuals we are today. I truly believe that without her guidance, love, and support all these years, I would have wound up a statistic like so many of the young Hispanic males I grew up with in the poor suburbs of Austin, TX. The flaws I have are wholly of my own doing. For her undivided commitment to self-less sacrifice of health and happiness, as a single mother, to ensure my sisters and I grew up with warm beds to sleep in, healthy food on the table, and, most dear to me, her love and attention, I am eternally grateful. I hope that I can repay even a shred of what she deserves by continuing to take care of her as I have since my adolescence and by continuing on the path to becoming a better person with each passing day. I hope to someday be able to pass down what I've learned from her about the value of family and good people, doing the right thing even when much more difficult than the alternatives, and not crumbling in the face of insurmountable adversity to my own children. For everything she has done and continues to do, my sisters and I are truly blessed.

Next I'd like to thank all the mentors that I have had over the years which helped mold me as an intellectual, scientist, businessman and person including Hamid Rassoul, Joseph Dwyer, Randall Alford and Chris Frongillo at the Florida Institute of Technology and Dan Burns, Bill Rodi, Blanche Staton, Bill Aulet and Bob Dolan at MIT. While at FIT, Hamid Rassoul saw promise in me at a young age and took me under his wing. To this day I affectionately call him “Uncle Rassoul.” I am grateful for his persistence that I apply to MIT for graduate school. Joseph Dwyer,

after seeing my level of dedication to my mother, his research and to the development of his experimental apparatus, also became like an uncle to me. Randall Alford, being a fellow Texan but of Dutch heritage, had no problem quickly Dutch-uncling me. I will always cherish his appreciation of my culture, heritage, and story. Chris Frongillo provided my mom, my dogs and me shelter during the harsh 2004 hurricane season when housing was hard to come by. For his sacrifice to help us during a time of great need, I will always be thankful. Coming into MIT as a young graduate student Dan Burns helped me navigate through a maze of obstacles. His great sense of humor and light hearted way of looking at things rubbed off on me. Leaving MIT I will especially miss the long discussions with Bill Rodi about an assortment of topics ranging from higher order spectral measures to fixing broken furniture and food fights at Princeton. He helped me to weather the storm that is MIT, though he might not have realized it. Blanche Staton was also a great source of support and encouragement here at MIT. I highly recommend that all graduate students seek out her advice and expert opinion when it comes to graduate student matters and life in general. Her warm heart and dedication to students make her a valuable asset at MIT. Bill Aulet, director of the MIT Entrepreneurship Center, sets the example that the rest of professors at MIT should follow. His sincere interest in helping further his students' careers, insight and intuition with all entrepreneurial and business matters and great sense of humor, especially in lectures, sets the bar high for the rest of the faculty. As a former hiring manager, Bob Dolan helped me to better understand my talents and, as a devoted family man, reminded me of the pleasure of putting family before work. The children of these nine great individuals are incredibly lucky to have them as parents. I am lucky to have them as role models and mentors.

This work without the funding and support of my research advisor Michael Fehler would not have been possible. I thank him for his enormous patience and many teachings during the last year. It was a pleasure to have been his advisee and to have learned so much from him about seismology and geothermal energy. His commitment to helping me finish my degree despite being swamped with proposals and numerous other responsibilities as executive director of the MIT Earth Resources Lab (ERL), was admirable.

Nafi Toksöz, Rob van der Hilst, and Alison Malcolm also deserve many thanks for teaching me a great deal about seismology and for revising this thesis. Haijiang Zhang also provided much help in getting our data to work with BCSEIS and his code, TomoDD.

Next I'd like to thank my officemates with whom I shared many joyful times over the past two years including Fred Pearce, Yulia Agramakova, Mirna Slim, Di Yang, Xin Ding Fang, Nasruddin “Nas” Nazerali, Maria “Gabi” Melo, Sudhish Bakku, Bongani Mashele, and Alexander Evans. Fred Pearce was also my roommate for most of my time here at MIT and I owe him much for my quick acclimation to Boston and MIT. He was the big brother I never had. I will always cherish cooking Lebanese food with Mirna, sailing (when he didn't capsize the Tech Dingy we were on) and skydiving with Sudhish, dancing and learning about Russia with Yulia, discussing current events and philosophy with Nas and Bongani, watching concerts and stand-up comedians with Gabi, doing pull-ups and running with Alex, and bantering with Di and Xin Ding. I am grateful to Dale Morgan for bringing most of us together in a research field trip to the Caribbean island of St. Lucia during IAP 2009. I will miss them all dearly.

My friend Susan Kennedy and her lovely family also deserve a mention. Their

friendship gave me a great deal of fortitude and joy during my time here in Boston, while I was far away from my own family. They reinforce my admiration for tightly-knit country families.

I'd also like to thank the ERL and EAPS administrative staff. In the ERL. I thank Sue Turbak and Marcia Taylor for all their support. They do the behind-the-scenes, "dirty" work that makes the ERL so successful. I will miss conversations with Sue about family, gardening, and New England. Carol Sprague, Vicki McKenna, Roberta Allard, Jacqueline Taylor and the rest of the EAPS administrative staff deserve a big thanks as well. They've been a great source of help on all EAPS and MIT matters. I will especially miss the conversations with Carol about her boys, her grandkids, and fun things to check out around Boston and with Roberta about her motorcycle and her family. I wish them and their families the very best and thank them from the bottom of my heart for helping enrich my experience at EAPS.

Collectively, the authors acknowledge the GEIE Exploitation Minière de la Chaleur (Kutzenhausen, France) for giving us permission to use the Soultz data. We thank Roy Baria and Ernie Majer for providing the data and Hiro Asanuma for providing the Tohoku University event locations.

TABLE OF CONTENTS

CHAPTER 1

INTRODUCTION

1.1 Introduction

The September and October 1993 stimulations of the Soultz Enhanced Geothermal System (EGS) reservoir (also known as the European Hot Dry Rock geothermal reservoir) at Soultz-sous-Forets, France with 45000 m^3 of water, at a depth of approximately 3000 meters, resulted in over 12,000 microseismic events (also known as micro-earthquakes) that were recorded by a four station down-hole seismic network and subsequently located using a one-dimensional velocity model obtained from calibration shots. These micro-earthquakes provide a wealth of information about the processes that accompanied the stimulation (see e.g. Evans *et al.*, 2005). Here we apply double-difference tomography developed by Zhang and Thurber (2003) to jointly determine the spatial variations in velocity within the reservoir as well as relocate the microseismic event locations.

Block *et al.* (1994) developed a tomography imaging approach that used absolute arrival times of events recorded at the Fenton Hill Hot Dry Rock reservoir to determine the spatial variation in P and S-wave velocities within the reservoir and simultaneously determine locations of the microseismic events. They found the resulting image of S-wave velocity variation was reliable and showed a decrease of velocity of approximately 13% within the most fractured portion of the stimulated reservoir. They argued that the P-wave velocity image was unreliable due to the relatively smaller changes in P-wave arrival times that result from changes in P-wave velocity.

Double-difference tomography has advantages over conventional

tomographic schemes in that it uses absolute arrival times in addition to relative arrival times of events recorded at common stations. Relative arrival times can be reliably determined using cross-correlation. The use of relative arrival times for events that are located close to each other helps to minimize the effects of unmodeled variations in geological structure along common portions of the ray paths propagating between the events and the station. These unmodeled paths occur at locations near the stations where tomography has poorer resolution. The double difference approach allows the velocity variations within a zone of seismicity to be well determined even if the variations outside the zone are poorly known. Thus, the double-difference approach provides an improved capability for application to EGS stimulations where monitoring stations are located well outside the reservoir. Another study using the Zhang and Thurber (2003) double-difference tomography method was performed on data from the 2003 hydraulic stimulation at the Soultz EGS site (Charlety *et al.*, 2006) which involved the use of a surface array of sensors and a deeper injection than performed in the 1993 stimulations. That study found that using the method of Zhang and Thurber (2003) produced a good model resolution compared to a standard tomography approach also employed in that same study but on the 2000 hydraulic stimulation data.

1.2 1993 Soultz EGS Experiment

The 1993 stimulations at Soultz consisted of the injection of 45,000 m^3 of water into an open-hole section of the GPK1 well at depths between 2850 and 3550 meters. Evans *et al.* (2005) show that, during the first stimulation in September, which produced a majority of the events, the fluid entered the formation through a number of natural fracture zones that had evidence of hydrothermal alteration.

Their interpretation of the seismic energy release and the pattern of locations of the microseismic events, using a suite of microseismic analysis methods, temperature and spinner logs, is that a major structure appearing to be a flow path extends downward from the injection zone at about 2950 m, shown in Figure 11 of Evans *et al*. (2005).

Figure 3 and 7 of Evans *et al.* (2005) show the well logs (spinners, UBI and others), injection rates, flow profile, pressure, degree of alteration, pre and post-stimulation fractures, and fracture density for the entire open-hole depth of GPK1. Figure 3 from Evans *et al.* (2005) is reproduced here as Figure 1.1. Figure 1.2 shows a plan view of all four seismic stations, GPK1, and the starting Joint Hypocenter Determination (JHD) event locations obtained from Tohoku University.

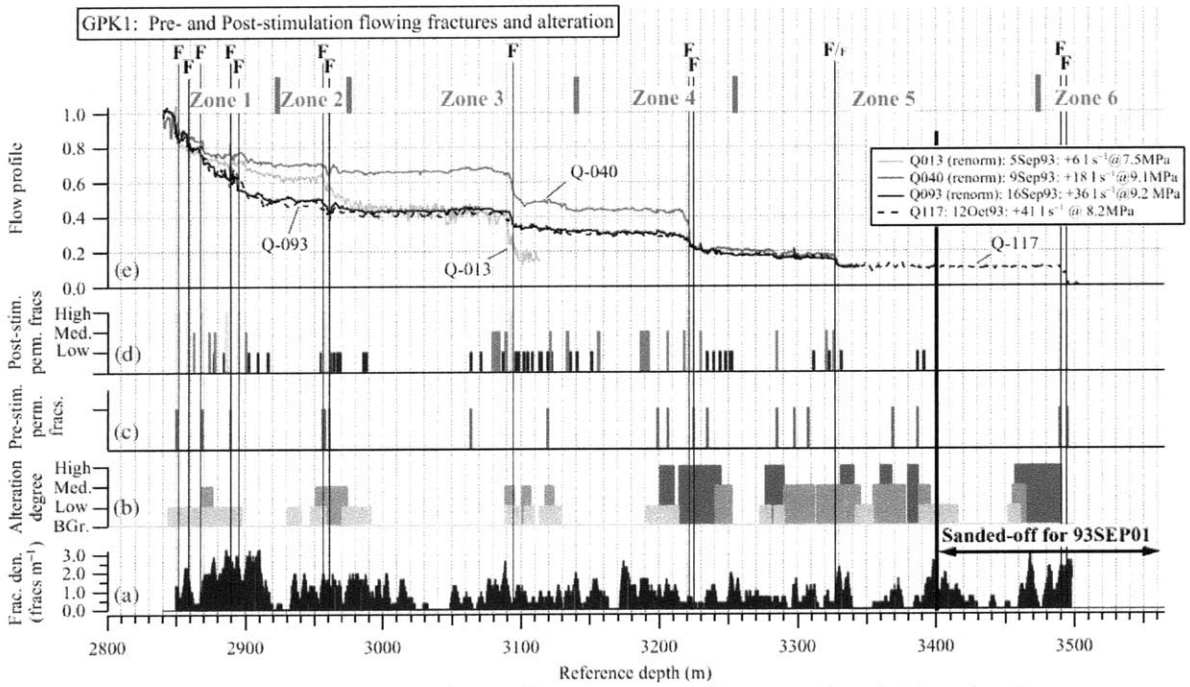

Figure 1.1: Flow profile (from spinner logs), pre and post-stimulation fractures, alteration degree, and fracture density plotted from 2800 to 3600 meters depth for the September 1993 Soutlz EGS hydraulic stimulation, from Evans *et al.* (2005).

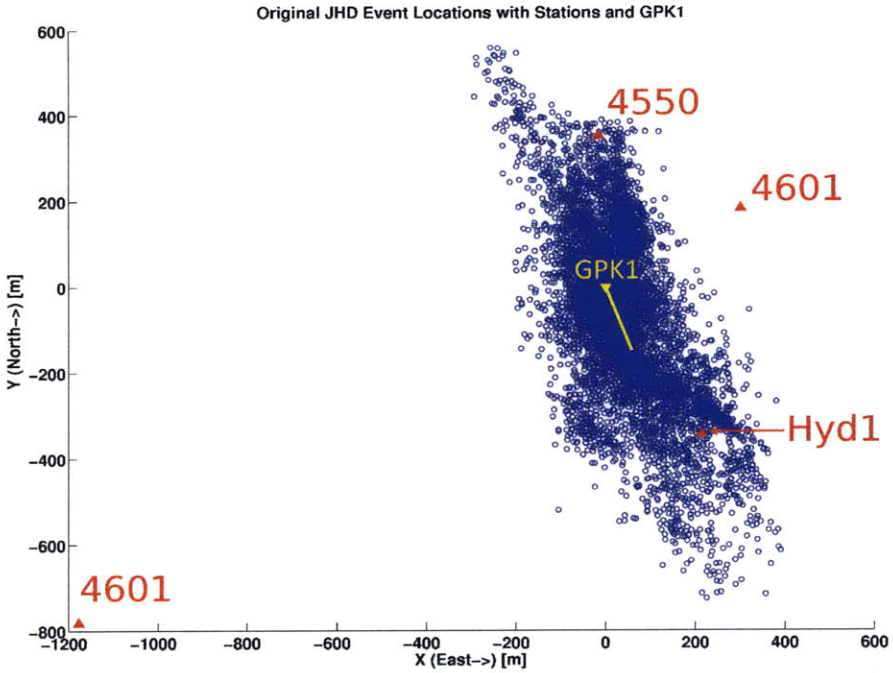

Figure 1.2. Plan view map showing locations of the four seismic stations (red triangles), the injection well GPK1 (yellow triangle), its superimposed path through the reservoir (yellow line) and the 8930 initial JHD event locations used in this study (blue circles).

According to Baria *et al.* (1999) the crystalline basement begins at 1355 meters for the injection well GPK1 with a temperature, at that depth, of 140.3° C. They explain, from temperature logs, that the temperature gradient is 10.5° C per 100 meters within the sedimentary cover and on average 2.3° C per 100 meters in the granite basement. The temperature gradient increases from 1.5° C per 100 meters at 2350 meters depth to 3° C per 100 meters at 3800 meters depth, which suggests to Baria *et al.* (1999) the presence of convective cells between the granite and sedimentary layers. This conclusion agrees with hydrothermal alteration noted by Evans *et al.* (2005).

From a regional perspective, the reservoir is in the Rhine graben which, according to Baria *et al.* (1999), is part of the Western European rift system that

extends North-South between Mainz in central Germany to Basel in Switzerland. Figure 1.3, borrowed from Evans *et al.* (2005), gives an overview of the location of the reservoir on the regional scale.

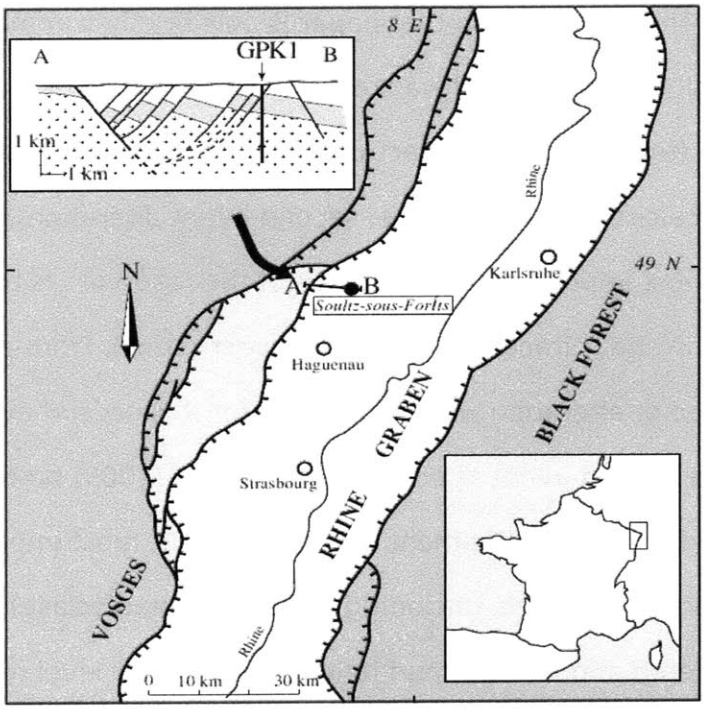

Figure 1.3: Regional overview of location of Soultz EGS reservoir from Evans *et al.* (2005). Upper left inset shows a cross-sectional view from A-B with GPK1 and the main geologic sections (granite denoted by crosses, Mesozoic sediments in light gray, and Oligocene and Miocene sediments in white). Lower right inset shows the location of the expanded view relative to France.

The boreholes used for the four stations were old oil wells. They were extended in depth in order to deploy the receivers in basement rock. GPK1 was also extended from 2000 to 3600 meters in 1993, before the stimulation experiment was performed. GPK1 had a 7 inch well casing and a 6.25 inch open-hole from 2850 to 3600 meters during the 1993 stimulation (Baria *et al.*, 1999).

Baria *et al.* (1999) report that the maximum horizontal stress (a function of

depth between 1458 and 3506 meters) is less than the vertical stress and is oriented N 170° E which agrees with the trend of the prominent joint structures in the reservoir.

Evans *et al.* (2005) show that three distinct hydrothermal events altered the granite at Soultz. The discussion in that paper is now briefly summarized. The first slightly affected all the granite and was related to the cooling of the pluton. It produced mode 1 (tension), narrow fractures (therefore with high aspect ratio) filled with chlorite and calcite. The second (i.e. second-event alteration), which Evans *et al*. (2005) say is most important to the studies of the reservoir, is the result of fluid flow and resulted in shear fractures (with low aspect ratios). From analysis of limited cuttings the degree of alteration was established for this second event, as shown in Figure 1.1. For the second-event alteration Evans *et al*. (2005) propose three levels of alteration based on the development of clay minerals, most importantly illite, and the removal of primary minerals (including biotite and plagioclase). In the lowest level, biotite is altered and transformed to illite. At the next level (considered the moderate alteration grade) biotite and plagioclase are in the process of transformation to illite. Lastly, in the highest level of alteration biotite and plagioclase are completely transformed to illite with quartz deposits in some places. As shown in Figure 1.1, moderate to high alteration occurred to rock deeper than 3200 meters depth with less occurrence at shallower depths. The third event alteration is related to haematite deposition near the top of the granite.

Evans *et al*. (2005) and Baria *et al*. (1999) summarize the detailed discussion by Dyer *et al.* (1994) regarding the hydraulic experiment carried out in September and October of 1993 at Soultz. Before that time a packer test, in which all but 30 meters of open-hole was blocked from water exposure by use of expanding packers,

was performed in August of 1993 in order to link existing fractures to the borehole of GPK1. This test only produced 203 microseismic events (Dyer *et al.*, 1994). The first open-hole test was performed from the 1st to the 22nd of September and involved sanding the bottom of the borehole up to 3400 meters depth leaving an exposed open-hole from 2850 to 3400 meters depth. Dyer *et al.* (1994) explain that the injection consisted of twelve steps, each lasting 48 hours, of increasing injection flow rate starting from 0.15 liters per second and increasing up to 36 liters per second. Figure 3.3 of Dyer *et al.* (1994) shows the injection rate over the entire course of this stimulation. Over 18000 events were produced in this period alone with microseismic activity beginning at an injection pressure of 6 MPa. Events initially clustered near the borehole and then expanded outward over time and eventually grew along a NW-SE direction. They report that the majority of the microseismicity occurred near the top of the open-hole (between 2850 and 3000 meters depth), which is consistent with the pre-stimulation fault locations. Also, 25,000 cubic meters of water were injected during this test.

From October 1st to the 15th a second packer test was performed in order to stimulate a natural fracture zone between 3480 and 3485 meters depth. To do this some sand was removed from the bottom of GPK1 and two expansion packers were installed in the well. This second packer test only produced 92 microseismic events and had to be stopped as it was believed that the expanding packers failed, allowing water to permeate into the reservoir at shallower depths.

The second open-hole test was conducted from October 11 to the 21st in order to further stimulate the reservoir between 3480 and 3485 meters depth. In this stimulation the injection flow rate was increased to 41 liters per second and then sustained for four days. At the end of the fourth day the injection rate was increased

to 50 liters per second and sustained for 24 hours. A total of 20,000 cubic meters of water were injected during this test and 1954 microseismic events were produced. Microseismicity began at about 7-8 MPa. Initially, most of the seismicity was detected at the bottom open-hole section between 3342 and 3500 meters depth, despite spinner logs showing that only 10% of the water entered the rock mass at these depths. After 3.5 days the upper portion of the open-hole section became active again suggesting to Dyer *et al*. (1994) that the previously stimulated areas had to be re-pressurized in order for further shearing to occur. After this, the same NW-SE trend in microseismicity was observed.

In 1994 two tests were performed to further understand the effects of the September and October 1993 stimulations. Evans *et al.* (2005) discuss and interpret the findings of these tests.

1.3 Thesis Outline

In Chapter 2 of this thesis we discuss the methods used to process and analyze the microseismic event data, produced by the September and October 1993 stimulations, using the double-difference method of Zhang and Thurber (2003). In Chapter 3 we show how an interpretable set of results was selected from four principle sets which we obtained. Then we interpret this selected set of results. In Chapter 4 we summarize our findings and suggest future work that can be done to extract more information about the stimulated flow paths of the Soultz EGS reservoir. Additionally, an appendix is included with the four principle sets of tomographic and event relocation results.

CHAPTER 2

METHODOLOGY

2.1 Introduction

The Soultz data set was processed in a number of steps to get the final tomographic results. The steps are listed and then explained in more detail. First the data were converted to a binary format for ease of analysis and storage efficiency. Next we reduced the size of the data set by selecting high quality events that had a minimum number of phase picks. Trace data were filtered and passed through a cross-correlation package to obtain relative arrival times between event pairs at common stations for later use in the double-difference tomography. Next, relative arrival times were calculated using the absolute arrival time catalog (i.e. phase picks) for both P and S arrivals. Lastly, the relative arrival times from both the cross-correlation and from the catalog of phase picks, along with a catalog of absolute arrival times were used to perform double-difference tomography inversion. The major steps are now described in more detail.

2.2 Data Preparation

We obtained seismic waveform data recorded during the September and October 1993 hydraulic stimulations of the Soultz EGS reservoir. This dataset contained over 12000 microseismic events. Figures 2.1 and 2.2 show the time distributions of both the entire data set (12000 plus events) and the down-selected data set (8930 events) described later on in this chapter. Note the gap in data between Julian days 259 and 266 for both figures. This gap was not explained by Dyer *et al.* (1994) as the sensors were operational during this period of time.

Only about ten percent of the data were from the October stimulation. The data were recorded by three four-component stations (4550, 4601, and 4616) and a single-component hydrophone (Hyd1). Figure 2.3 shows a plan view of the station locations. Note that the stations (i.e. receivers) are down-hole in order to make contact with the granite basement. The purpose of using four-component sensors was to give data redundancy and enhance the identification of shear waves (Dyer *et al.,* 1994). Each sensor contained four components equally oriented in space with an angular spacing of 109.47 degrees and one of the four components aligned with the vertical, forming a tetrahedral geometry as shown in Figure 2.4. The three subhorzontal components allowed for easier detection of S waves for most events (Dyer *et al.*,1994). Additionally, if one component failed or was determined to produce unreliable measurements an orthogonal set of three components (N,E,depth) could be recovered from the remaining three (Dyer *et al.*, 1994; Jones and Asanuma, 1997). The single-component hydrophone could only measure P-waves including direct P-waves and P-waves transformed from S-waves that scattered off the well-bore.

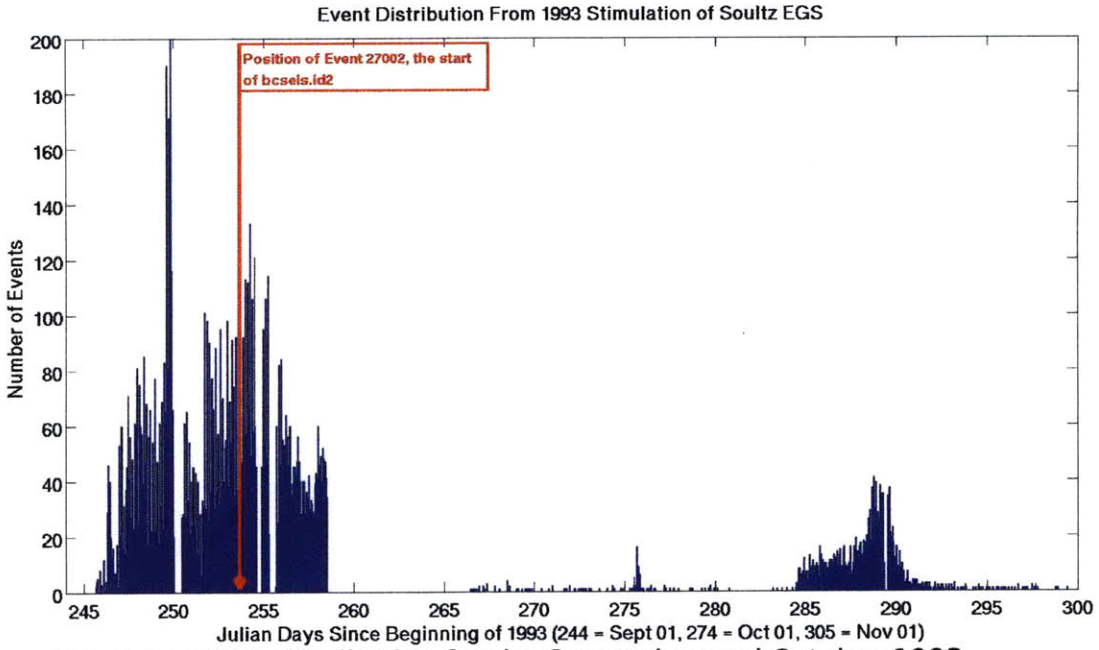

Figure 2.1. Event-time distribution for the September and October 1993 stimulations of all 12000 plus events. Note the gap in the data from Julian days 259 to 266 despite no sensor downtime during that period.

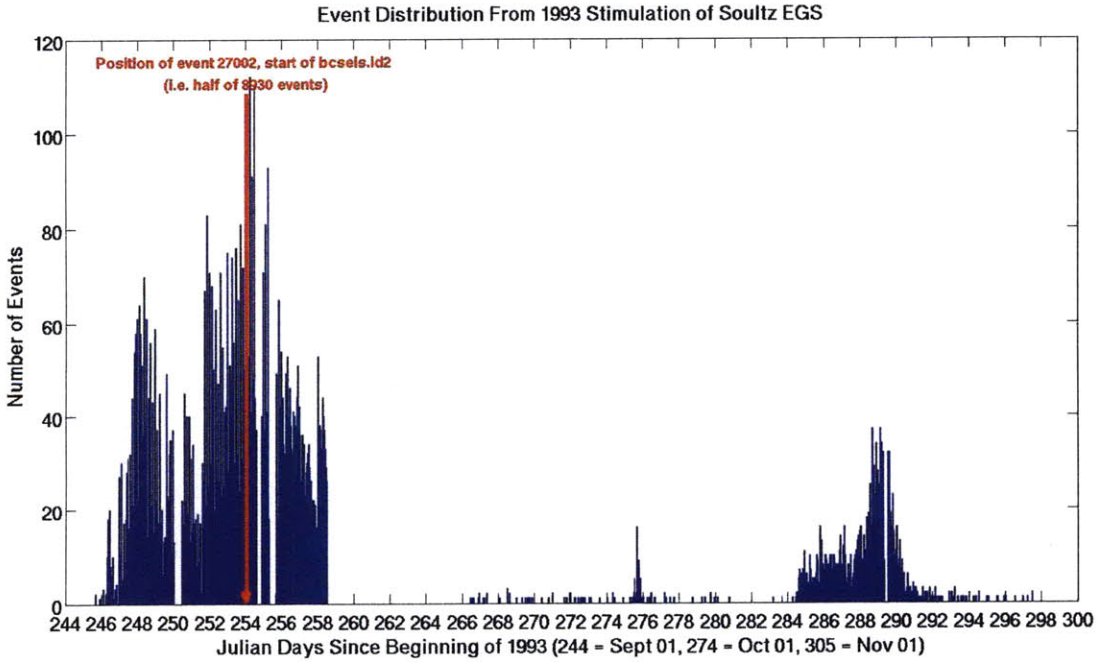

Figure 2.2. Event-time distribution for the September and October 1993 stimulations of the 8930 high-quality events. Note the gap in the data from Julian days 259 to 266 despite the sensor array being operational during that time period.

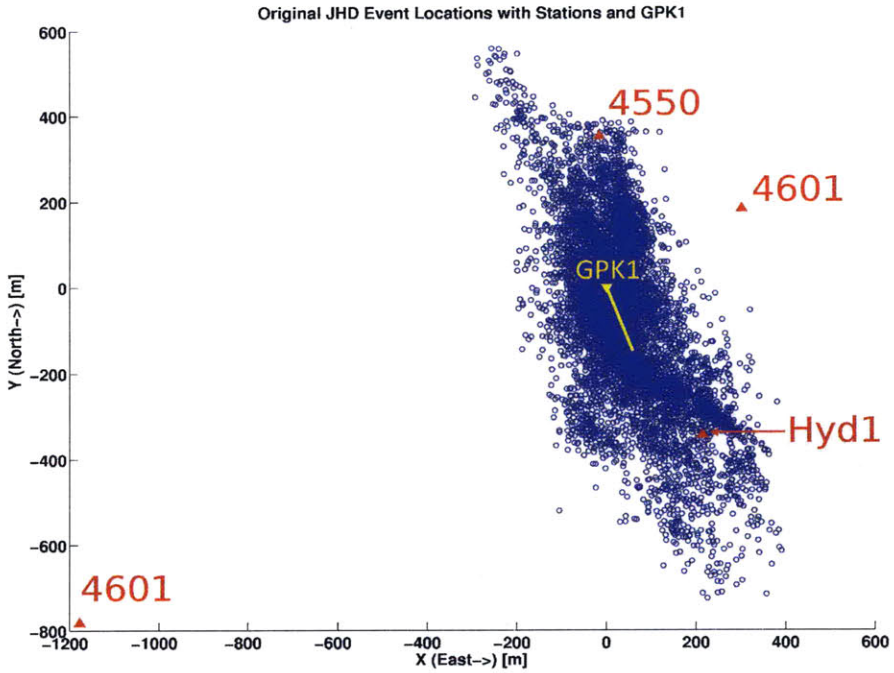

Figure 2.3. Plan view map showing locations of the four down-hole stations (red triangles), the injection well GPK1 (yellow triangle), its superimposed path through the reservoir (yellow line) and the 8930 initial event locations used in this study (blue circles).

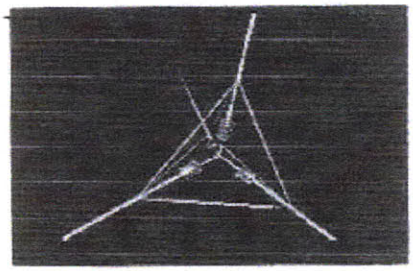

Figure 2.4. This diagram, from Dyer *et al.* (1994), shows the tetrahedral sensor configuration of the four-component stations.

2.2.1 Changing the Data Format

The data were obtained in ASCII format with each file containing data from one station for an individual event. Files were organized into folders by station. Each event file, for a given station, started with a header containing event information (e.g. arrival times, start of recording date and time, hypocenter, etc...) followed by

four columns of time series (one for each of the station's sensor components) sampled at 5000 Hz. This format was cumbersome to use and required a large amount of storage space. To facilitate ease of use and storage efficiency the data were converted to the Seismic Analysis Code (SAC) binary format. Refer to Goldstein *et al.* (2003) for further details on SAC. The headers were assimilated into a single catalog file for all events and each trace was saved into its own SAC file with embedded header information. The folder structure was also simplified. Initially the root folder contained four folders (one for each station) each of which contained over 12000 folders for the events. The folders were merged to yield a total of 12000 folders (one for each event) in a single root directory with traces for all stations included within each folder. Each folder ultimately contained thirteen trace files (12 for the four component stations and a single trace file for the hydrophone).

2.2.2 Down-selecting the Dataset

Once the data were in an easy to use format it was necessary to reduce the set as some events had large arrival time uncertainties or had missing P and S picks on some traces. The three four-component stations produced up to 2 picks per trace (P and S phases) and the hydrophone produced at most a single P pick, resulting in a maximum of seven picks per event. Events that did not contain those seven picks were removed from further analysis. Dealing with the large location uncertainties required more work and is explained next.

The large uncertainties resulted from a combination of poor or missing picks and low signal-to-noise ratios in the time series so it was necessary to do a statistical analysis to remove these events. The original ASCII files did not include locations or origin times. We obtained event locations from Tohoku University, who

employed a Joint Hypocenter Determination (JHD) method followed by a collapsing approach (Jones and Stewart, 1997) to refine the locations. Tohoku University did not provide event origin times. We estimated an origin time for each pick from the locations provided for all events. The root mean square error (RMSE) of origin time was determined by applying Equation 2.1.

$$RMSE=\sqrt{\frac{(\sum t-\bar{t})^2}{N-1}} \tag{2.1}$$

From plotting histograms of RMSE for all events located within 100 m depth intervals an appropriate cutoff RMSE was chosen which would contain a distribution of events for all depths within the reservoir and remove poor quality outliers. Figure 2.5 shows a typical distribution of RMSE for all events within a given depth interval and Figure 2.6 shows a zoomed version of the same plot. From both figures it is clear that choosing 50 ms as the RMSE cutoff eliminates events that may have RMSE that differ significantly from the majority of the events. However further analysis was done to ensure this indeed would be a good choice.

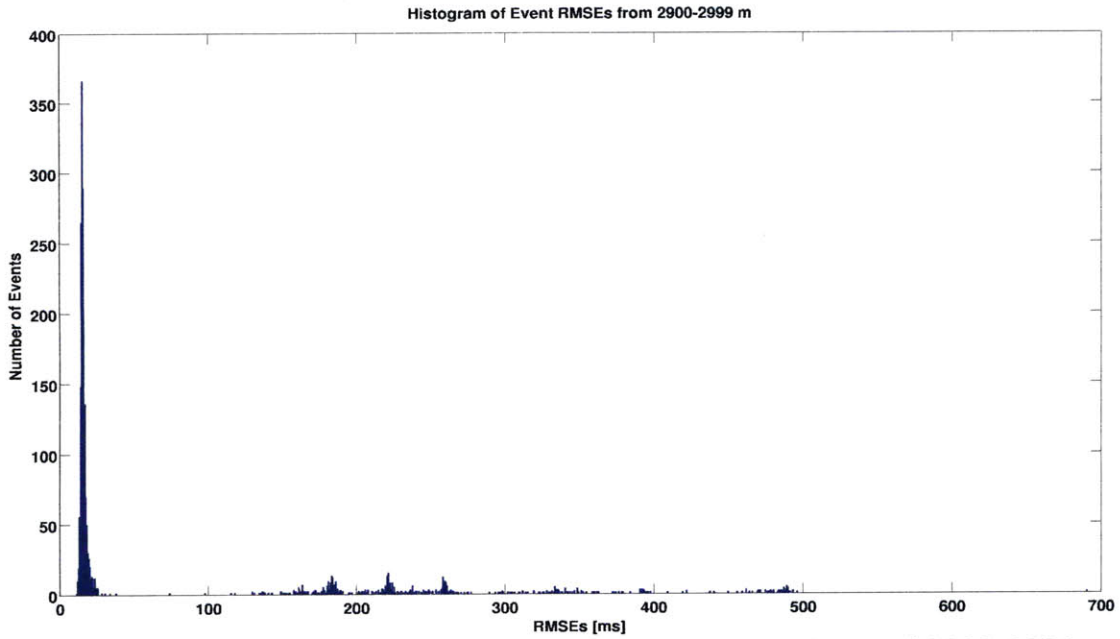

Figure 2.5. RMSE distribution for all events within the depth interval 2900-2999 meters. Histograms like this were used to choose an appropriate RMSE cutoff to remove low quality events.

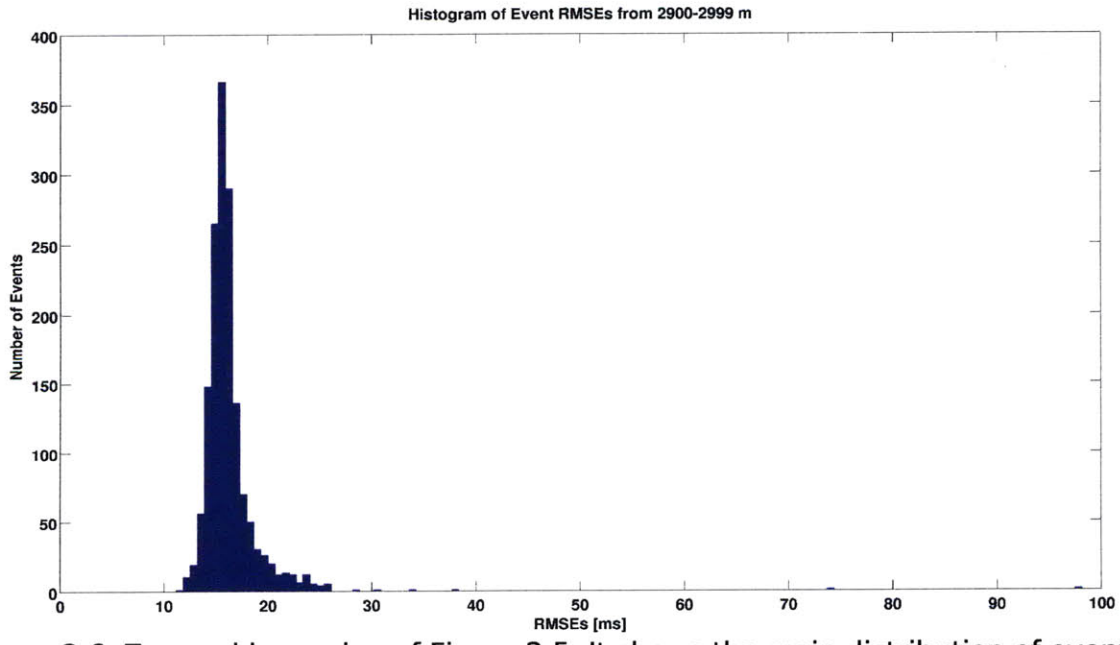

Figure 2.6. Zoomed in version of Figure 2.5. It shows the main distribution of events based on their RMSEs.

When choosing an appropriate RMSE cutoff, it was also important to note two things, how the main distribution shifted along the RMSE axis with increasing depth and also the desire to maintain a uniform distribution of events in three-dimensional space to provide good coverage for the tomography. The RMSE is expected to increase with increasing event depth because rays from events that are deeper in the reservoir propagate through the shallower portion of the reservoir that has heterogeneity that is not accounted for in the initial homogeneous velocity model. To illustrate how the distribution changed location on the RMSE axis with increasing depth, histograms and plots of mean and median RMSE per depth interval were examined. From the histograms it was clear that the main distribution shifted to higher RMSE values as depicted in Figure 2.7. This was also expressed in the plot of median RMSE versus depth, but not so clearly in the plot of average RMSE versus depth due to the presence of outliers. Figure 2.8 shows how the median RMSE changed with increasing depth. Figures 2.9 and 2.10 show the median RMSE per 100 meter depth interval for the September and October stimulations accordingly. Note that the plots of median RMSE contains some large values at shallow depths that go against the trend at deeper depths. We believe this is due to the smaller number of events at these shallow depth intervals. The trend is important because choosing a cutoff RMSE solely based on an assessment of shallow depth intervals could result in a partial or substantial cutoff of the main distribution of events at greater depths. To further illustrate this, we looked at the spatial distribution of events using an aggressively low cutoff RMSE of 16 ms and the conservative 50 ms cutoff RMSE. It's clear from looking at the distribution of events in Figure 2.11 that deeper events were removed by using the smaller cutoff RMSE while the distribution of shallower events remained on par with using the conservative cutoff

RMSE. Also note that using the 16 ms cutoff RMSE resulted in 4625 events while using the 50 ms cutoff RMSE resulted in 8930 events spanning both the September and October stimulations so a substantial number of events were removed by using the 16 ms cutoff. As a result of this analysis we decided to go with the 50 ms RMSE cutoff. Refer to Figure 2.2 to see the time distribution of the 8930 events.

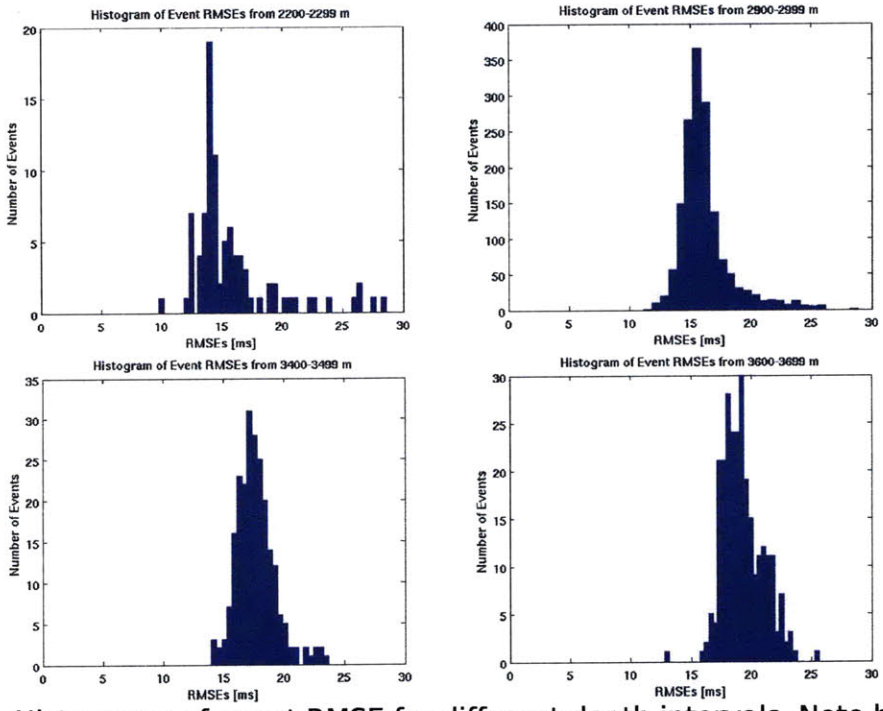

Figure 2.7. Histograms of event RMSE for different depth intervals. Note how the center of the main event distribution shifts towards higher RMSE with increasing depth.

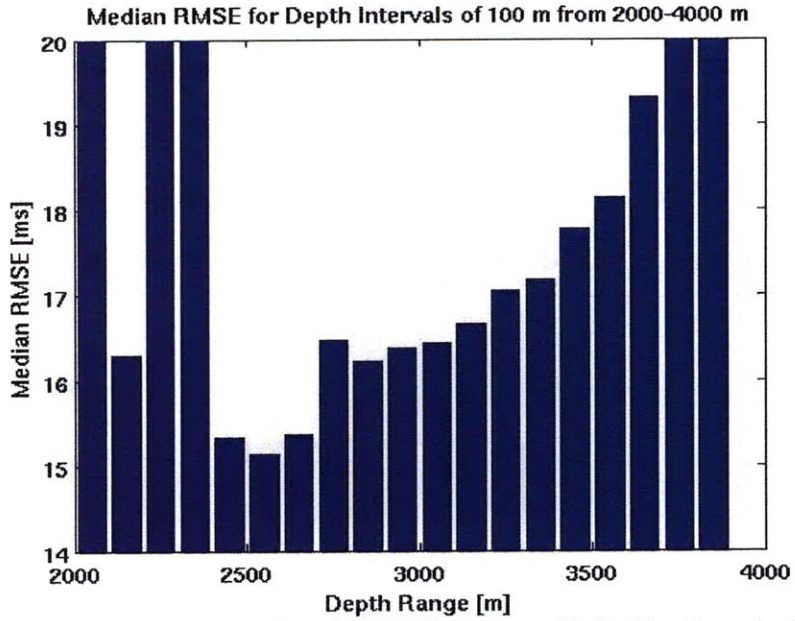

Figure 2.8. Median RMSE versus depth for all events. Note the trend of increasing median RMSE with increasing depth. Discrepancy in trend from 2000 to 2400 meters caused by outliers.

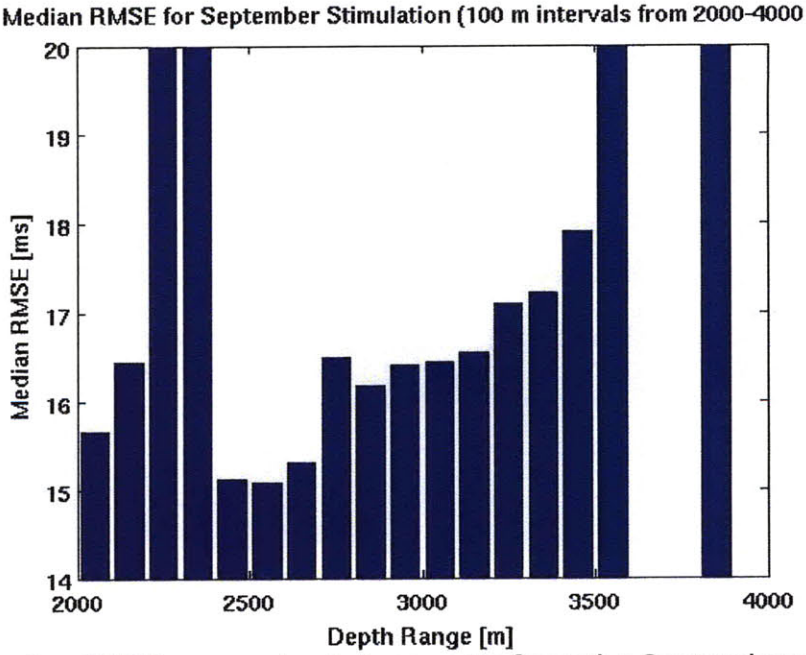

Figure 2.9. Median RMSE versus depth for events from the September stimulation. Note the trend of increasing median RMSE with increasing depth. Discrepancy in trend from 2000 to 2400 meters caused by outliers. Also note the absence of events between 3700 and 3900 m.

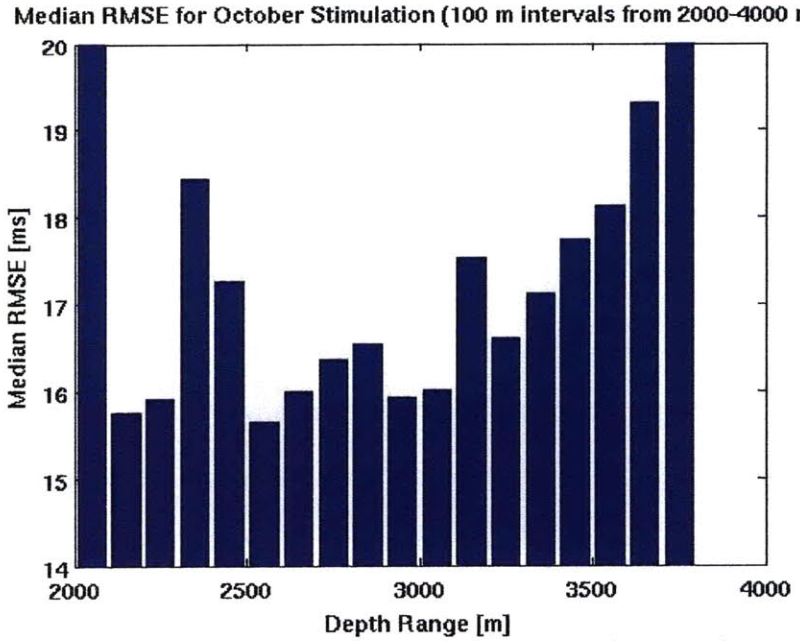

Figure 2.10. Median RMSE versus depth for events from the October stimulation. Note the trend of increasing median RMSE with increasing depth. Discrepancy in trend from 2000 to 2400 meters caused by outliers.

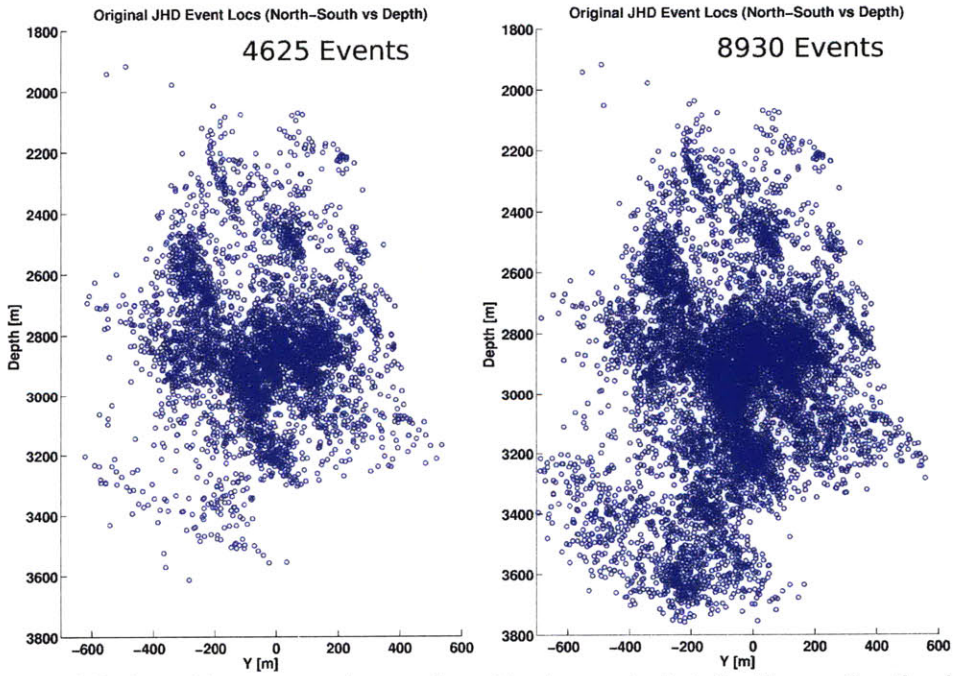

Figure 2.11. Side-by-side comparison of vertical event distributions. On the left is the distribution resulting from using the 16 ms cutoff RMSE and on the right is the distribution resulting from using the 50 ms cutoff RMSE. Note that a majority of deeper events are eliminated by using the 16 ms cutoff.

2.2.3. Filtering the Data

Traces from the 8930 event dataset were filtered to enhance the signal-to-noise ratio. This filtering would also help in the cross-correlation process detailed in the next section. A causal Butterworth band pass filter was chosen due to its uniform sensitivity over the pass band and since fast roll-off beyond the cutoff frequency was not important (Butterworth, 1930). Note that using this type of filter can affect the absolute times by producing a time shift. However, all the absolute times would be shifted in the same fashion so there would be no effect on the differential times. Using the amplitude spectrum of typical signals, the corner frequencies were chosen. Figure 2.12 shows the time series for the vertical component of a typical event in the down-selected data set. Note the prevalence of low frequency ringing in the trace for station 4601. We do not know the exact source of this ringing but guess it might be associated with the alternating current frequency in Europe of 50 Hz. The effects of this ringing can be seen in the larger amplitude spectrum at lower frequencies compared to the traces recorded at other stations and in the higher average value of correlation coefficients compared to the other stations, discussed below. Also note that the ringing on station 4601 affects the majority of events in our data set. Figures 2.13-2.16 show the amplitude spectrum of the vertical components of station 4550, 4601, 4616 and hyd1 for event 41256, a typical event. Note how the spectra (except for 4601) begin to roll-off between 1000-1500 Hz. This is due to the anti-alias filter used before digitizing (Dyer *et al.*, 1994). The frequencies of 20-500 Hz were chosen for the band to be kept. A fourth-order Butterworth filter was applied to the data in SAC and the resulting time series are shown in Figure 2.17 for the same event as before. Compare Figure 2.17 with Figure 2.12 and note the reduction of high frequency

noise but the continued presence of the low frequency ringing in the trace from station 4601. Using a frequency larger than 20 Hz for the low end of the bandpass filter did not seem to remove the ringing without removing a lot of the signal as well since this event has low signal-to-noise ratio. Filtering for this event had little effect on traces at stations 4550, 4616 or hyd1.

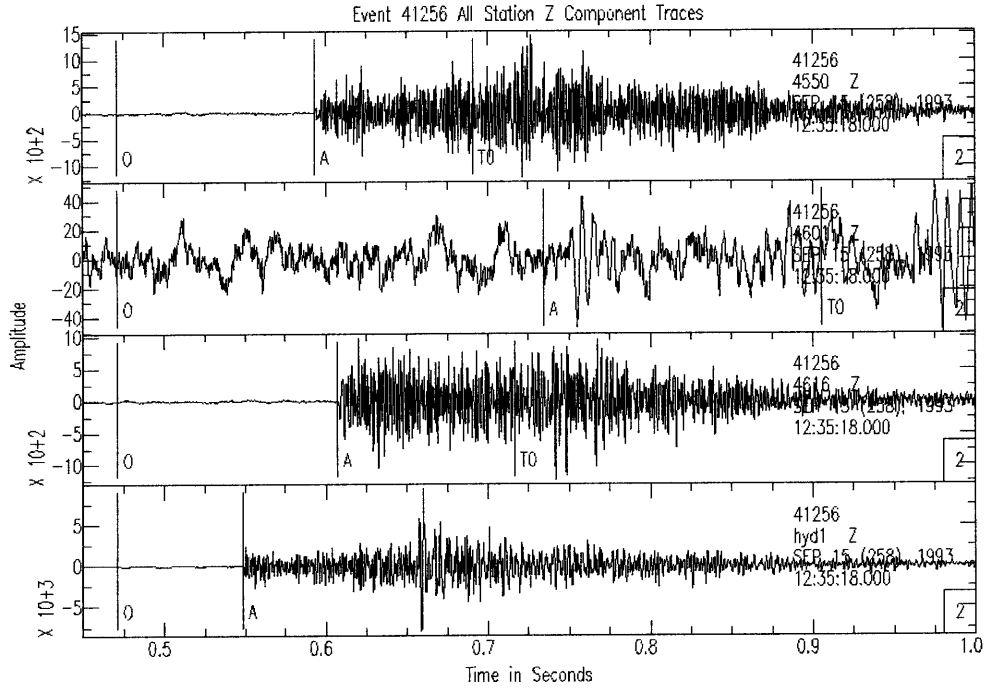

Figure 2.12. Time series plots for the vertical component traces of a typical signal without filtering ordered top to bottom by station (4550, 4601, 4616, hyd1).

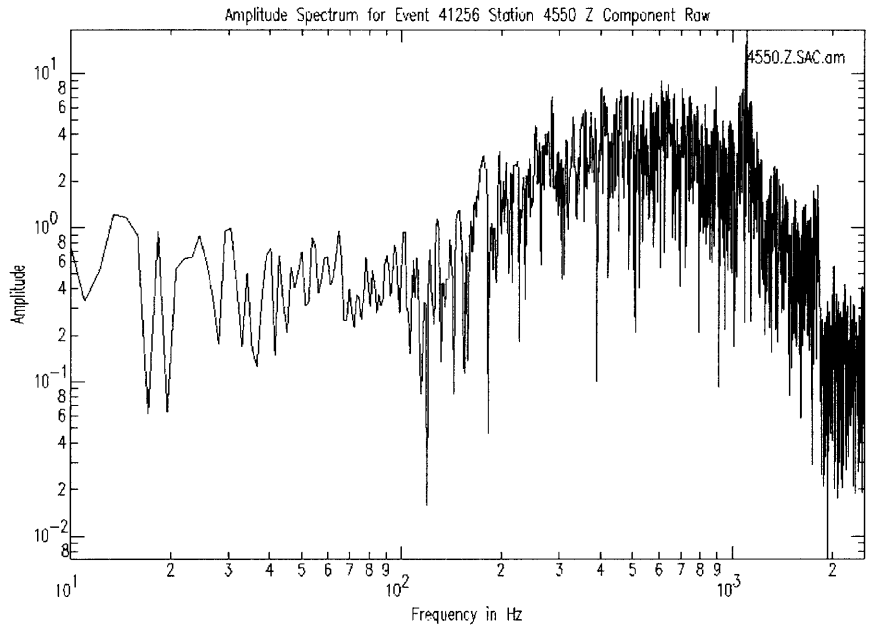

Figure 2.13. Amplitude spectrum of the unfiltered vertical trace of station 4550 for event 41256.

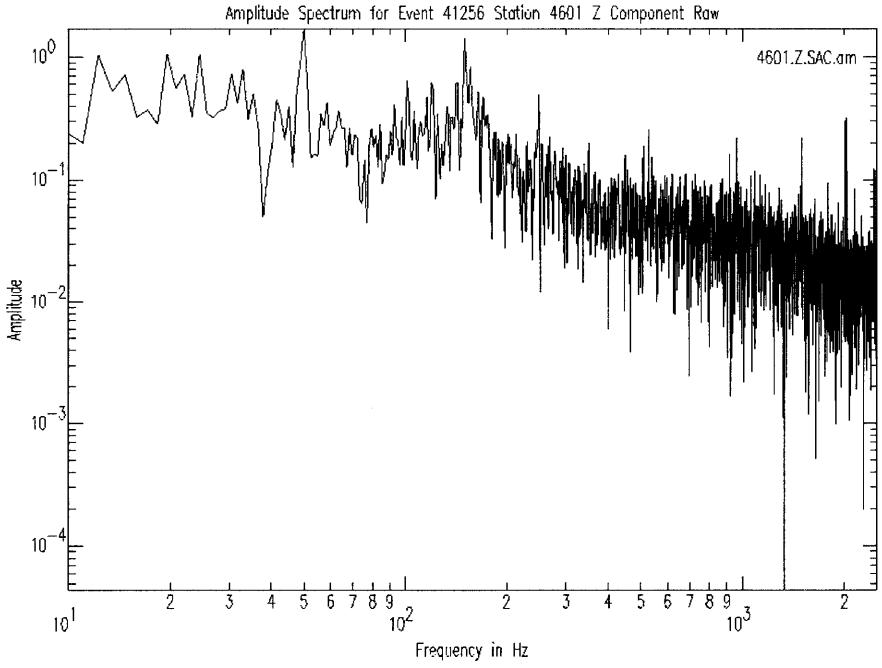

Figure 2.14. This is the amplitude spectrum of the vertical trace for station 4601 of event 41256. Note how no clear roll-off is present and how different the shape is compared to the other spectra figures. Note that the peak at 50 Hz might be the source of the ringing.

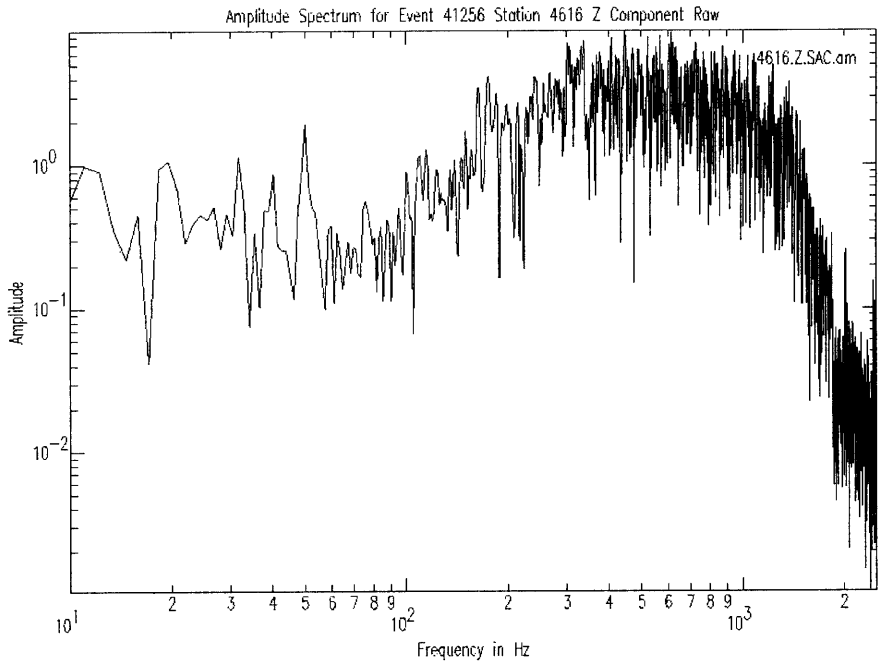

Figure 2.15. This is the amplitude spectrum of the vertical trace for station 4616 of event 41256.

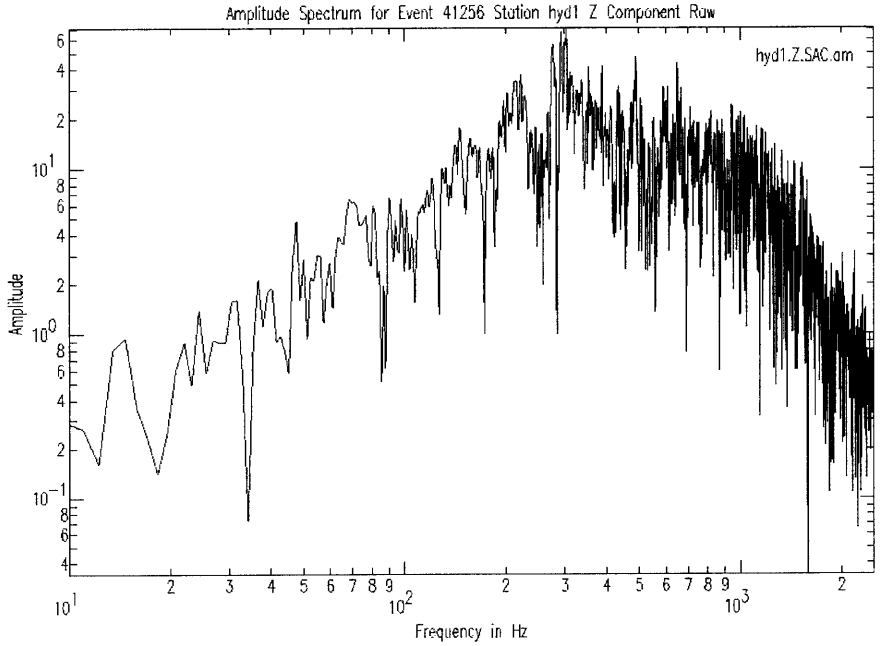

Figure 2.16. This is the amplitude spectrum of the vertical trace for station hyd1 of event 41256.

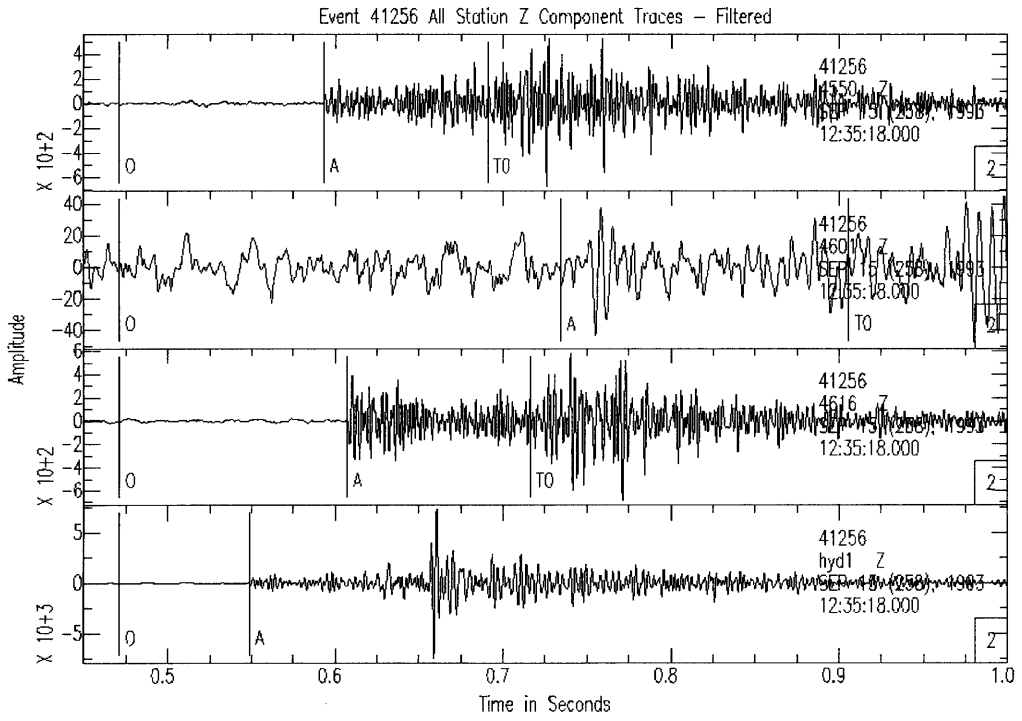

Figure 2.17. Time series plots for the vertical component traces of a typical signal after applying a forth order Butterworth band-pass filter (20-500 Hz).

2.3 Cross-Correlation Using BCSEIS

We used BCSEIS, a package written by Du *et al.* (2004), which performs both bispectrum cross-correlation (BS), and standard cross-correlation (CC) calculations to obtain relative arrival times (i.e. delay times) for event pairs record at common stations. This code was chosen because of its ability to suppress both Gaussian and non-Gaussian correlated noise sources from waveforms recorded at common stations and its previous results showing improved relative arrival times over standard CC methods. To elaborate, this code performed the standard CC technique on the band-pass filtered data described above and the BS method on both unfiltered and filtered waveforms for events with epicenters within 500 meters of each other. The results from the BS method were then used as a means to reject or

accept the CC relative time. This methodology has been shown to produce results with smaller RMS residuals (Du *et al.*, 2004). The resulting relative times were then used in the tomography code.

2.3.1 BCSEIS in Detail

In order to understand the bispectrum method, a short discussion of higher order spectra (HOS) and the statistical measures used to describe a signal's probability distribution, is necessary. McLaughin *et al.* (1995) give a good overview of HOS which we used to formulate the following discussion.

In signal processing, a signals probability distribution function (PDF) is determined by treating the signal's values at all sampling points as a population of measurements in order to generate a histogram showing the frequency of occurrence of the values in the population of measurements. Different statistical measures, called moments, have been developed to characterize the PDF. The first order moment of a signal X(t) in the time-domain is the signal's mean value μ^1 (i.e. population mean) determined by applying the expectation operator E{} to the signal.

$$\mu^1 = E\{X\} \tag{2.2}$$

The second-order moment, in the time-domain, is known as the autocorrelation function (ACF) μ^2 of the signal.

$$\mu^2 = E\{X(t) \cdot X(t+t1)\} \tag{2.3}$$

Note that t1 in μ^2 is simply a time shift. Also note that the second-order moment is related to the signal's variance σ^2. For zero-mean signals (i.e. signals with $\mu^1 = 0$), the second order moment is equal to the signal's variance σ^2.

$$\sigma^2 = E\{(X(t) - \mu^1)^2\} \tag{2.4}$$

The variance is also called the second central moment. Another common second-order measure is the cross-correlation function (CCF) between two signals X(t) and Y(t+t1) with a time shift t1. Note the similarity to the ACF. The ACF can be thought of as the CCF applied to a single signal X(t).

$$CCF = E\{X(t) \cdot Y(t+t1)\} \tag{2.5}$$

Note that the CCF is maximized for the time shift t1 where the signals line up the best. In this case, the time shift t1 is called the time-delay between the signals. This peak value when normalized over the square root of the variance of each signal is called the cross-correlation coefficient. The ACF is maximized when the time shift is equal to zero and the value is one when normalized over the signal's variance. The third-order moment μ^3, in the time-domain, involves two independent time shifts t1 and t2.

$$\mu^3 = E\{X(t) \cdot X(t+t1) \cdot X(t+t2)\} \tag{2.6}$$

In the frequency domain the second-order measure is the power spectrum P(k) of a signal X(t) calculated by multiplying a signal's Fourier transform X(k) and the complex conjugate of the signal's Fourier Transform X*(k) together.

$$P(k) = X(k) \cdot X^*(k) \tag{2.7}$$

A signal's power spectrum can also be calculated by taking the Discrete Fourier Transform (DFT) of the autocorrelation function μ^2.

$$P(k) = DFT(\mu^2) = DFT(ACF) \tag{2.8}$$

A signal's third-order measure, in the frequency domain, is the bispectrum. The bispectrum B(k,l) can also be calculated in two ways. The first way makes use of the

Double Discrete Fourier Transform (DDFT), also known as the 2D Fourier Transform, applied to the third-order moment μ^3.

$$B(k,l)=DDFT(\mu^3) \tag{2.9}$$

The second way of calculating the bispectrum is by a product of the Fourier Transforms of a signal at three different frequencies (k, l, and k+l).

$$B(k,l) = X(k)\cdot X(l)\cdot X^*(k+l) \tag{2.10}$$

The cross-bispectrum (CBS) between two signals X(t) and Y(t) can be calculated with a product of Fourier Transforms of both signals at three different frequencies.

$$CBS(k,l) = X(k)\cdot Y(l)\cdot X^*(k+l) \tag{2.11}$$

Because the Fourier Transform of a signal contains both real and imaginary parts and because the bispectrum and CBS are the product of three Fourier Transforms, the bispectrum and CBS contain real and imaginary parts as well. A Fourier Transform X(k) of a signal X(t) can be expressed as a sum of it's real and imaginary parts multiplied by its complex magnitude |X(k)| and in the equivalent exponential form via Euler's Formula.

$$X(k) = |X(k)|\cdot(\cos\theta + i\cdot\sin\theta) = |X(k)|\cdot\exp(i\cdot\theta) \tag{2.12}$$

Here i is the square root of negative one and not an index. The phase information θ can be calculated for X(k) by first taking the ratio of the imaginary and real components of X(k), which is equivalent to the tangent of θ, and then taking the arctangent of the ratio to get θ. By taking the arctangent of the ratio of the imaginary and real parts, the phase information can be determined for a particular spectrum. The phase information is typically called the phase spectrum or phase estimator.

The difference $\phi(k,l)$ between the CBS and bispectrum phase estimators can then be used to calculate the function I(k,l).

$$I(k,l)=\exp(i\Phi(k,l)) \tag{2.13}$$

Du et al. (2004) explain that in BCSEIS the inverse Fourier Transform is applied to I(k,l) summed over frequencies k and l. They claim that the resulting function peaks at the time shift (i.e. time delay) between the signals, yielding a third-order method for estimating the time difference between the two signals. Nikias and Pan (1988) discuss this method in more detail along with several other methods for calculating time delays, between signals, from third-order measures.

Just as the second-order moment was related to the variance (i.e. width) of a signal's PDF, the third-order moment and the skewness of a PDF are also related. Skewness, also known as the third central moment, is a measure of the asymmetry of a PDF. The fourth central moment, called kurtosis, is the measure of whether the distribution is tall and skinny or short and squat. For a more thorough discussion of higher order statistics we recommend McLaughlin *et al.* (1995).

Note that a Gaussian signal has zero skewness. Gaussian signals can therefore be completely described by the first and second central moments (mean and variance). As a result, all moments of order higher than two (especially the signal's bispectrum) will be zero for Gaussian signals. Therefore, the time shift between two signals calculated using the bispectrum should not be contaminated by Gaussian noise sources unlike the time shift calculated by the second-order CCF.

According to Du *et al.*, (2004) the standard CC method computes the second-order measure (i.e. CCF) between two waveforms while the BS method computes the third-order measure (i.e. bispectrum) between two waveforms. Because the spectra of order higher than two of Gaussian noise sources will be zero, as

described above, they claim that the BS method can handle Gaussian noise sources for events at a given station better than the standard CC technique. Additionally, they say that even if the noise embedded in the signal is non-Gaussian, as long as it has zero skewness the BS method will suppress it. However they point out that in the case of more complicated noise sources the BS method will not always provide an advantage over the standard CC method. As a result, BCSEIS uses the BS method to help in verifying the validity of the CC method's time delay for event pairs recorded at common stations. Note that the BS method is performed on both the filtered and unfiltered waveforms in order to provide another means of handling noise. A CC time-delay passes the BS verification if the difference between the two BS time-delays (one for the filtered waveform and one for the unfiltered waveform) is within a threshold. Because the BS time-delay calculation is computationally intensive compared to the standard CC time-delay calculation (Du *et al.*, 2004), BCSEIS looks at the values of the CC coefficients to decide what to do next.

BCSEIS uses three limits to decide how to proceed with a particular event pair: upper, middle, and lower. Once the standard CC calculations are done for a particular event pair, for both P and S phases at all common stations (i.e. stations that detected both events in the pair), the largest of the computed CC coefficients, for the event pair, is compared to the upper CC limit. If it exceeds this limit, then all the CC coefficients for this pair, at all common stations, that are larger than the lower limit and pass the BS verification are saved along with their corresponding relative arrival times (i.e. delay times) calculated using the standard CC method. If the largest CC coefficient is smaller than the upper limit then the BS verification is done only for stations with CC coefficients above the middle limit. Any that pass the BS verification are then saved along with their corresponding relative arrival times

calculated from the standard CC method. Lastly, if the largest CC coefficient is smaller than the middle limit then the relative arrival times for the event pair are discarded. For this study we chose lower = 0.6, middle = 0.8, upper = 0.9 resulting in a total of 78 million selected CC differential times and coefficients.

Despite the claims by Du *et al.*, (2004) of BCSEIS's ability to handle correlated noise sources well, station 4601 had a larger percentage of high correlations (>0.7) than the other stations even at large hypocentral separation distances, as shown Figure 2.20. We believe this is due to the presence of the low frequency ringing, described above, embedded in most of the waveforms recorded by this station. This is also evident by the total number of event pairs calculated by station 4601 (over 25 million) compared to the numbers of station 4550 (13 million), 4616 (18 million), and hyd1 (20 million). We do not know the source of this correlated noise, which can be seen in the four traces from station 4601 for many events and was shown in the second trace from the top in Figure 2.12, but believe it could be associated with the alternating current frequency of European electricity which is 50 Hz. As a result of this noise affecting the correlations, we feel BCSEIS does not work as intended for our dataset.

2.3.2 Choosing Maximum Event Pair Separation

The maximum event pair separation distance of 500 meters was a parameter we chose early in the study by looking at the distribution of event pair hypocentral separation distance without realizing that BCSEIS calculates epicentral (2D: latitude, longitude) instead of hypocentral (3D: latitude, longitude, depth) distance. Now, after plotting the relationship between hypocentral event pair separation distance and CC coefficient, it's clear that the BCSEIS needs to be modified to calculate

hypocentral separation distance. The reasoning behind BCSEIS using epicentral separation distance might have been that Du *et al.* (2004) designed it for regional earthquake datasets where depths are poorly constrained in event catalogs. Since we are using very local microseismic earthquake data, hypocentral separation distance is crucial as events might be very near in their latitude and longitude but far apart in depth. Figure 2.18 shows the distribution of event pair hypocentral separation distances for all 8930 events used in our study. This was the plot used early in the study to choose the maximum separation distance before we determined, by looking at the source code, that BCSEIS calculates epicentral distance. Figures 2.19-2.22 show the relationship between event pair hypocentral separation distance and the corresponding CC coefficient for the event pairs with an epicentral separation distance less than or equal to 500 m. Note how the distribution decreases in CC coefficient as the event pair hypocentral separation distance increases while staying within the maximum epicentral separation distance of 500 m. From these plots, it is clear that choosing a value of 1500 or 1600 meters maximum hypocentral separation distance would be an appropriate value in conjunction with the modification to BCSEIS's event pair distance calculation. It's also interesting to note how there is a high percentage of event pairs with high cross-correlation coefficients at large hypocentral separation distances for station 4601 up to about 1600 meters and then there's a sharp drop. This could be as a result of the low frequency ringing noted above which could have yielded false correlations. Also note that BCSEIS only outputs correlations larger than 0.5 which is why the plots are scaled from 0.5 to 1 on the CC coefficient axis. A last thing to note is how all four plots show that the largest percentage of events, per 100 m depth interval, have CC coefficients between 0.5 and 0.6.

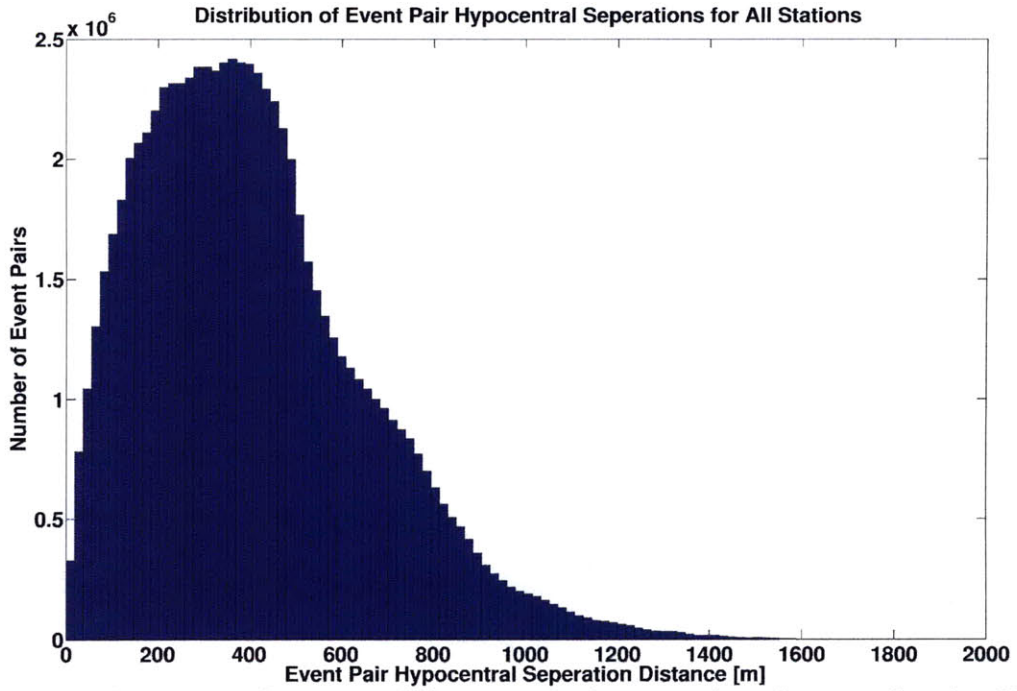

Figure 2.18. Histogram of event pair hypocentral separation distance for the 8930-event catalog.

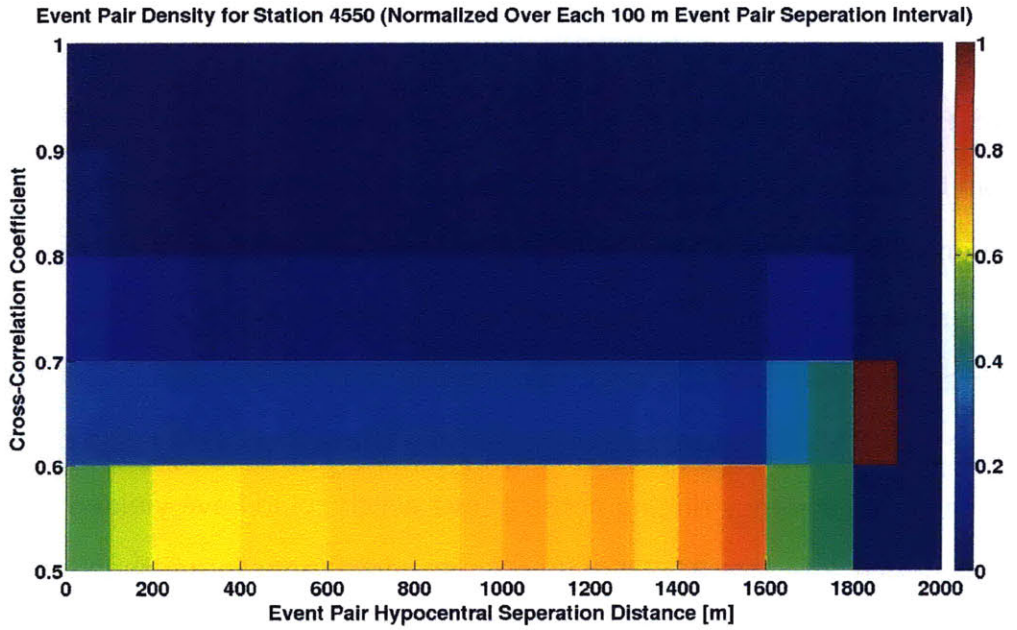

Figure 2.19: Density of event pairs based on their relationship between event pair hypocentral separation distance and cross-correlation coefficient for station 4550. Note that each cell represents the percentage of event pairs within the range of CC coefficients at the given 100 m interval in hypocentral separation distance.

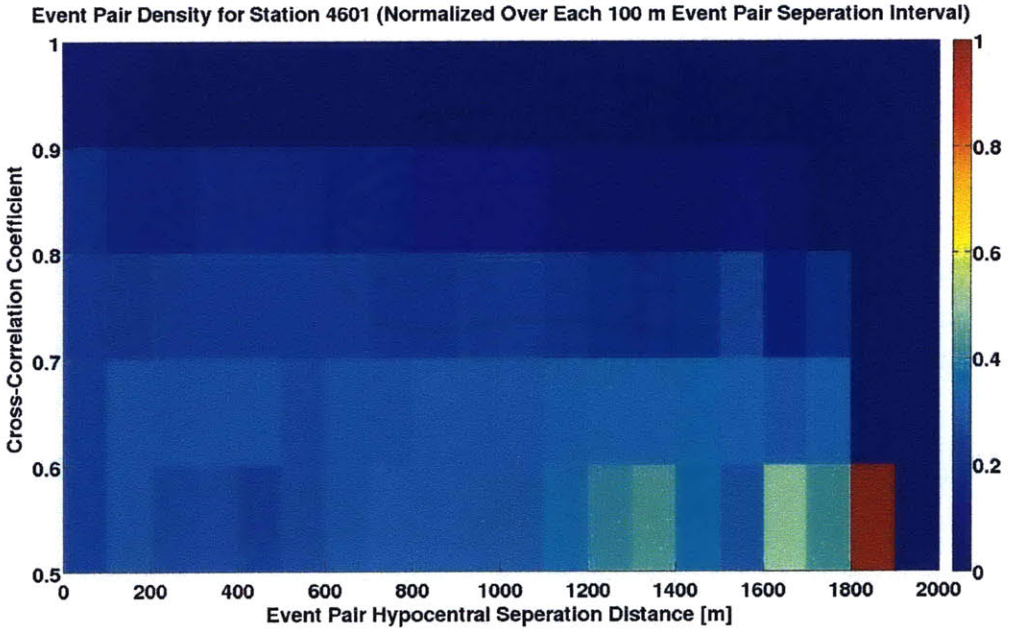

Figure 2.20: Density of event pairs based on their relationship between event pair hypocentral separation distance and cross-correlation coefficient for station 4601. Note that each cell represents the percentage of event pairs within the range of CC coefficients at the given 100 m interval in hypocentral separation distance.

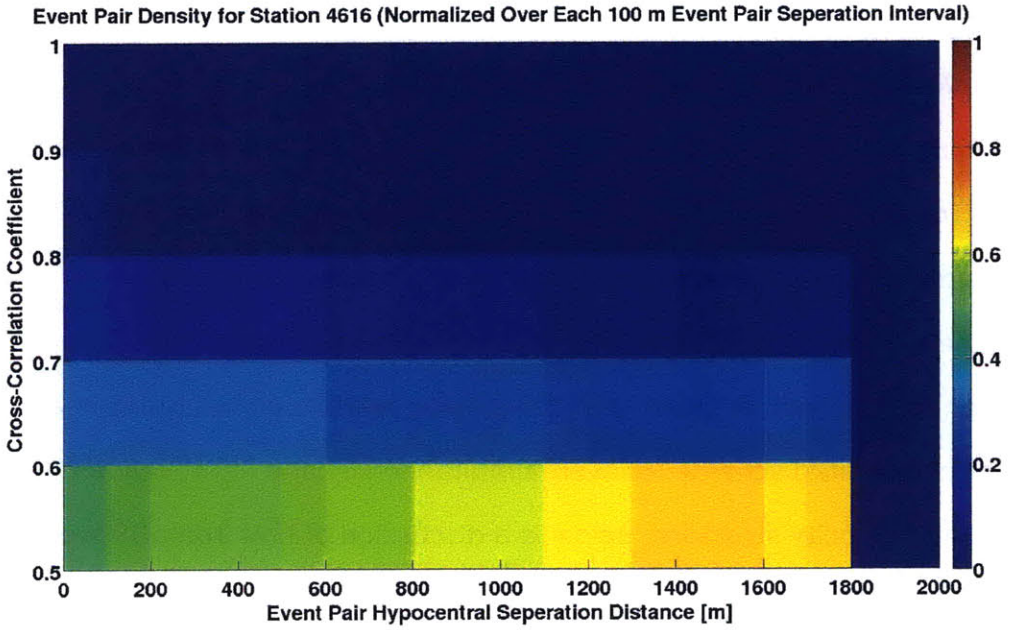

Figure 2.21: Density of event pairs based on their relationship between event pair hypocentral separation distance and cross-correlation coefficient for station 4616. Note that each cell represents the percentage of event pairs within the range of CC coefficients at the given 100 m interval in hypocentral separation distance.

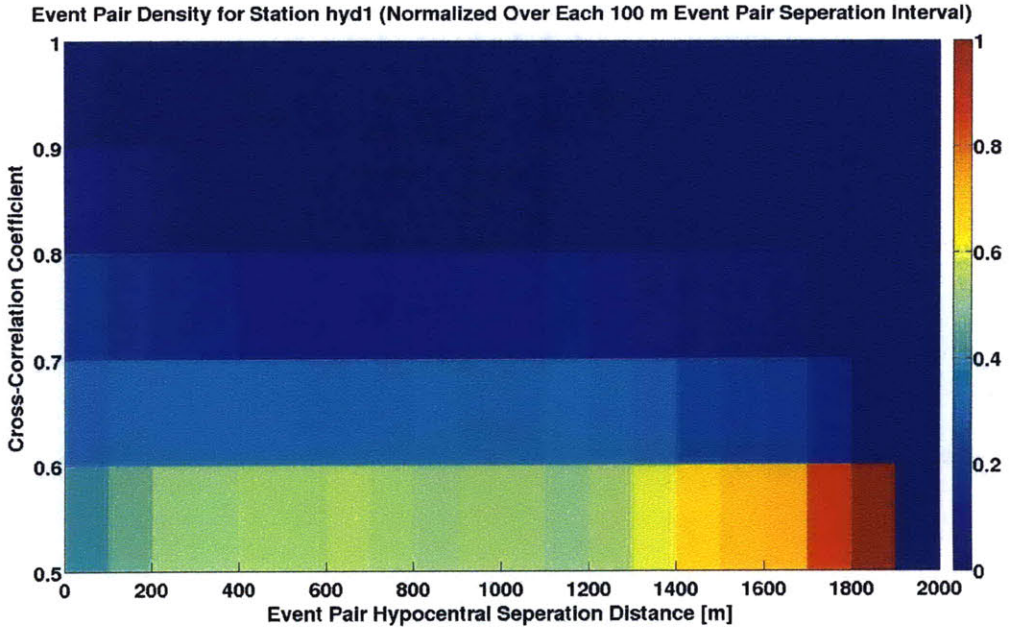

Figure 2.22: Density of event pairs based on their relationship between event pair hypocentral separation distance and cross-correlation coefficient for station hyd1. Note that each cell represents the percentage of event pairs within the range of CC coefficients at the given 100 m interval in hypocentral separation distance.

2.4 Double-Difference Tomography

Zhang and Thurber (2003) developed a double-difference tomography method (TomoDD), which incorporates both relative and absolute arrival times for simultaneously relocating events and calculating a three-dimensional velocity model. The algorithm they developed uses the absolute arrival times, cross-correlation relative arrival times, and the catalog relative arrival times in a hierarchical weighted scheme to invert simultaneously and iteratively for both event locations and velocity structure. Below is a discussion of how TomoDD works as well as how parameter values and settings were chosen.

2.4.1 TomoDD in Detail

To understand the advantages of this method, a brief discussion of previous methods is necessary. In the last fifteen years many seismic studies have shown the advantage of using waveform cross-correlation to improve relative arrival time estimates. These methods are based on the assertion that closely-located events, whose waves propagate along similar paths to receiving stations, will produce similar waveforms (Zhang and Thurber, 2003). Zhang and Thurber (2003) describe two common approaches for using waveform cross-correlation data for tomography along with their advantages and disadvantages.

The first approach involves using the relative times to determine relative locations and thereby takes full advantage of the information contained in the data (Waldhauser and Ellsworth, 2000). However, it uses simplifying assumptions such as that all events in a cluster have the same take off angle and azimuth to each station. As a result, the calculated locations are relative instead of absolute. Also, it uses a location algorithm that assumes that velocity heterogeneity is location-independent which they show is valid for closely spaced events but not valid for events that are far apart. This assumption can bias event locations for event pairs that are widely separated.

The second approach adjusts absolute arrival times to minimize the errors in relative arrival times and still yield absolute locations. TomoDD is based on a modification to this approach that does not adjust arrival times. TomoDD uses both the relative times (from both cross-correlation and phase catalog) and absolute arrival times (from phase catalog) to jointly produce a three-dimensional velocity model (starting from a simple layered model) and relocate the events. As a result, TomoDD produces absolute locations that have been refined by the relative

information without having to make assumptions about path heterogeneity. Zhang and Thurber (2003) give further details including examples from using both synthetic and real data.

2.4.2 The Double Difference Algorithm

The arrival time T^i for a body wave going through a medium is a function of the event's origin time τ^i and the unknown velocity $v(\vec{x})$ in the medium integrated along the wave's unknown path s from the source i to receiver k.

$$T_k^i = \tau^i + \int_k \frac{1}{v(\vec{x})} ds \tag{2.14}$$

Because the arrival time is related to position of the source and receiver and is inversely related to the unknown velocity structure, the problem is nonlinear. To be able to solve this nonlinear problem a Taylor series expansion is performed for the position-arrival time relation. Also the slowness rather than the velocity is calculated. The result is a linearized misfit function r relating the difference between observed and predicted arrival times to perturbations in the event locations (x_1^i, x_2^i, x_3^i) and slowness u.

$$r_k^i = \sum_{l=1}^{3} \frac{\partial T_k^i}{\partial x_l^i} \Delta x_l^i + \tau^i + \int_k \partial u \, ds \tag{2.14}$$

The double difference approach goes a step further and subtracts the misfits between similar events at common stations.

$$dr_k^{ij} = r_k^i - r_k^j = (T_k^i - T_k^j)^{obs} - (T_k^i - T_k^j)^{calc} \tag{2.15}$$

Here the double difference (dr_k^{ij}) and therefore the time differences $(T_k^i - T_k^j)$ between the events only depend on their hypocentral separation distance and on

the velocity heterogeneity near them. This is done assuming that the events are near each other so the portion of their ray paths that lay outside the seismic zone are similar, as illustrated in Figure 2.23. Assuming that their paths are similar will cause any effects of velocity heterogeneity encountered along common portions of their paths to the receiver to cancel out near the receiver by subtracting the misfits. Note that TomoDD uses distance weighting to select event pairs with hypocentral separation distance equal or less than the value used as the weight in kilometers. TomoDD also includes the absolute time picks so that any velocity heterogeneity outside the source region and near receivers can be resolved. The rays and arrival times are calculated from these picks using a pseudo-bending ray-tracing algorithm (Um and Thurber, 1987).

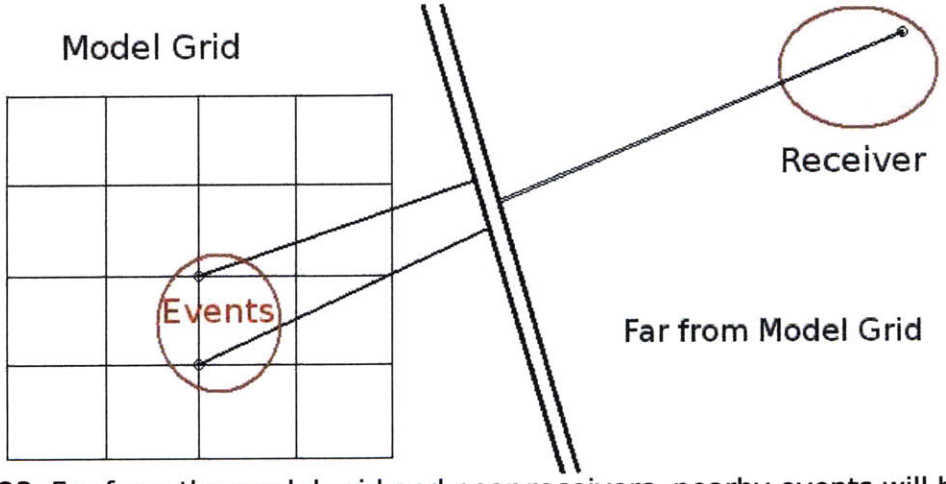

Figure 2.23. Far from the model grid and near receivers, nearby events will have almost identical paths so any arrival/travel time differences between these events with high similarity will be dependent on any velocity heterogeneity near the events and on their hypocentral separation distance, not on heterogeneity near the receiver.

The three-dimensional velocity structure is described by velocities at a set of nodes. Trilinear interpolation is used between adjacent nodes. A first order smoothing model is used as regularization to limit the spatial variation in structure.

This regularization is based on the difference in slowness perturbations between adjacent nodes via a first derivative as a measure of model roughness. A weighting parameter is then used for each direction (X,Y,Z) to scale the roughness against the model residual. The complete system of misfit equations and smoothing equations are solved using the LSQR algorithm developed by Paige and Saunders at Stanford (1982).

2.4.3 Weighting Between Different Data Types

TomoDD uses a heretical weighting scheme to apply greater weight to the different types of data at different iterations in the inversion. Zhang and Thurber (2003) explain that early on it is best to weigh the absolute and differential times from the phase catalog highest in order to get large scale structure and absolute locations. Later in the inversion they recommend more weight is placed on the differential times from the CC calculations to provide a refinement of the velocity structure and event locations. In the final iterations distance weighting can be used to throw out event pairs that are spaced far apart.

2.4.4 Setting Up TomoDD

It is important to note that we obtained four main sets of results which included a set only using differential times, another not utilizing station corrections in conjunction with absolute times, and two sets using station corrections which we obtained from calibration shots performed by Dyer *et al.* (1994) and from a JHD inversion from Rowe *et al.* (2002). We used the absolute arrival times that came with the data set as well as both sets of differential arrival times (catalog and cross-correlation) and both sets of locations (JHD and collapsed), obtained from Tohoku

University who used the method of Jones and Stewart (1997), as the starting event locations. The catalog differential times were calculated using ph2dt, a script included in HypoDD (Waldhauser, 2001). Ph2dt was setup to calculate differential times for event pairs with hypocentral separation distance of less than or equal to one kilometer.

We followed the suggestion of Zhang and Thurder (2003) and started the inversion by initially applying more weight to the absolute times and the relative catalog data (or just to the relative catalog data in the absence of absolute times) and less to the cross-correlation relative times in order to get initial locations from the absolute times and relative locations of distant event pairs from the differential catalog data. As the inversion progressed, more weight was applied to the more accurate cross-correlation relative times in order to further refine the relative event locations and velocity model. Dampening, used to stabilize the inversion, was also reduced as the inversion progressed and converged on a solution. Distance weighting was used in the last few iterations to further refine the locations by selecting event pairs with small separation distance and discarding all other data in that iteration of the inversion. Note that a joint inversion (locations and velocity model) was not performed at every iteration. This is due to the locations converging much slower than the velocity model because the locations are less linear in relation to the arrival time residuals than the slowness model from which the velocities are calculated. So some iterations only relocated events to allow the locations to converge before performing another velocity model inversion. Figure 2.24 shows an example input file with explanations of the parameters used for a typical run of TomoDD.

```
*--- input file selection
* cross-correlation differential times:
../dt.cc4
*catalog differential times:
../dt.ct
* catalog absolute times:
../absolute.dat
* event catalog file:
../event.dat.new.JHD
* station file:
../station.dat
*--- output file selection
* original locations:
soultz_8930_O3_cutoff500_CC.loc
* relocations (final and per iteration):
soultz_8930_O3_cutoff500_CC.reloc
* station information:
soultz_8930_O3_cutoff500_CC.sta
* final residual information:
soultz_8930_O3_cutoff500_CC.res
* output velocity at each iteration
soultz_8930_O3_cutoff500_CC.vel
* final Vp model
Vp_model.dat
* final Vs model
Vs_model.dat
*--- data type selection:
* IDAT:  0 = synthetics; 1= cross corr; 2= catalog; 3= cross & cat
* IPHA: 1= P; 2= S; 3= P&S
* DIST:max dist [km] between cluster centroid and station
* IDAT   IPHA   DIST
  3       3       30
*--- event clustering:
* OBSCC:    min # of obs/pair for crosstime data (0= no clustering)
* OBSCT:    min # of obs/pair for network data (0= no clustering)
* OBSCC  OBSCT  CC_format
  0         0         1
*--- solution control:
* ISTART:          1 = from single source; 2 = from network sources
* ISOLV:           1 = SVD, 2=lsqr
* NSET:            number of sets of iteration with specifications following
*  ISTART  ISOLV  NSET  smoothing-weight1 s.-weight2  s.-weight3  air_depth
   2         2       18     5                    5             5             -1.5
* i3D delt1 ndip iskip scale1 scale2 iuses
  2   0      9    1      0.1     1.00   2
* xfac   tlim        nitpb(1) nitpb(2) stepl
  1.3    0.0005    50         50        0.5
* lat_Origin         lon_Origin      Z_Origin iorig rotation
  48.93722222    7.88416666   0          1     0
*--- data weighting and re-weighting:
* NITER: The number of iterations using these parameter values
* WTCCP, WTCCS:                  weight cross P, S
* WTCTP, WTCTS:                  weight catalog P, S
* WRCC, WRCT:            residual threshold in sec for cross, catalog data
* WDCC, WDCT:                    max dist [km] between cross, catalog linked pairs
* WTCD:   relative weighting between absolute and differential data
* THRES: Scalar used to determine the DWS threshold values
* DAMP:                  damping (for lsqr only)
* NITER WTCCP WTCCS WRCC WDCC WTCTP WTCTS WRCT WDCT WTCD DAMP JOINT THRES
```

```
  3     0.01    0.008   -9      -9      1.0     0.80    -9      -9      0.1   550   1     0.1
  3     0.01    0.008   -9      -9      1.0     0.80    8       -9      0.1   350   0     0.1
  3     0.01    0.008   8       -9      1.0     0.80    7       20      0.1   550   1     0.1
  3     0.01    0.008   8       -9      1.0     0.80    7       20      0.1   350   1     0.1
  2     1       0.8     8       -9      0.01    0.008   6       20      0.1    800  1     0.1
  3     1       0.8     8       -9      0.01    0.008   6       20      0.1    500  0     0.1
  2     1       0.8     6       -9      0.01    0.008   6       20      0.1    800  1     0.1
  3     1       0.8     6       .8      0.01    0.008   6       20      0.1    500  0     0.1
*--- event selection:
* CID:   cluster to be relocated (0 = all)
* ID:    cuspids of event to be relocated (8 per line)
* CID
   1
* ID
```

Figure 2.24: A sample input file used in the TomoDD inversion package. Note that DWS is a qualitative measure of the model resolution.

Note that more weighting is placed on the catalog data for the first ten iterations and always more on the times from the P-picks than those from the S-picks. More weight is always placed on the times from the P-picks as their arrival times are easier to determine from looking at the waveform traces than those of the S-picks. For the remaining iterations, more weight is placed on the cross-correlated differential times than on the catalog times and the distance weighting is started to select event pairs within 800 meters hypocentral separation and decreased slowly to 50 meters after many iterations. Also note how some sets of iterations only invert for locations (Joint = 0) to allow the locations to converge before performing a model inversion (Joint = 1) for the reasons explained above.

2.4.5 Starting Velocity Model

From sonic log analysis of GPK1 (Dyer, 2000) as well as calibration shot data (Dyer *et al.*, 1993) the initial velocity model was developed. The shot data yielded a P-wave velocity of 5.85 km/s and S-wave velocity of 3.34 km/s from a shot at a depth of 3360 meters. Then Dyer (2000) used the velocity gradients from sonic logs to calculate the P and S-wave velocities at other depths. From his calculations, we

created a model with 100 meter node spacing (in all directions) in the middle of the reservoir where the events are concentrated and a total size of 15x19x23 (X,Y,Z) nodes. The starting model was a layered model with velocity values shown in Table 2.1. Note how both P and S-wave velocities increase with depth.

Initial Velocity Model	200 m Depth (Slice 1)	1300-4000 m Depth (Slices 2-21)	5000 & 8000 m Depth (Slices 22 & 23)
Vp [km/s]	5.8	5.85	6
Vs [km/s]	3.35	3.44	3.5

Table 2.1: P and S velocities at different depths (i.e. nodes) in the starting model we created from the calibration shot data of Dyer *et al.* (1993).

2.4.6 TomoDD Output

TomoDD outputs several files with velocity models, residuals, locations, take-off angles and runtime output per iteration. The final velocity model was plotted to form horizontal and vertical P and S-wave velocity cross-sections through the reservoir. The location residuals were also plotted to see temporal and depth changes. The residuals summed over all events and stations were extracted from the log file to interpret the quality of the sets of locations. Results from plotting all these outputs are depicted and interpreted in the following chapter. Determination of the goodness of fit of the velocity model was complicated but was also completed. A more detailed explanation of this is given in the next section.

2.4.7 Velocity Model Resolution

Determining the quality of the final velocity model is a more complicated affair as described by Zhang and Thurber (2007). According the them, the standard

practice of calculating the full resolution matrix by applying singular value decomposition (SVD) to the sensitivity matrix is too inefficient and can take weeks on the most powerful of computers. To circumvent having to the calculate the full resolution matrix using SVD, they used a measure called the ray-sampling density which is also known as the derivative weighted sum (DWS). This measure gives an estimate of the density of rays traveling through a given node in the model without considering ray angular coverage. According to them, the larger the DWS values, the larger the singular values (i.e. model resolution) as shown in Figure 4 of their paper (Zhang and Thurber, 2007). In other words, the larger the DWS value for a given node, the more rays are traveling through the node and therefore the better sampled that node is. Well sampled nodes are assumed to have a good fit between velocity model and travel time data. Tests on real and synthetic data show that this is a valid assumption (Zhang and Thurber, 2007; Toomey and Foulger, 1989; Toomey *et al*. 1994). As a result, we use the DWS values as an indicator of model resolution at each model node.

Additionally, a checkerboard test was performed to further test the inversion's performance. In this test the homogeneous starting model (described in Section 2.4.5) was perturbed in a checkerboard pattern and then used to generate a synthetic set of absolute and differential times using the same starting event locations as used in the real data. These synthetic data are then inverted using the non-perturbed starting homogeneous velocity model to see how well the inversion can recover the perturbed checkerboard velocity model.

It is also important to note that there was a trade-off between data and model variances (square of RMS of differences between final and starting velocity models) by selecting different values for the smoothing weight parameters. This

made it important to run the inversion using different values of smoothing to find the optimum value which minimized both data and model variances. Zhang and Thurber (2007) discuss this in more detail. Figure 3 from Zhang and Thurber (2007) shows how different values of smoothing affect the data and model variances produced by the inversion for constant dampening. As a result, we ran the inversion using different smoothing weights. We discuss the tomogram results in the next chapter along with the results of running the checkerboard test and the analysis of the DWS values.

CHAPTER 3

RESULTS AND INTERPRETATION

3.1 Introduction

We present the results of running TomoDD on the Soultz EGS 1993 stimulation data using various smoothing values and combinations of absolute and differential time data. We discuss how the final set of results was selected by analyzing the P and S-wave velocity structure, velocity model variance (with respect to the starting model) and RMS residuals for all three types of data used in the inversion for different values of smoothing. Then we look at the derivative weighted sum (DWS) values, discussed in Chapter 2, of the selected set to see where the model is resolved the best based on the source and receiver geometry. Also we run a checkerboard test to further understand the resolving power of the inversion method based on the source and receiver geometry. Lastly, we interpret the selected set in conjunction with results from other studies to gain an understanding of what TomoDD can illuminate in the reservoir.

3.2 Results

The open-hole depth (i.e. uncased well depth in which water was in contact with basement rock) ranged from 2850 to 3600 meters, according to Dyer *et al.* (1994). A majority of the seismicity accompanying the injection occurred at depths between 2500 and 3600 meters (see Figure 2.11). To understand how the reservoir was affected by the water injection experiments we show horizontal slices of the inverted three-dimensional velocity model from 2500 to 3600 meters in 100 meter intervals along with the TomoDD relocated event locations as part of the joint

inversion. On these tomograms, the microseismic events within 50 meters of the depth slice are plotted. Also, the position-at-depth of GPK1, the injection well used in this stimulation, is shown.

We chose to focus on four sets of results all with smoothing set to 5. How this smoothing value was chosen is discussed in Section 3.2.2. The first set A.1. (shown in Section A.1) was calculated using all the available data (absolute times, differential catalog times, and differential cross-correlation times) and using station corrections, applied to the absolute times, from Dyer *et al.* (1994) who calculated them from calibration shots in the injection well (GPK1). The second set A.2 (shown in Section A.2) also contains all the available data but uses station corrections obtained by Rowe *et al.* (2002) who obtained them from a Joint Hypocenter Determination (JHD) inversion. The third set A.3 (shown in Section A.3) also contains all the available data but no station corrections. The fourth set A.4 (shown in Section A.4) contains only differential times (both from catalog and cross-correlations). Table 3.1 summarizes the data types used in each of the four sets of results. Note that all sets of results were calculated using starting locations from the JHD location catalog obtained from Tohoku University. Figure 3.1 shows three plots of the Tohoku University JHD locations used (plan view, North-South vs Depth, and East-West vs Depth). Figure 3.2 shows the collapsed locations that were also obtained from Tohoku University who used the method of Jones and Stewart (1997) for comparison with the JHD locations. We consider the collapsed locations to be the most compact and found that using them as starting locations introduced a slight bias in the final locations. As a result, we chose to go with the more diffuse JHD locations as the starting event locations.

Inversion	Absolute Times	Differential Catalog Times	Differential CC Times	Station Corrections	Complete Set of Plots
1	X	X	X	Dyer	A.1
2	X	X	X	Rowe	A.2
3	X	X	X	-	A.3
4	-	X	X	N/A	A.4

Table 3.1: Summary of the data types used in the four sets of results.

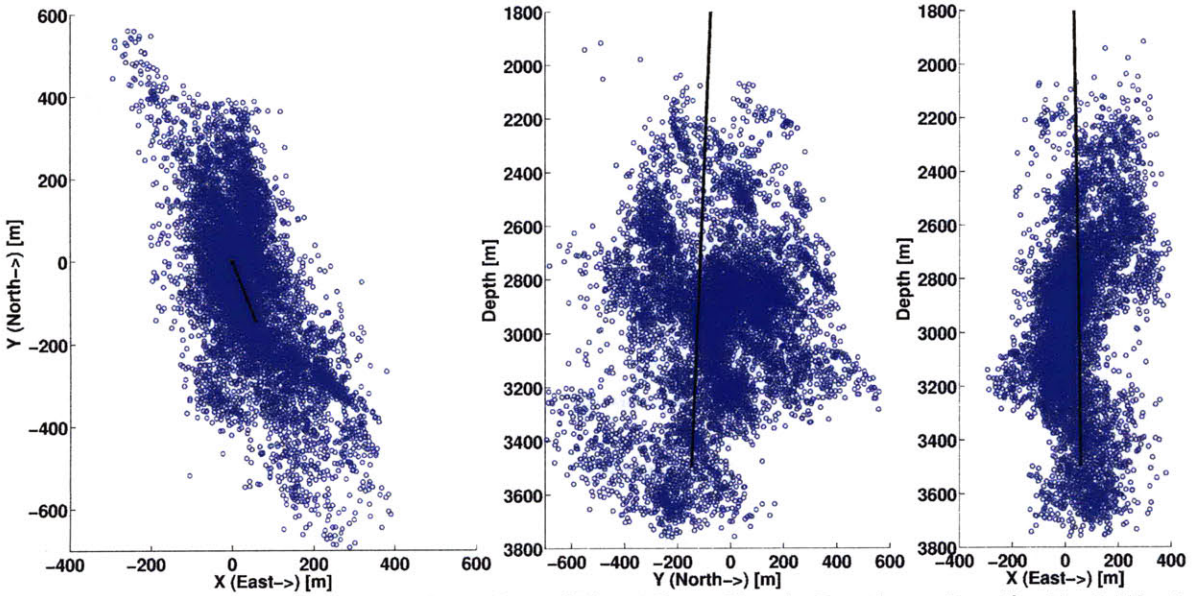

Figure 3.1: Starting JHD event locations (Plan View, North-South vs Depth, East-West vs Depth) with the path of the injection well GPK1 (black line) through the reservoir.

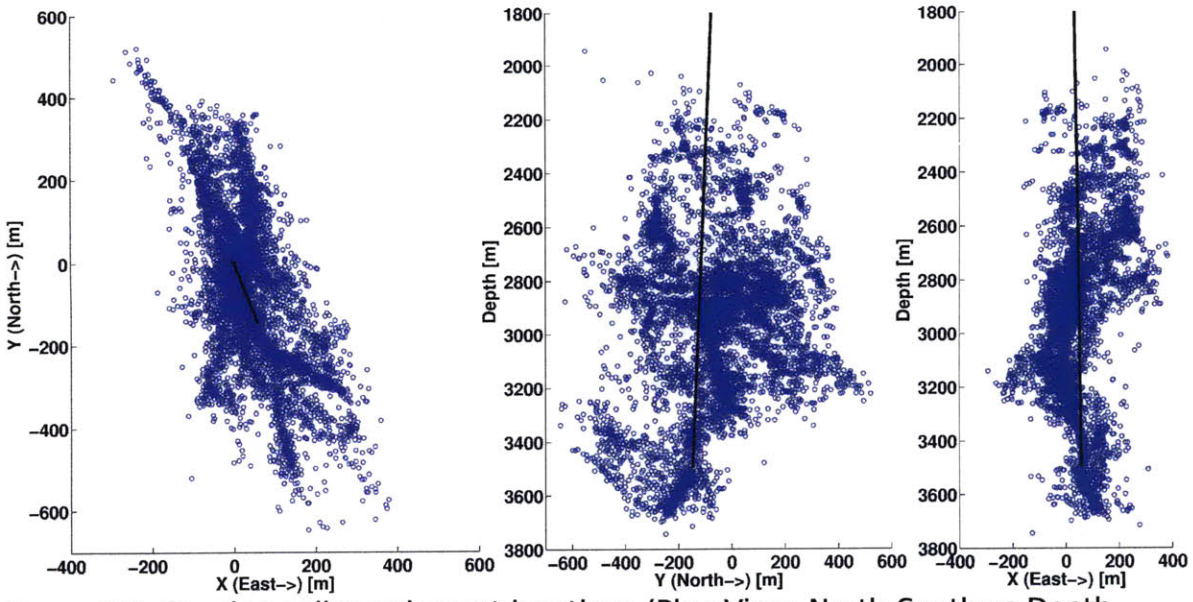

Figure 3.2: Starting collapsed event locations (Plan View, North-South vs Depth, East-West vs Depth) with the path of the injection well GPK1 (black line) through the reservoir.

For convenience in this chapter we show only the figures necessary to illustrate key features including differences between sets of results based on varying smoothing weights and types of data included in the inversion. Refer to Appendix A for all four complete sets of results.

3.2.1 General Trends

At shallow depths, the tomograms among all four sets are similar except those for A.4 which show a big difference in the P-wave velocity structure compared to the other sets, as shown in Figure 3.3. This figure shows P and S-wave tomograms centered at 2500 meters, for all four sets. Figure 3.4 shows P and S-wave tomograms centered at 2700 meters for all four sets. At 2700 meters depth, sets A.1 through A.3 show large similarity for the P-wave velocity structure with A.4 standing out again. At this depth, sets A.1 and A.4 show similar S-wave velocity

structure but are different from the similar S-wave velocity structure of the A.2 and A.3 tomograms. It is not until 2900 meters depth that all four inversions have similar P-wave tomograms, as shown in Figure 3.5. However for the S-wave velocity structure A.1 stands out with the lack of a low S-wave velocity zone. Figure 3.6 shows P and S-wave tomograms centered, for all four sets, at 3100 meters. At this and deeper depths, all sets agree significantly for both the P and S-wave tomograms which boosts our confidence in the method at these depths, as shown in Figures 3.6, 3.7 and 3.8.

It is also important to note the relationship between velocity structure and microseismic event locations. In this respect, S-wave tomograms show a stronger correlation with microseismic clustering than P-wave tomograms at all depths, for all sets. This relationship does improve for both P and S-waves with increasing depth. Also note how most of the velocity structure and microseismic event clusters have NNW-SSE trends.

In Figure 3.5 it is important to note that at the injection well GPK1 (denoted by the black circle) the tomogram from set A.1 lacks a low S-wave velocity zone. This low S-wave velocity zone results from the presence of fluid filled fractures, which is explained in more detail later, was expected due to an assortment of geophysical well logs including Schlumberger Ultrasonic Borehole Imager (UBI) showing a large fracture network intersecting the injection well between 2850 to 3000 meters depth and spinner logs showing 30-50% fluid loss in that same depth range, according to Evans *et al.* (2005). Figure 1.1, borrowed from Evans *et al.* (2005), shows the fracture density, flow profile, and other well log measurements for the entire open-hole depth of GPK1 for the 1993 stimulation experiment. Note how A.2, A.3 and A.4 do contain the expected low S-wave velocity zone at 2900

meters depth.

The final event locations among the four sets of results are shown in Figures 3.9, 3.10, 3.11, and 3.12 in three views (plan view, North-South vs Depth, and East-West vs Depth). Note how sets A.1 and A.4 produce clusters that approach the compactness of the collapsed event locations produced by Tohoku University and shown in Figure 3.2. A.2 and A.3 on the other hand are slightly more diffuse than the starting JHD locations and much more diffuse than the collapsed locations. Also note that the locations of A.2 and A.3 are shifted to the South-East with A.3 having the largest shift. We believe this is due to not using station corrections in A.3 and the use of JHD derived station corrections in A.2. A.1 does not suffer from this shift leading us to conclude that the calibration-shot derived station corrections are the best. A.4 also does not have any shifting due to it only using differential times and thereby avoiding the use of station corrections. These shifts can be clearly seen in Figures 3.13 through 3.16 which show the final event locations in red plotted with the initial JHD locations in blue. Additionally, Figures 3.13 through 3.16 show that A.1 and A.4 line up the best with the linear structures present in the JHD locations. A.4 lines up better with the cylindrical cluster of JHD event locations in the South-East (centered at North = -300, East = 200) than A.1. In Figure 3.16 it is clear that for the A.4 set of locations the cylindrical cluster to the South-East is tilted towards the South with rotation point at the centroid and an angle of a couple of degrees versus about five degrees for the A.1 set. Because the locations for A.2 and A.3 are more diffuse, an angular measurement was not made. Additionally from Figures 3.17 and 3.18 it is clear that the A.4 locations line up better with the collapsed event locations than the A.1 locations.

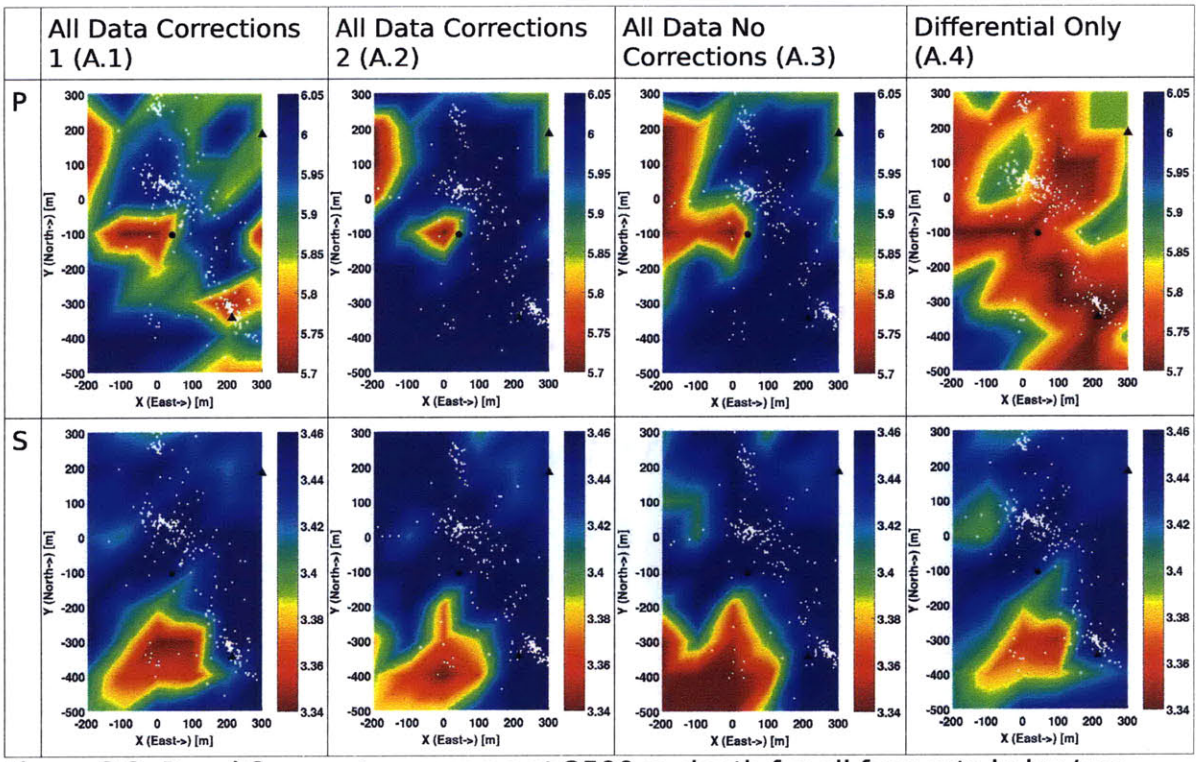

Figure 3.3: P and S-wave tomograms at 2500 m depth for all four sets in km/sec.

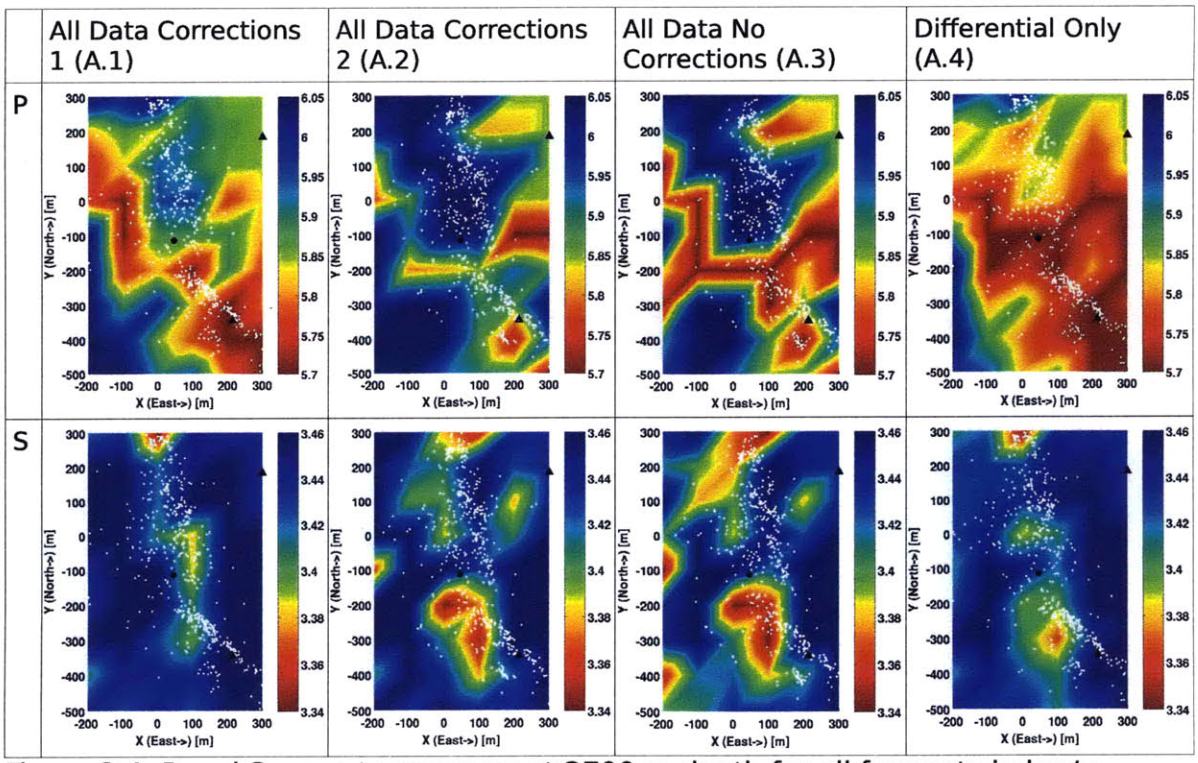

Figure 3.4: P and S-wave tomograms at 2700 m depth for all four sets in km/s.

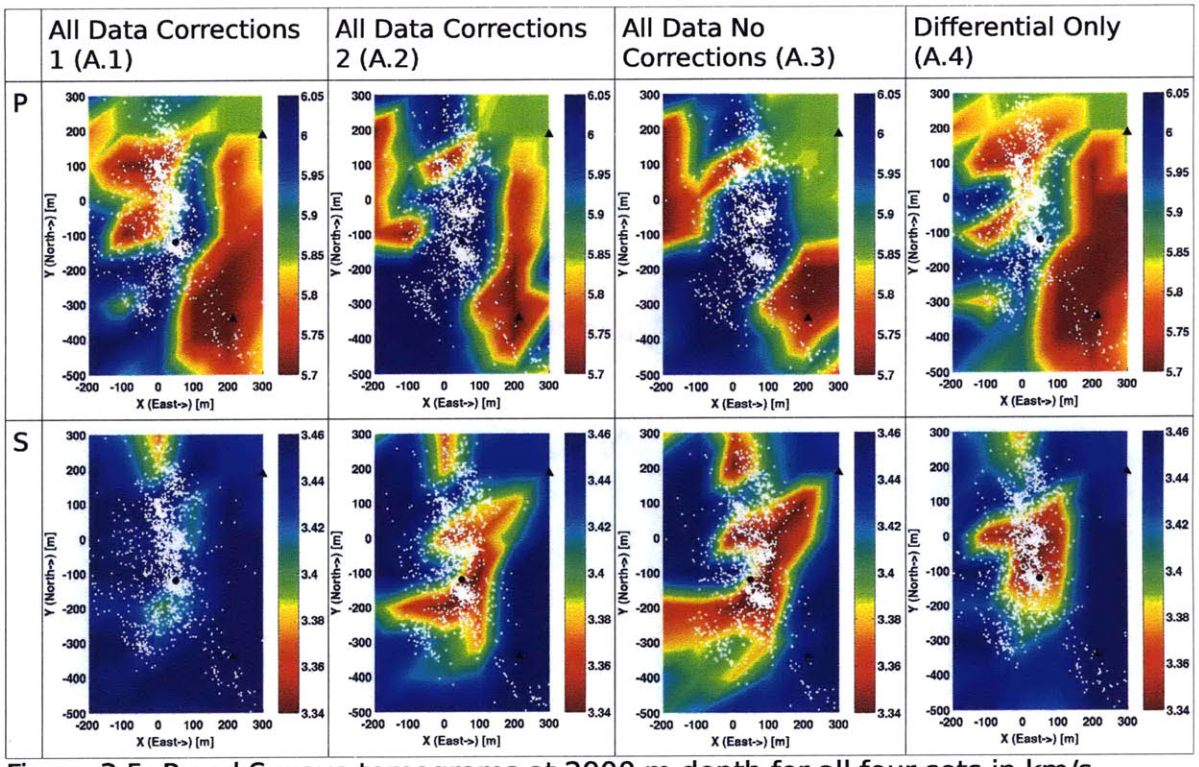

Figure 3.5: P and S-wave tomograms at 2900 m depth for all four sets in km/s.

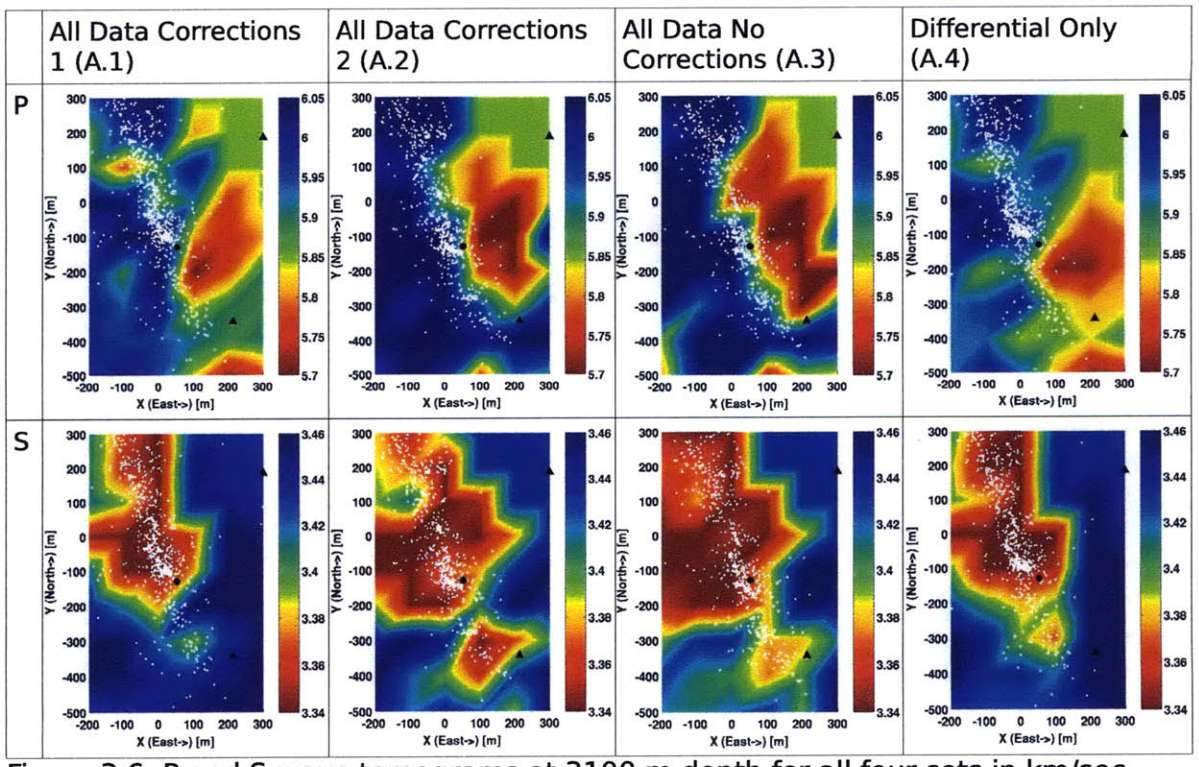

Figure 3.6: P and S-wave tomograms at 3100 m depth for all four sets in km/sec.

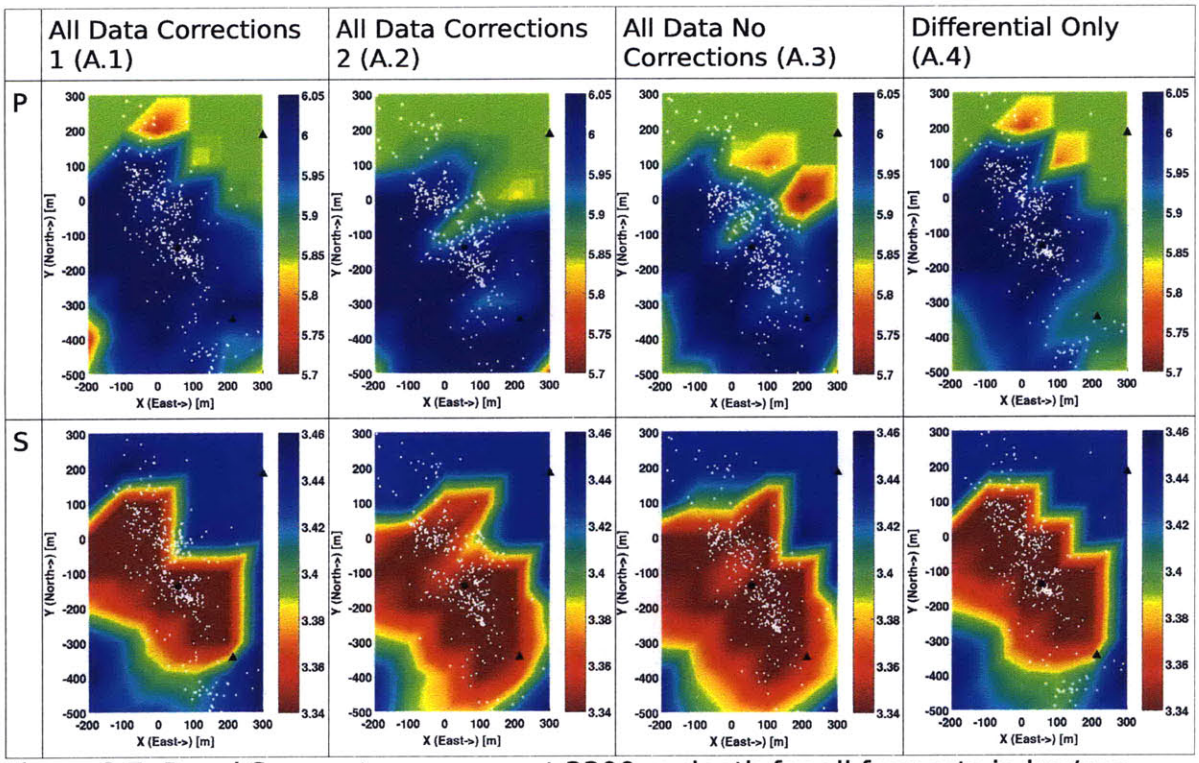

Figure 3.7: P and S-wave tomograms at 3300 m depth for all four sets in km/sec.

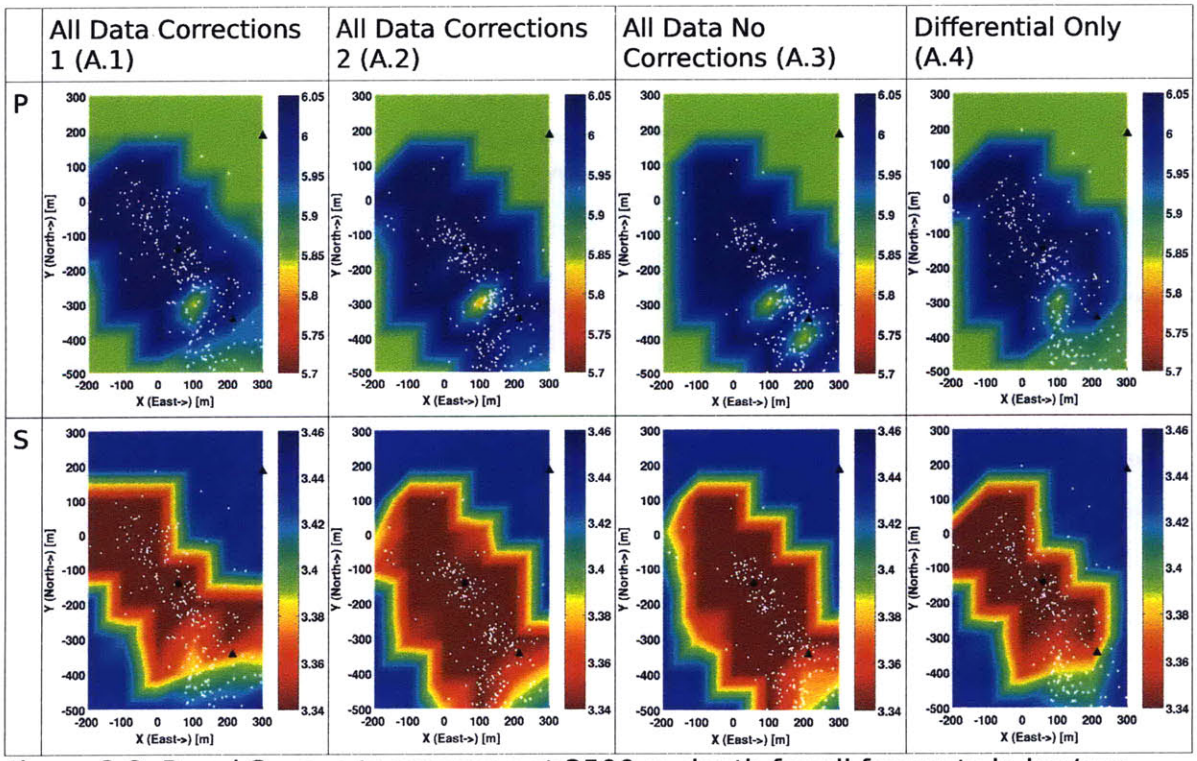

Figure 3.8: P and S-wave tomograms at 3500 m depth for all four sets in km/sec.

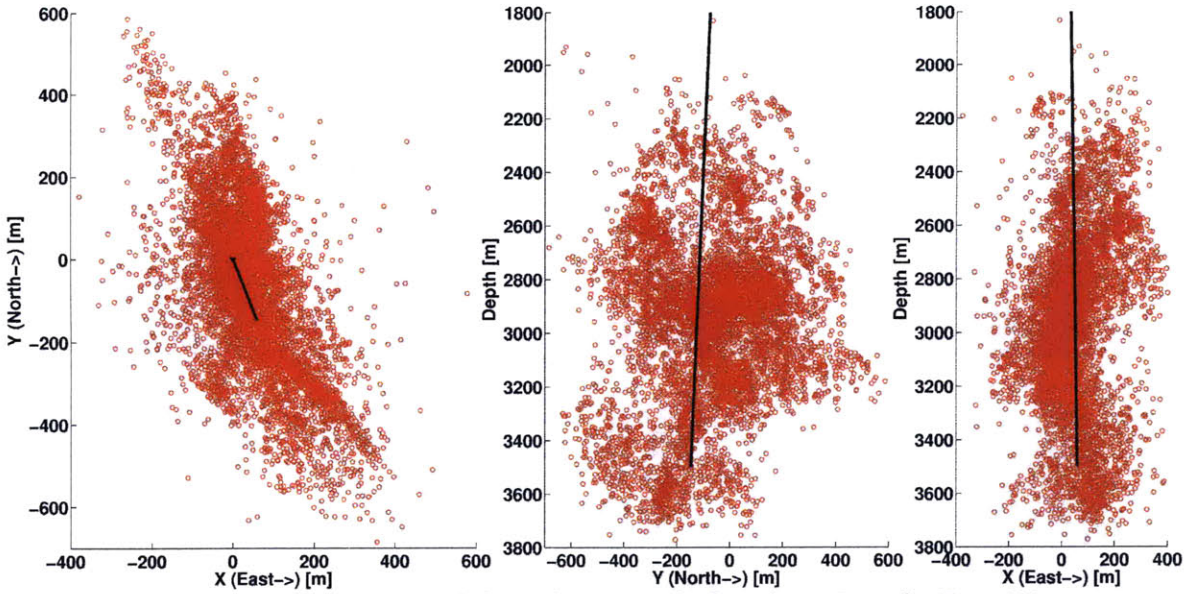

Figure 3.9: Final event locations (Plan View, North-South vs Depth, East-West vs Depth) with the path of the injection well GPK1 (black line) through the reservoir for the results set A.1.

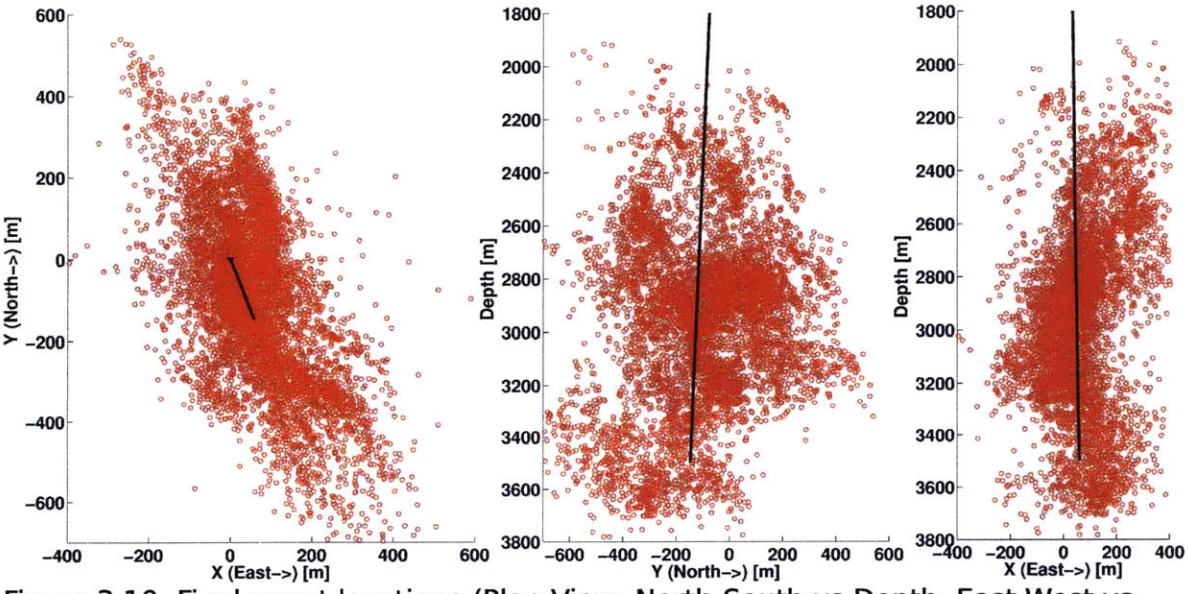

Figure 3.10: Final event locations (Plan View, North-South vs Depth, East-West vs Depth) with the path of the injection well GPK1 (black line) through the reservoir for the results set A.2.

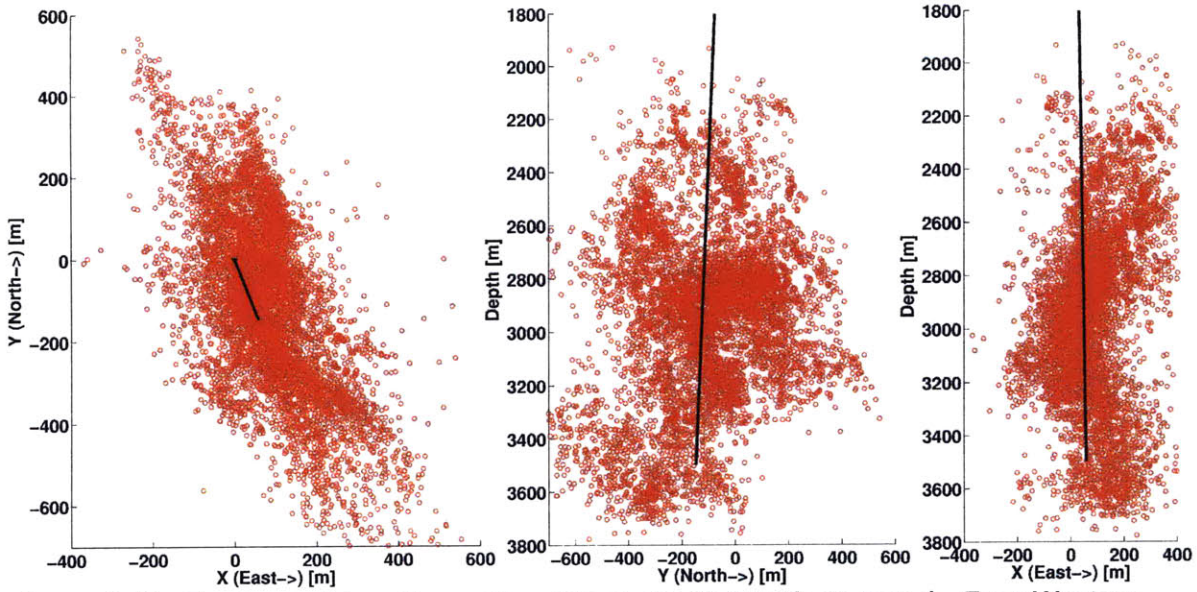

Figure 3.11: Final event locations (Plan View, North-South vs Depth, East-West vs Depth) with the path of the injection well GPK1 (black line) through the reservoir for the results set A.3.

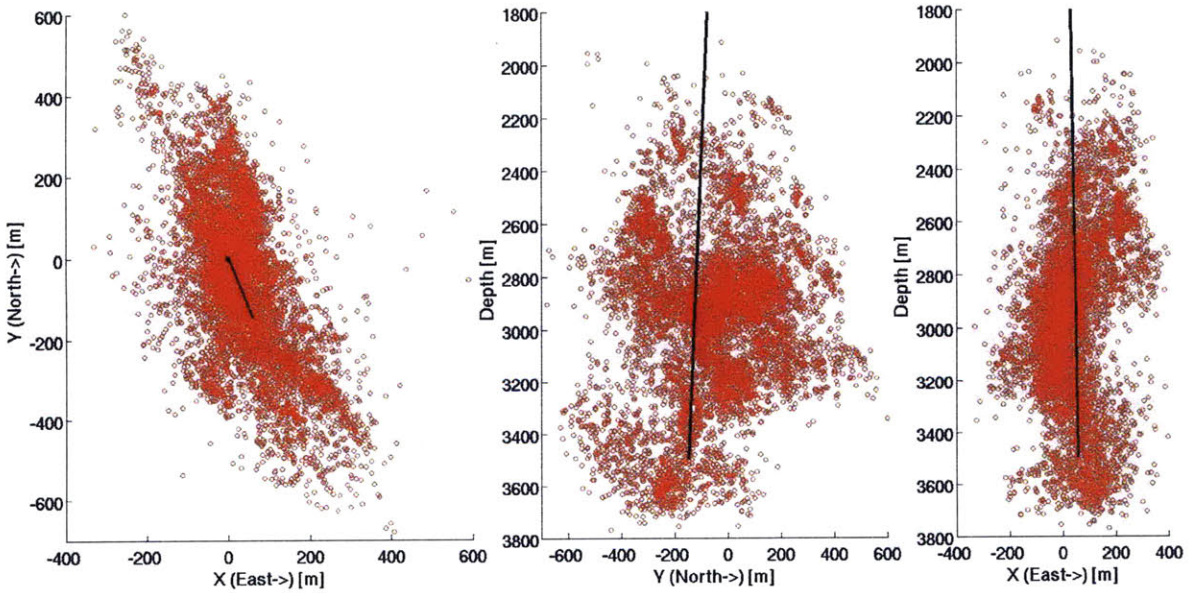

Figure 3.12: Final event locations (Plan View, North-South vs Depth, East-West vs Depth) with the path of the injection well GPK1 (black line) through the reservoir for the results set A.4.

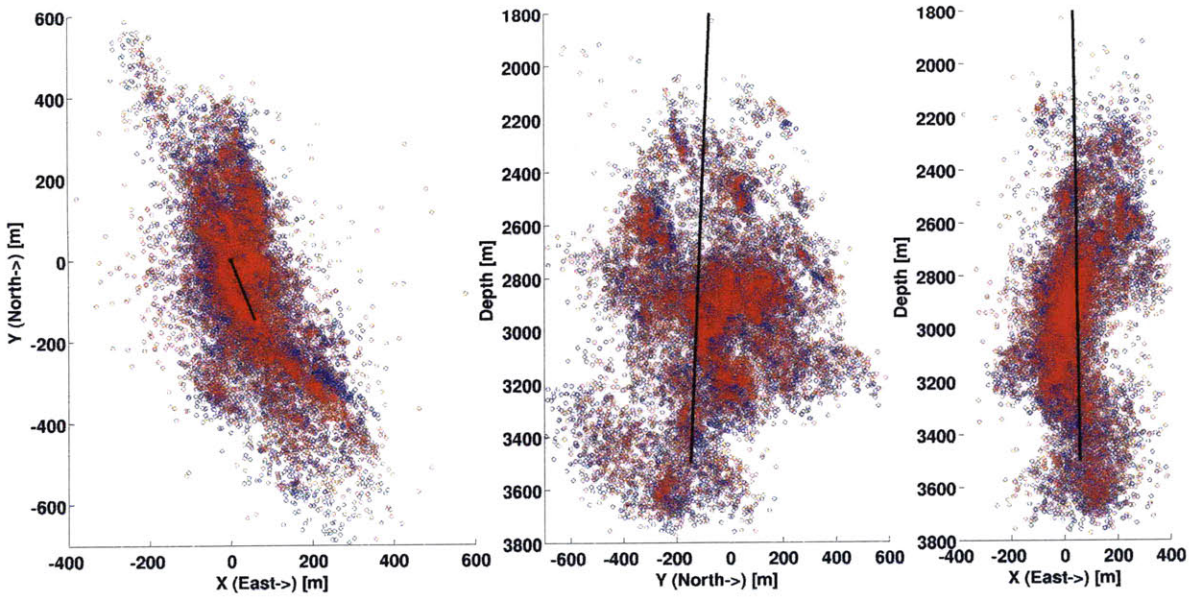

Figure 3.13: Final event locations (red) and original JHD locations (blue) plots (Plan View, North-South vs Depth, East-West vs Depth) with the path of the injection well GPK1 (black line) through the reservoir for the results set A.1.

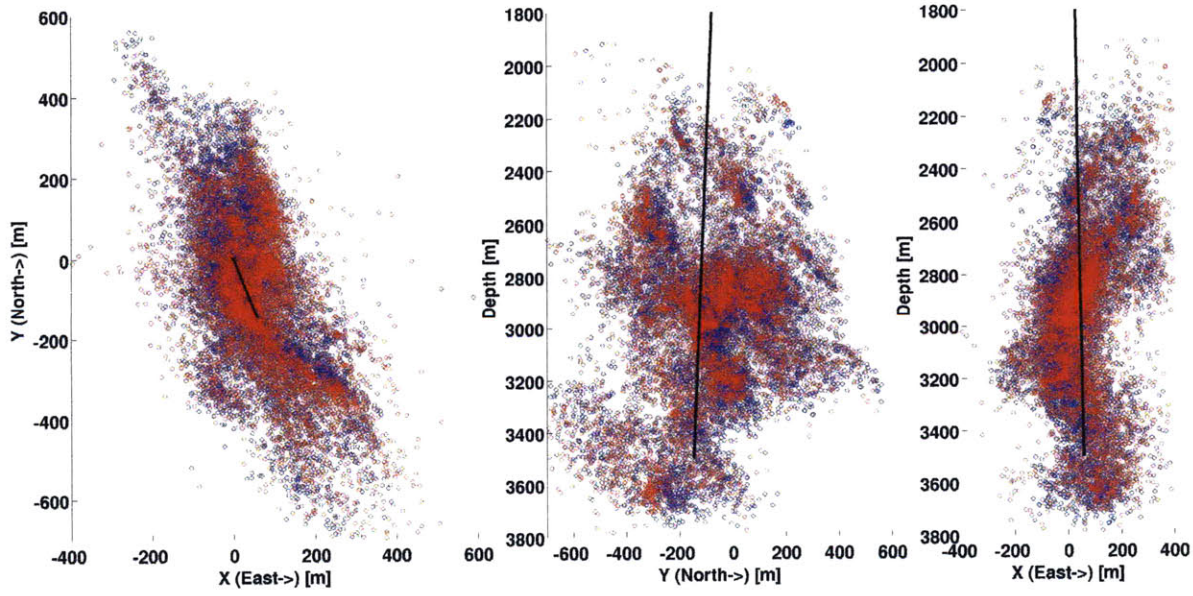

Figure 3.14: Final event locations (red) and original JHD locations (blue) plots (Plan View, North-South vs Depth, East-West vs Depth) with the path of the injection well GPK1 (black line) through the reservoir for the results set A.2.

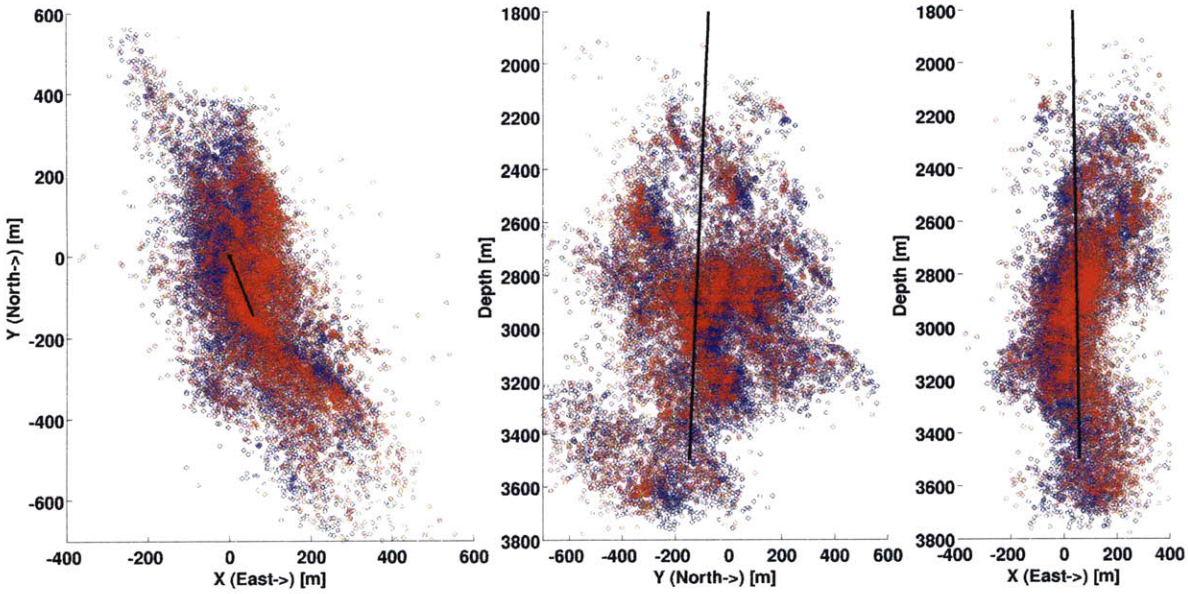

Figure 3.15: Final event locations (red) and original JHD locations (blue) plots (Plan View, North-South vs Depth, East-West vs Depth) with the path of the injection well GPK1 (black line) through the reservoir for the results set A.3.

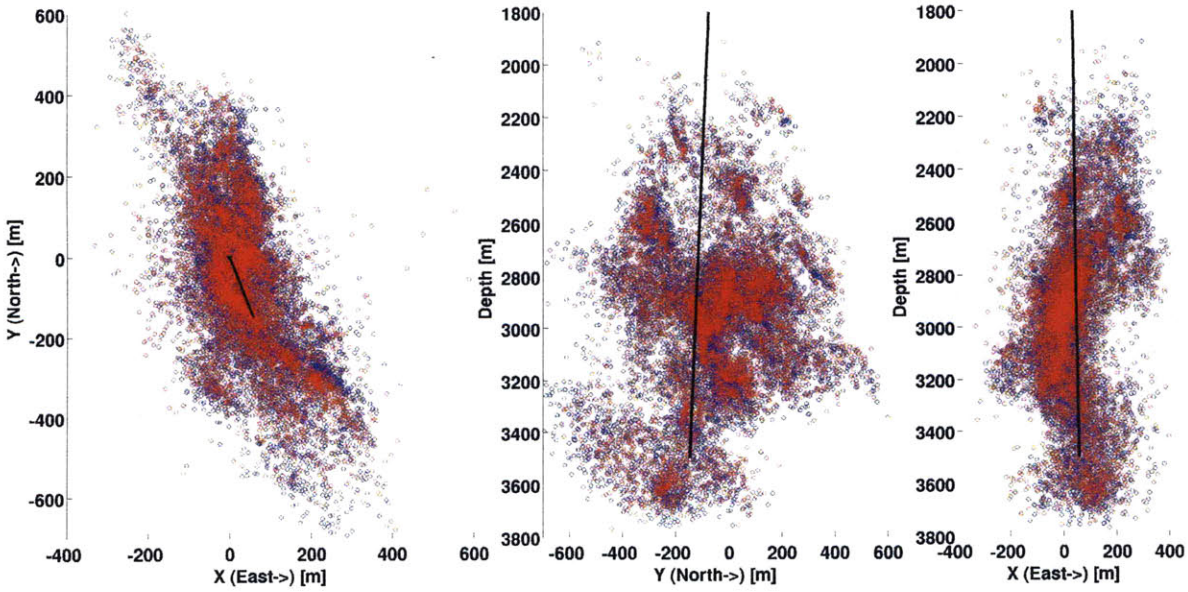

Figure 3.16: Final event locations (red) and original JHD locations (blue) plots (Plan View, North-South vs Depth, East-West vs Depth) with the path of the injection well GPK1 (black line) through the reservoir for the results set A.4.

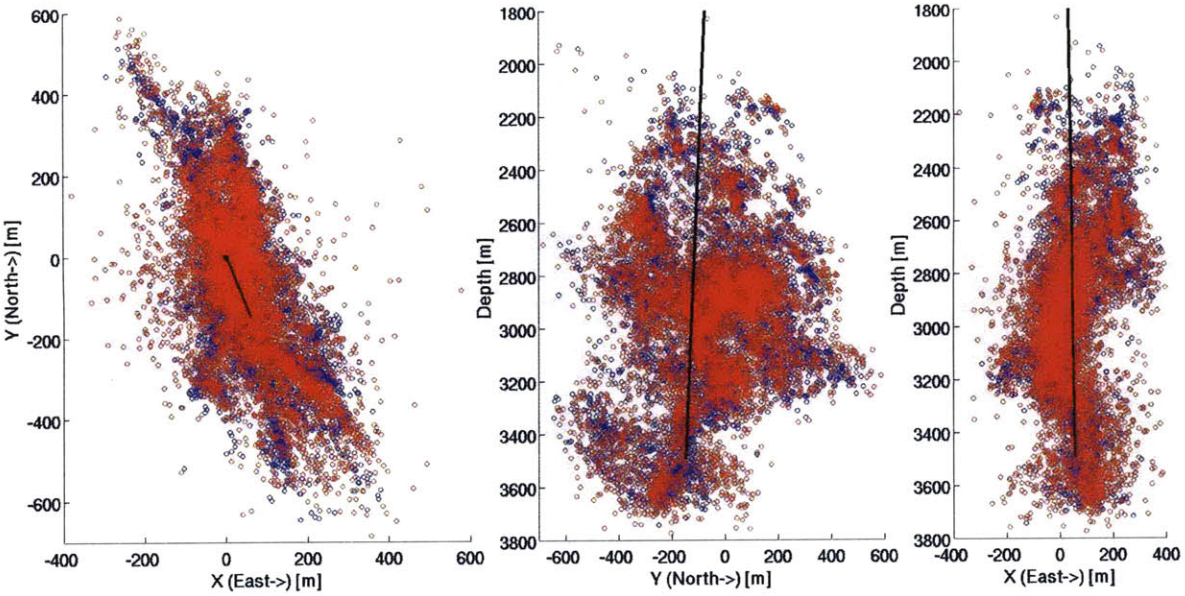

Figure 3.17: Final event locations (red) and original collapsed locations (blue) plots (Plan View, North-South vs Depth, East-West vs Depth) with the path of the injection well GPK1 (black line) through the reservoir for the results set A.1.

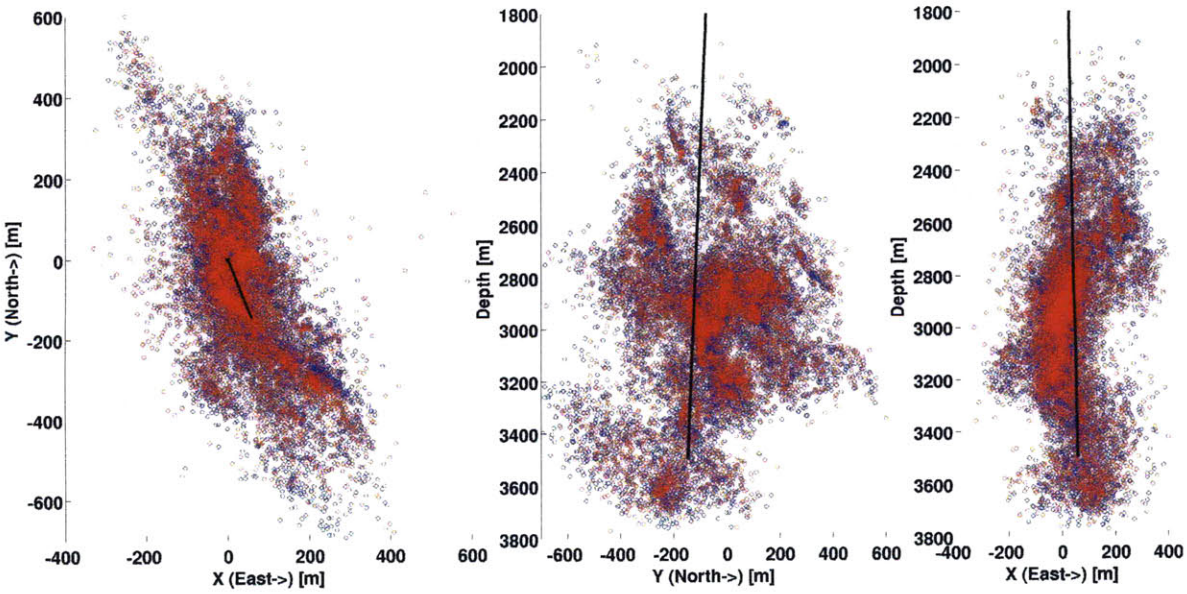

Figure 3.18: Final event locations (red) and original collapsed locations (blue) plots (Plan View, North-South vs Depth, East-West vs Depth) with the path of the injection well GPK1 (black line) through the reservoir for the results set A.4.

3.2.2 Choosing The Smoothing Weight

With the result of the previous section showing that sets A.1 and A.4 produced the most compact clustering of locations out of the four sets of results, two sets of multiple inversion runs were performed (one for A.1 and one for A.4), each using a range of smoothing weight values (1, 1.5, 2, 3, 5, 7.5, 10, 20, 50, 100) in order to find the optimal value which minimized both data residuals while providing a detailed velocity model. For the A.4 group of only differential times additional inversion runs were performed with smoothing weight values 200, 500, and 1000. Note that using increased smoothing weight values in the inversion resulted in smoother velocity models.

Figure 3.19 shows the final RMS of the differential times from cross-correlation (RMSCC) for different values of smoothing. Above a smoothing weight of 3 the RMS remains constant. Figure 3.20 shows the RMS of the the catalog data (RMSCT), which includes both differential and absolute times, for different smoothing weight values. Note that using a smoothing weight of 5 or 7.5 minimized RMSCT. Figure 3.21 shows the differential times only RMS (RMSDIFF) for different values of smoothing weight. Using this figure in conjunction with Figures 3.22 and 3.23, which show the relationship between the RMS of the difference of the final and starting velocity models for the P and S-wave velocity models respectively, an optimal value for the smoothing weight was chosen. Choosing a larger smoothing weight reduced the RMS of the differences between the final and starting model. In other words, the more smoothing was applied, the smaller the difference between the final and starting velocity models which produced a model similar to the one-dimensional starting model. As a result, the optimal value of smoothing was the smallest value that minimized the RMS of the data used in the inversion (differential

and/or absolute times) while obtaining the most detailed model possible, as explained by Zhang and Thurber (2007). Looking at Figures 3.19 through 3.21 while keeping in mind to find the smallest smoothing weight which minimized RMSCC, RMSCT and RMSDIFF, a smoothing weight of 5 was chosen as the best compromise.

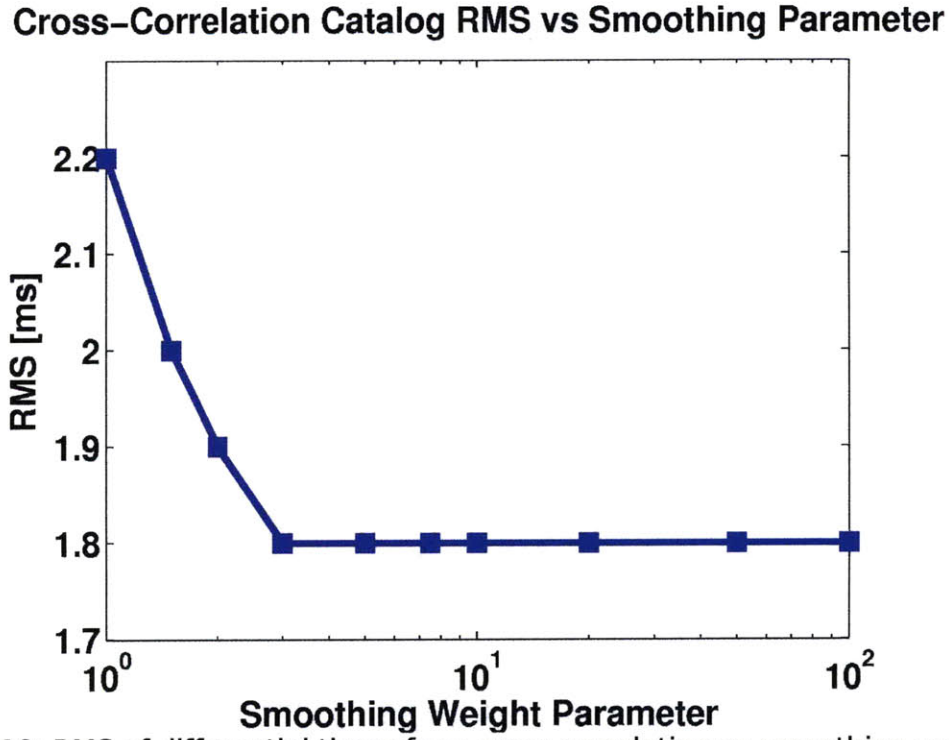

Figure 3.19: RMS of differential times from cross-correlation vs smoothing weight for inversion A.1. Note that the result is identical for inversion A.4.

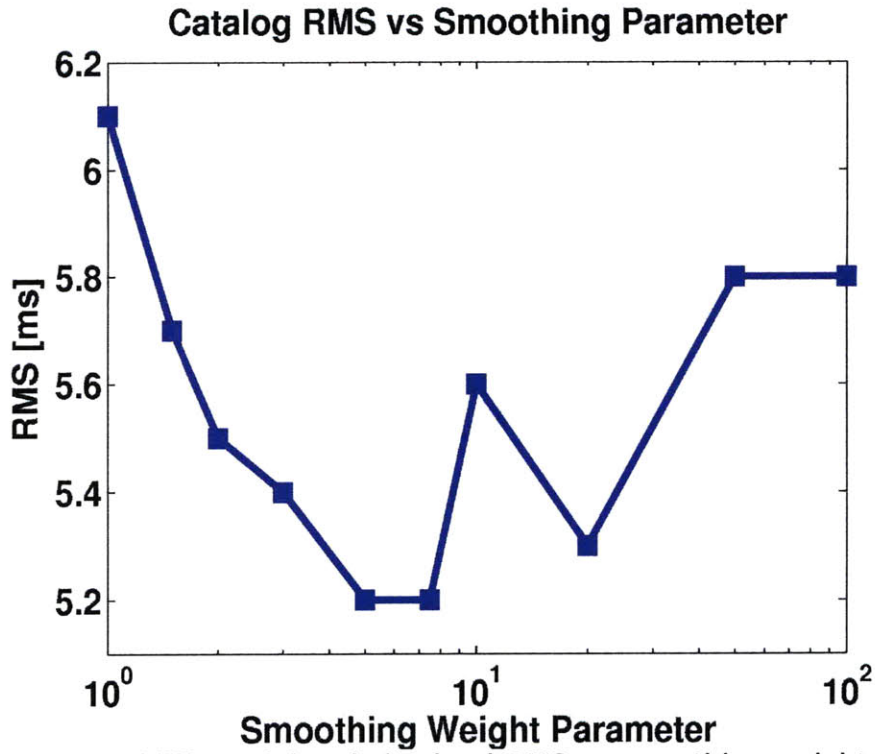

Figure 3.20: Catalog (differential and absolute) RMS vs smoothing weight for inversion A.1.

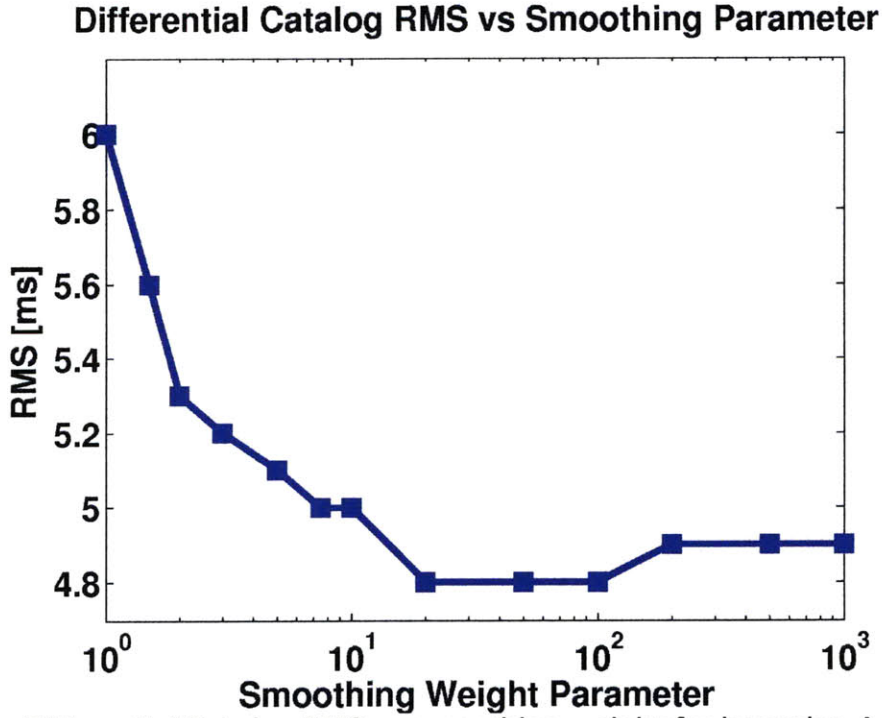

Figure 3.21: Differential Catalog RMS vs smoothing weight for inversion A.4.

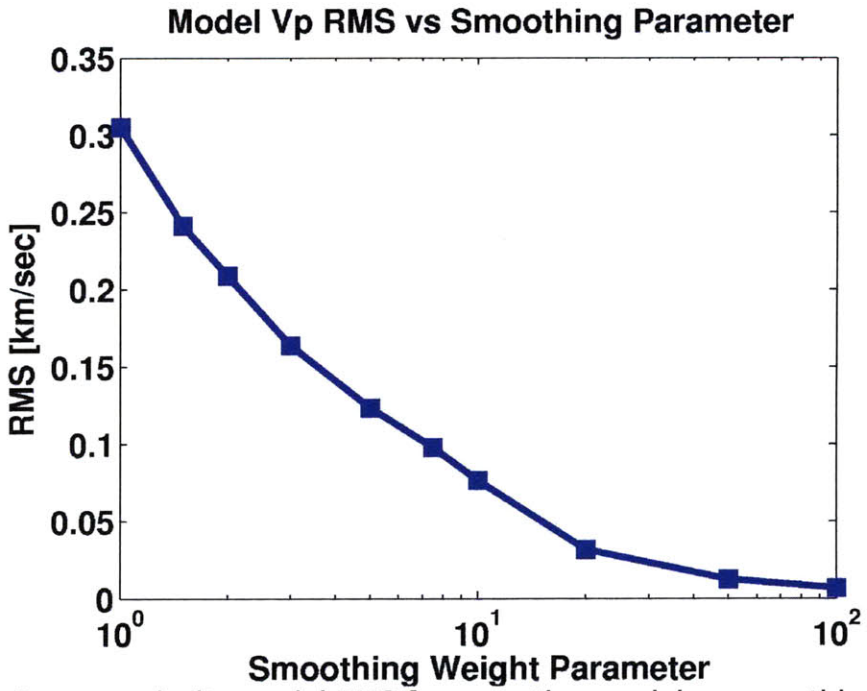

Figure 3.22: P-wave velocity model RMS from starting model vs smoothing weight for inversion A.1.

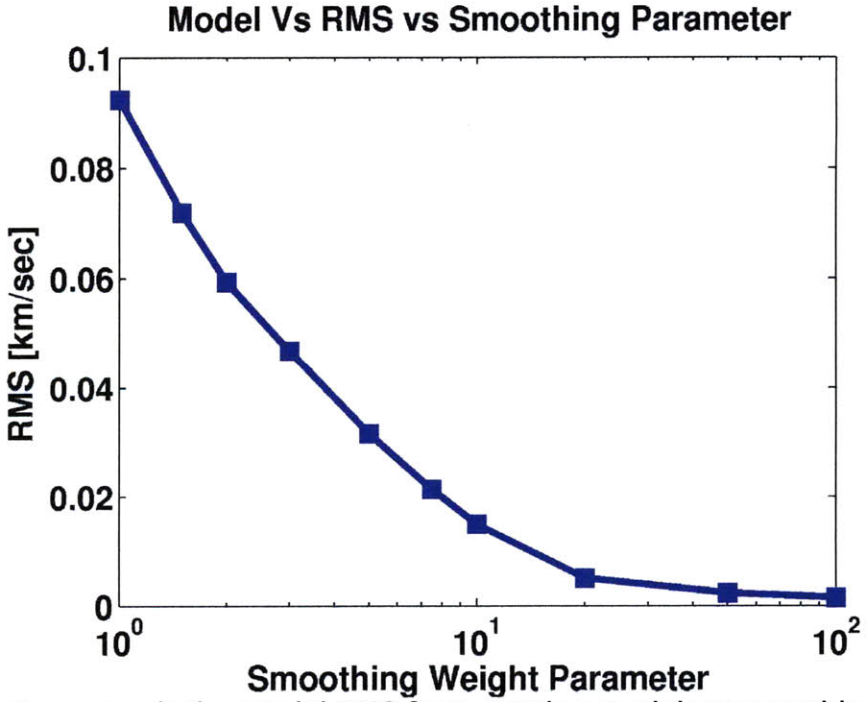

Figure 3.23: S-wave velocity model RMS from starting model vs smoothing weight for inversion A.1.

3.2.3 Selecting the Final Set of Results

Because set A.4 produced the best locations (no shifts like A.2 or A.3 and tighter clustering than A.1) and had the low S-wave velocity zone at 2900 meters depth (absent in A.1) as expected from well logs, we chose to interpret this set. From analyzing the smoothing weight values in the previous section, we decided to interpret set A.4, presented earlier, which was run with smoothing weight set to 5.

3.2.4 DWS Analysis

As described in Chapter 2, the derivative weighted sum (DWS for short) is a qualitative measure of model resolution which looks at the ray sampling density at nodes without regard for the direction the rays travel in. Zhang and Thurber (2007), Toomey and Foulger (1989), and Toomey *et al*. (1994) discuss the use of DWS when applied to real and synthetic data.

Figures 3.24 and 3.25 show the DWS plots for the P and S-waves velocity models. Note that for most of the plotting area there are at least 1000 rays crossing each node. The values are much higher but for ease of visualization the color bar was capped at 1000 rays. Therefore, we believe many rays sample the entire model space.

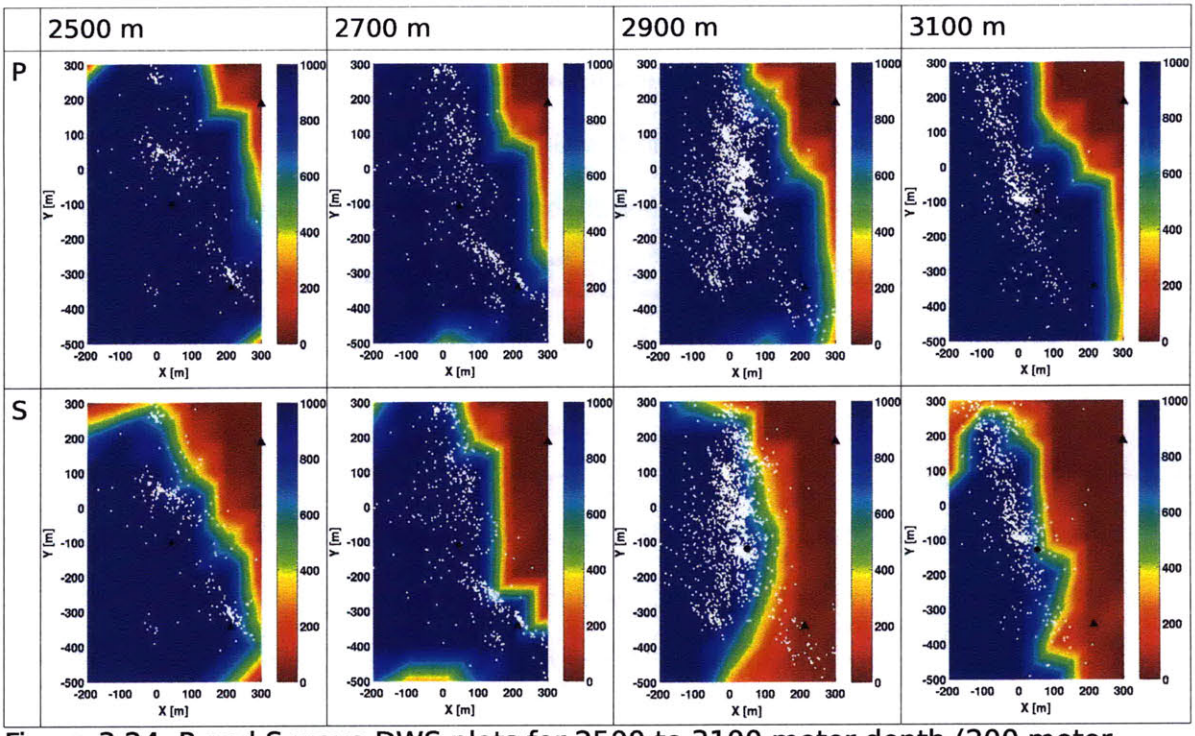

Figure 3.24: P and S-wave DWS plots for 2500 to 3100 meter depth (200 meter intervals).

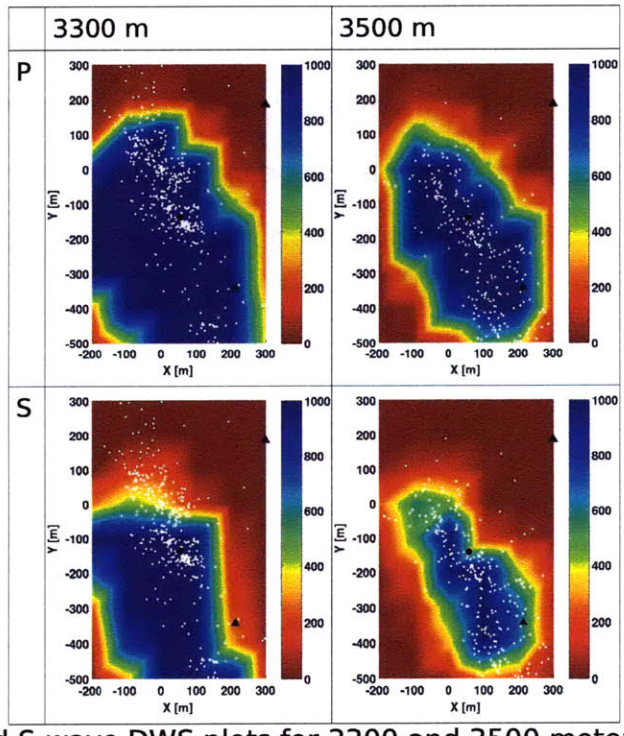

Figure 3.25: P and S-wave DWS plots for 3300 and 3500 meter depths.

3.2.5 Checkerboard Test

Figures 3.26 and 3.27 show the checkerboard used to calculate synthetic absolute and differential catalog times in TomoDD. The checkerboard consisted of alternating low and high velocity regimes having dimensions of 200 meters on a side with velocity perturbations of ±5%. Zones of high/low P-velocity overlayed zones of low/high S-velocity. Figures 3.28 and 3.29 show the results of running the inversion on the non-perturbed one-dimensional velocity model (the same one used for all previously discussed sets of results) with the synthetics obtained from the checkerboard and using the same event locations as the real data with smoothing weight set to 5. Note how the checkerboard pattern is stronger at or near the injection well GPK1 for all tomograms, but especially true for tomograms at 2700 and 3100 meters depth. The trajectories of rays propagating from events to receivers form a cone with the receivers on the periphery of the circular end and events at or near the pointed end. Despite the large number of rays sampling the volume, few rays travel horizontally through the volume near the sides of the cone so the volume near the injection well GPK1 is best resolved and streaking of velocity structure can occur.

Figure 3.30 shows cross-plots of P and S-wave speeds. Note how the relation between P and S-wave velocities has considerable variation in P-wave speed and less variation in S-wave speed for all depths. As depth increases, the range of variation of P-wave speeds decreases while the range of S-wave speed variation stays about constant. Note that both ranges shift from one depth to another with no clear direction of shift with increase in depth.

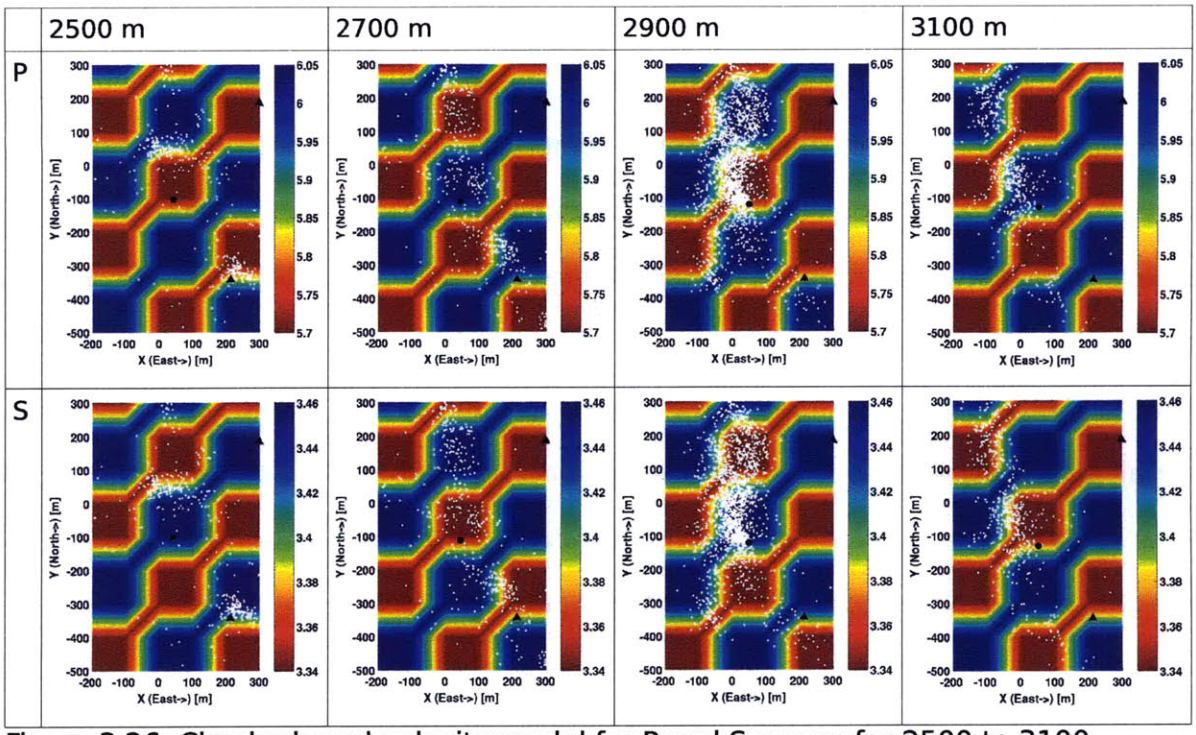

Figure 3.26: Checkerboard velocity model for P and S-waves for 2500 to 3100 meters depth.

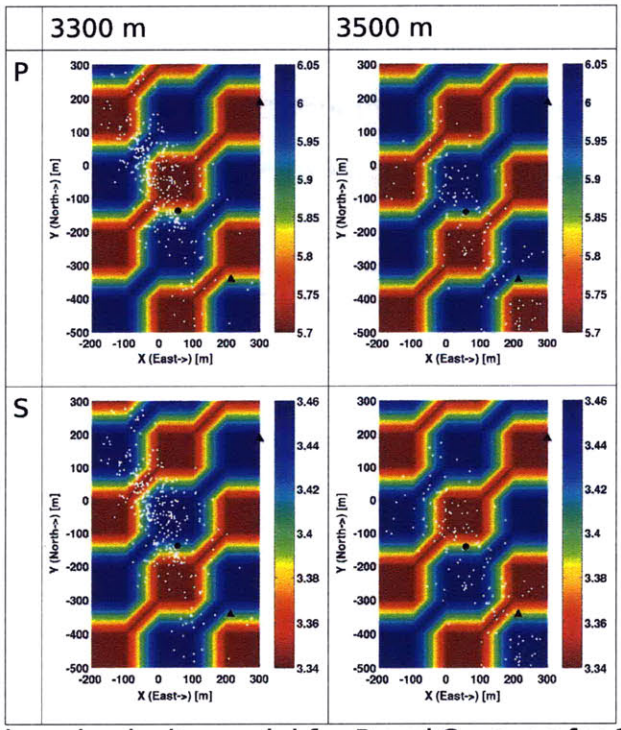

Figure 3.27: Checkerboard velocity model for P and S-waves for 3300 and 3500 meters depth.

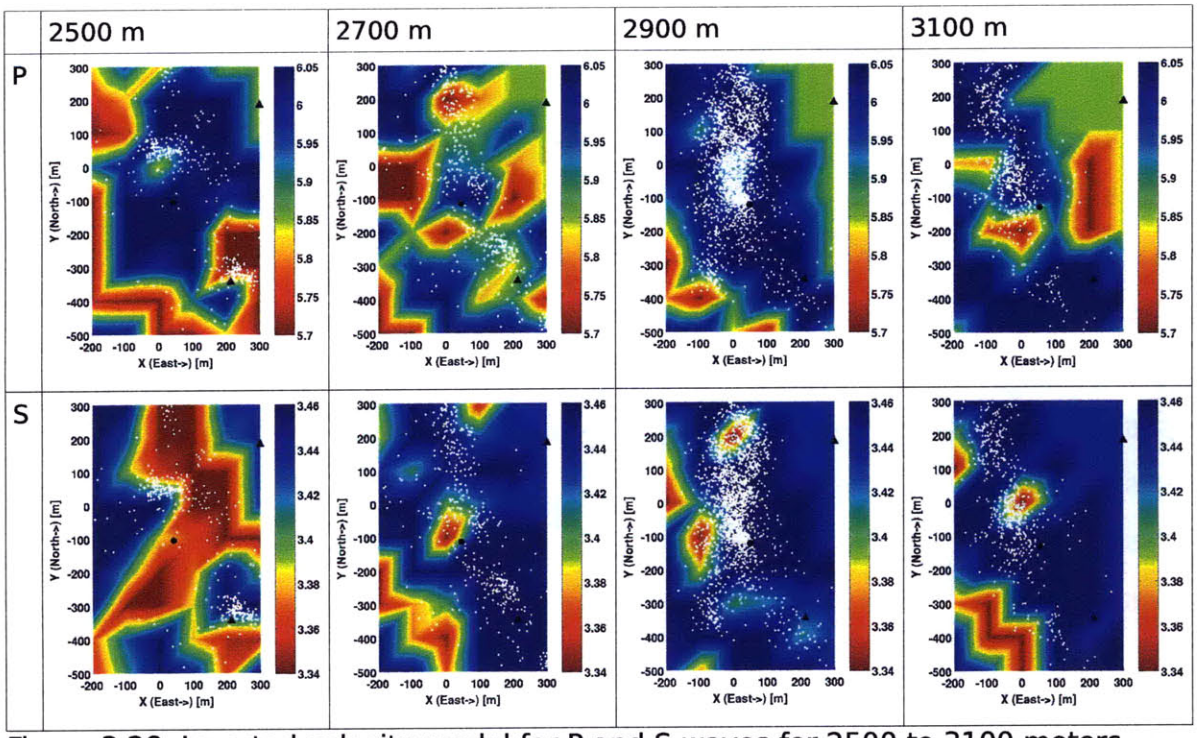

Figure 3.28: Inverted velocity model for P and S-waves for 2500 to 3100 meters depth.

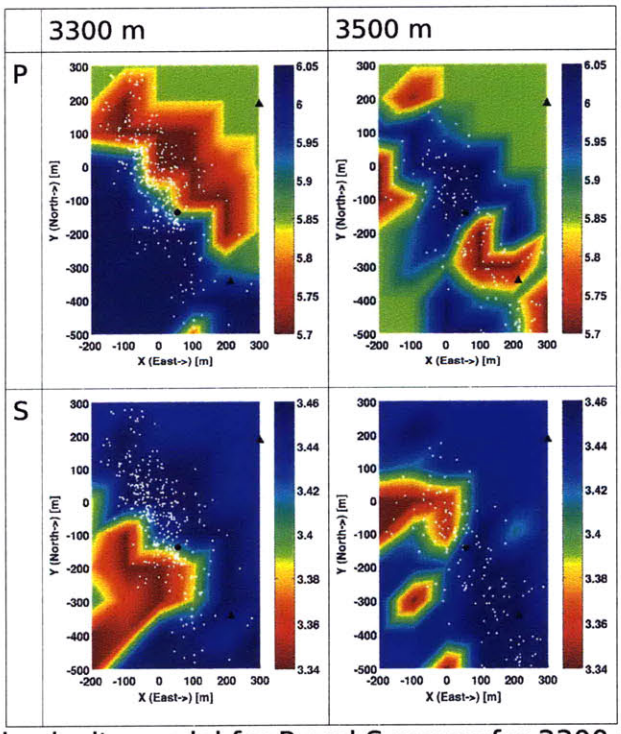

Figure 3.29: Inverted velocity model for P and S-waves for 3300 and 3500 meters depth.

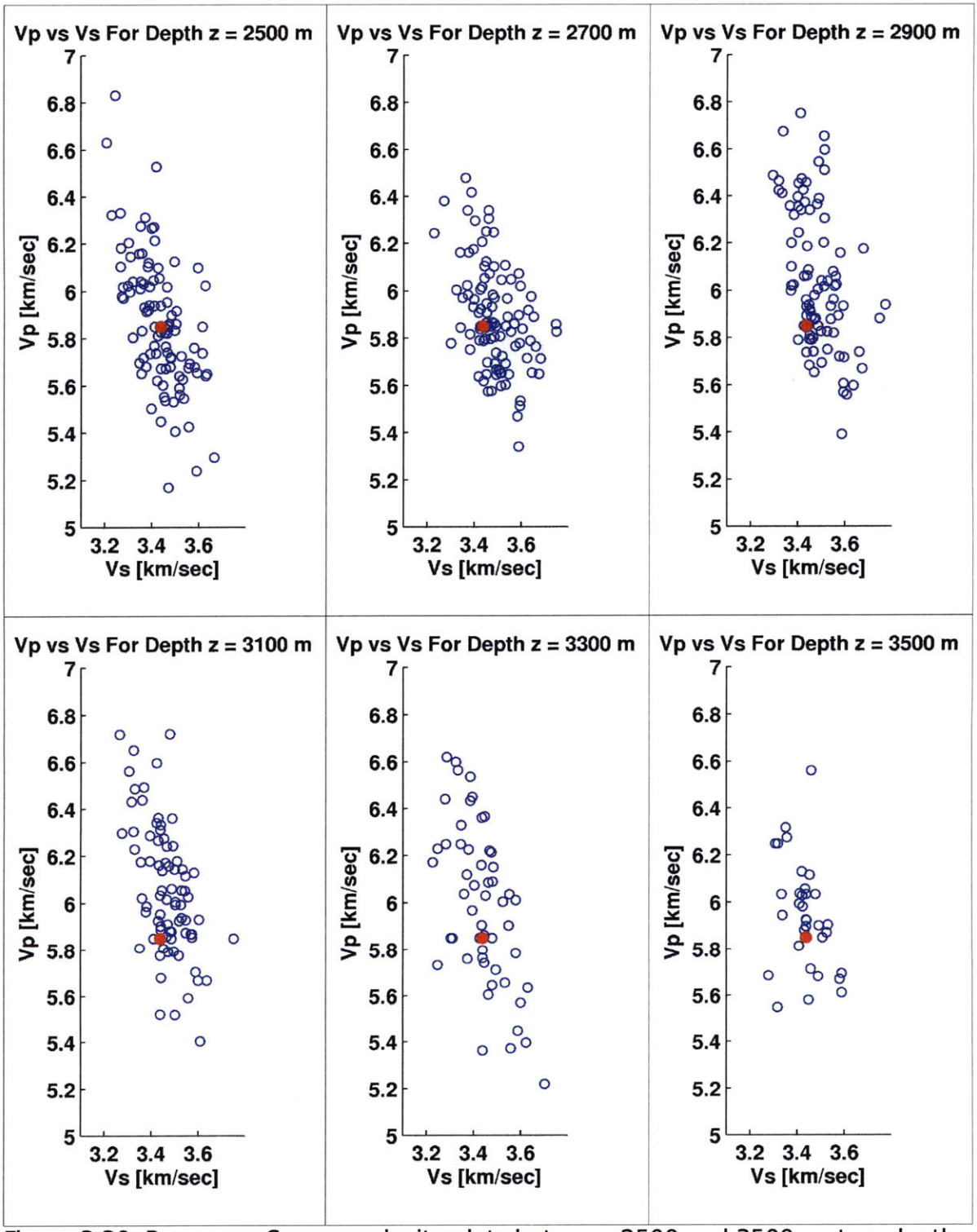

Figure 3.30: P-wave vs S-wave velocity plots between 2500 and 3500 meters depth for the checkerboard test. Starting model velocity denoted by a red dot.

3.3 Interpretation

A simple framework for interpreting the results begins with the P and S-wave speeds (Vp and Vs) which depend on the shear modulus μ, bulk modulus K, and density ρ (together known as the elastic moduli) of a material. The bulk modulus is also known as the incompressibility of a material and the higher the value, the harder it is to compress the material. The shear modulus is also known as the rigidity of a material. The larger a material's shear modulus, the larger its resistance to shear.

$$V_p = \sqrt{\frac{K + 4/3\mu}{\rho}} \tag{3.1}$$

$$V_s = \sqrt{\frac{\mu}{\rho}} \tag{3.2}$$

The effective elastic moduli (i.e. moduli of the rock matrix and pore inclusions combined) depend on the density of the rock, presence of pores, fluid in the pores, and other factors. According to Toksöz *et al.* (1976) the wave speeds also depend on the porosity (percent of volume which is empty) and the shape of the pores (i.e. aspect ratio of the pores) in the rock. For rocks with flat pores, such as in the case of igneous rocks like granite, the aspect ratios are small (on the order of 10^{-4}) and are affected more by the presence of fluid or gas than rock with rounder, more spherical pores, and therefore higher aspect ratios. According to Evans *et al.* (2005) hydro-fracturing experiments in crystalline/igneous rock, such as at Soultz and many other geothermal fields, produces shear type fractures as the main permeability creating mechanism. Because of the enhanced changes in velocities for rocks with small aspect ratios compared to those with large aspect ratios, described in Figure 1 of Toksöz *et al.* (1976), a tomographic method like TomoDD should be well poised to

detect the presence of fluid or gas in geothermal reservoirs.

In tomograms of depth slices shallower than 2800 meters, shown in Figures 3.3 and 3.4, the injection well GPK1 is centered on a low P-wave, and near-to-background S-wave velocity zone, which is consistent with the theoretical and experimental results of Toksöz *et al.* (1976), for a dry but fractured crystalline rock. Starting at about 2900 meters depth (Figure 3.5) the zone centered on GPK1 changes to high P-wave and low S-wave velocity, which is expected when new fractures are generated and filled with water. Since water has a smaller shear modulus than the rock matrix, the S-wave velocity decreases.

The explanation for why the P-wave velocity increases for the wet, stimulated rock mass compared to non-stimulated, dry rock is more complicated. Note that the term dry can apply to gas (i.e. steam, air) filled rock. According to Toksöz *et al.* (1976), granite contains pores with low aspect ratio and few of them which translates to a low porosity (percent volume occupied not occupied by solid granite). With that in mind, two limiting cases must be understood: the case of stimulated granite with dry pores and fractures (high porosity) and the case of non-stimulated, wet granite (low porosity). For the former case because the granite has been stimulated, it's porosity will be higher than for the later case of non-stimulated, wet granite. Because of the higher porosity, each unit volume of granite will contain less solid granite and, as a result, the effective moduli will all decrease with the bulk modulus will decreasing the most, yielding slower P-waves. We consider this as the lower limit on P-wave velocity, in our construct. On the other end of the spectrum, the low porosity (non-stimulated), wet granite will have the highest P-wave velocity because each unit volume of the rock will contain the highest amount of solid granite and the few pores it does have are filled with water

instead of gas (e.g. steam or air). We consider this as the upper limit on P-wave velocity, in our construct. In between these two limiting cases exist the case of stimulated (high porosity), wet granite and the case of non-stimulated (low porosity), dry granite. Because the elastic moduli are all higher for the high porosity, wet granite case, we believe this case has a higher P-wave velocity than the low porosity, dry granite case but a lower P-wave velocity than the upper limiting case. As a result, we expect the stimulated, high porosity, wet granite case to have higher P-wave velocity than later case of non-stimulated, low porosity, dry granite. However a more detailed theoretical and experimental analysis is needed in order to come to a firm conclusion as to the differences in P-wave velocities among these four cases.

Because the open hole depth ranged from 2850 to 3600 meters and spinner logs showed that about 60% of water losses occurred above 3100 meters, the low S-wave velocity zone in conjunction with a high P-wave velocity zone is an encouraging result. These results are also consistent with injection well GPK1 core analysis which showed that hydrothermal alteration was responsible for shear fractures present between 2850 and 3000 meter depths and also consistent with post-stimulation fracture mapping which showed a large density of fractures in the upper half of the open hole depth, as reported by Evans *et al.* (2005) and as shown in Figure 1.1. Refer to Figure 3 of Evans *et al.* (2005) for a detailed summary of the hydrothermal alteration at depth, flow profiles, fracture densities, and fluid injection schedule.

Evans *et al.* (2005) also explain how pre-stimulation fluid loss occurred at a large fault at 3490 meters depth with the same hydrothermal alteration as the fractures at shallower depths. They claim this alteration became the path of least

resistance for the formation of new fractures during the stimulation experiment. Spinner logs initially showed fluid loses in the upper half of the reservoir and then shifted deeper in the reservoir before going back to the shallower hydrothermally altered zone. Evans *et al.* (2005) conclude that fracture aperture changes at the shallower depths became permanent after that part of the injection.

Cross-plots of P-wave speed versus S-wave speed are displayed in Figure 3.31. Note how the relation between P-wave and S-wave velocities shows considerable variation in P-wave speed and little variation in S-wave speed in the shallower portions of the reservoir. The cross-plots for the checkerboard test showed this same relationship but for all depths. As depth increases in the reservoir, more S-wave velocity variation occurs unlike in the checkerboard test in which the range of S-wave speed variation stayed about the same at all depths. It is also interesting to note that the large variation in P-wave speed remains the same at about all depths unlike for the checkerboard test cross-plots. All this along with the direction in which the S-wave variation occurs (towards lower speed) at depths below 2900 meters is as we expected from the discussion in the previous paragraphs.

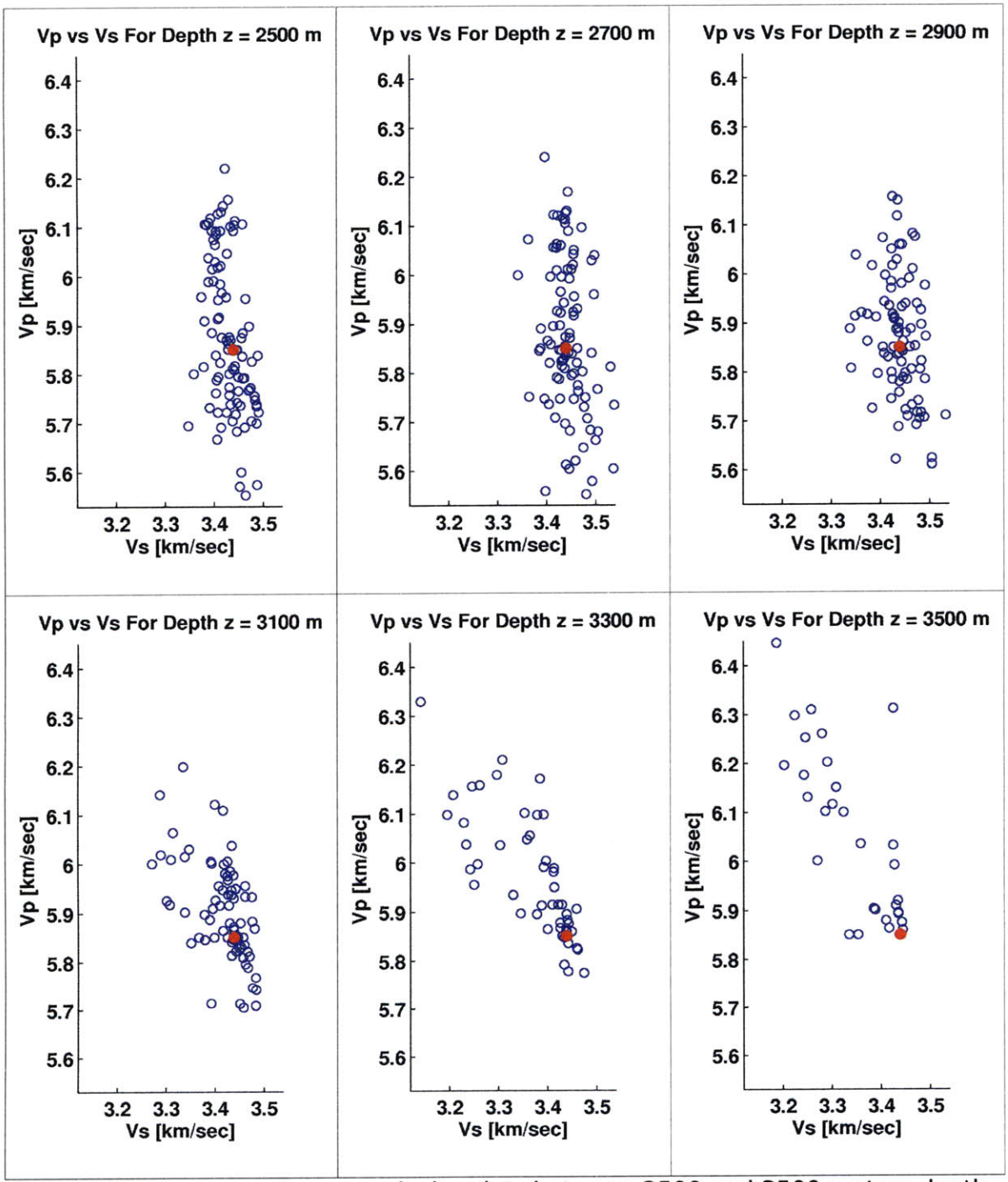

Figure 3.31: P-wave vs S-wave velocity plots between 2500 and 3500 meters depth for the results set A.4. Starting model velocity denoted by a red dot.

CHAPTER 4

CONCLUSION

4.1 Conclusion

The September and October 1993 hydraulic stimulations of the Soultz EGS reservoir produced over 13000 microseismic events recorded at four stations. These data were used in the double-difference tomography method of Zhang and Thurber (2003), in which we used both relative and absolute arrival times, to study the velocity structure at depth in the reservoir. This method provides advantages over conventional tomography by combining the precision provided by relative times and the accuracy provided by absolute times to simultaneously invert for event locations and a three-dimensional velocity model.

The results from applying the double-difference tomography method show some correlations between seismic events and velocity structures at depth. The tomograms for depth slices centered at and below 2900 m clearly show a low S-wave velocity zone over the region believed to have been infiltrated by fluid, as expected by theoretical and experimental results of Toksöz *et al*. (1976), and a high P-wave velocity zone over the same region. These results are also in agreement with the well logs reported in detail by Evans *et al.* (2005) and Dyer *et al*. (1994). These correlations occur for both P and S-wave models but less clearly for P, in agreement with the results of Block *et al*. (1994). This method produced a more compact grouping of event locations with a much smaller RMS residual than the starting JHD locations obtained from Tohoku University that approach the structural detail of the collapsed locations also obtained from Tohoku University, while doing away with the assumptions needed to perform collapsing.

In a nutshell, the results are encouraging and provide motivation for future work using the same double-difference method applied to Soultz and other data sets from geothermal reservoir studies.

4.2 Recommendations for Future Work

Here, in no particular order, we provide a list of recommendations for future work using our results.

1. Based on our results by using the double-difference tomographic method developed by Zhang and Thurber (2003), we recommend that our resulting velocity model be used in conjunction with a migration technique such as Generalized Radon Transform (GRT) migration, which is known to resolve structure at a higher level of detail than the smooth transitions resolved by tomography (Zhang *et al.*, 2009), or off-the-shelf Kirchoff migration.
2. The signal-to-noise ratio of the data may be improved by applying more aggressive filtering techniques. This could also do away with so many extra correlations for station 4601 compared to the other stations, as described in Chapter 2.
3. Sub-horizontal components of the data can be examined as these can sometimes resolve S-waves better than the vertical component used in this study, thereby producing more accurate S-wave arrival time picks.
4. Instead of a checkerboard, a cylindrical or ellipsoidal velocity anomaly oriented with long axis parallel to the Z-axis can be used as a more practical geometry to test TomoDD's ability to resolve velocity structures. A vertically oriented velocity anomaly is recommended as we expect that the source-receiver orientation of the 1993 Soultz EGS experiment can produce vertical

streaking in the final velocity model.

5. Temporal variation in data and model residuals should be studied to understand how well the final velocity model fits data at different times in the stimulation experiment. This could lead to a time-lapse tomographic analysis using TomoDD.

APPENDIX A

FULL SETS OF RESULTS

A.1 Data Results Using Calibration Shot Corrections

The first set of results were calculated using all the available data (absolute times, differential catalog times, and differential cross-correlation times) and using station corrections, applied to the absolute times, obtained from the calibration shot survey of Dyer *et al.* (1994). These calibration shots were performed at a depth of 3360 meters in the injection well GPK1 and resulted in the station corrections shown in Table A.1. The results shown in Figures A.1 through A.12 were obtained using a smoothing weight of 5 for each direction (X,Y,Z) and all other parameter values shown in Figure 2.24. Figure A.13 shows the relocated event locations at the end of the inversion.

Sensor	P-Delay (ms)	S-Delay (ms)
4550	0	0
4601	17	19
4616	5.5	7
hyd1	-3	0

Table A.1: Delay times, also known as station corrections, from a calibration shot survey performed by Dyer *et al.* (1994).

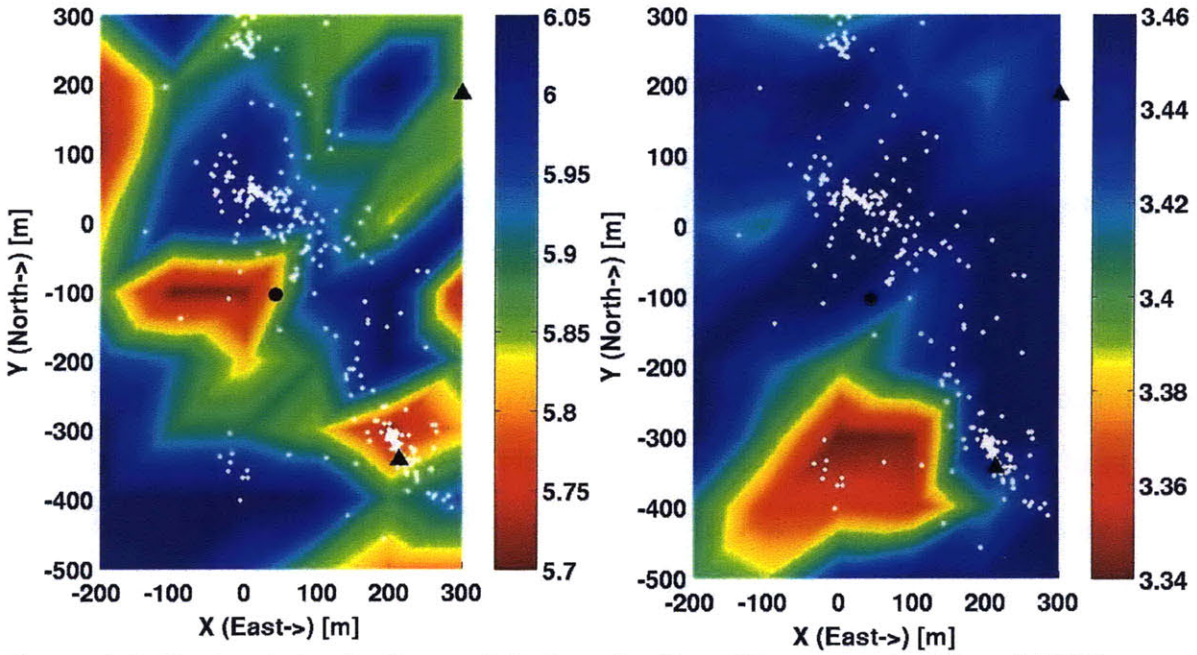

Figure A.1: Horizontal velocity model slices for P and S wave velocities at 2500 meters depth in km/sec. Black circle denotes the position of the injection well GPK1. Black triangles show the locations of station 4550 (upper right) and hyd1 (lower right). White dots denote final earthquake locations within fifty meters depth.

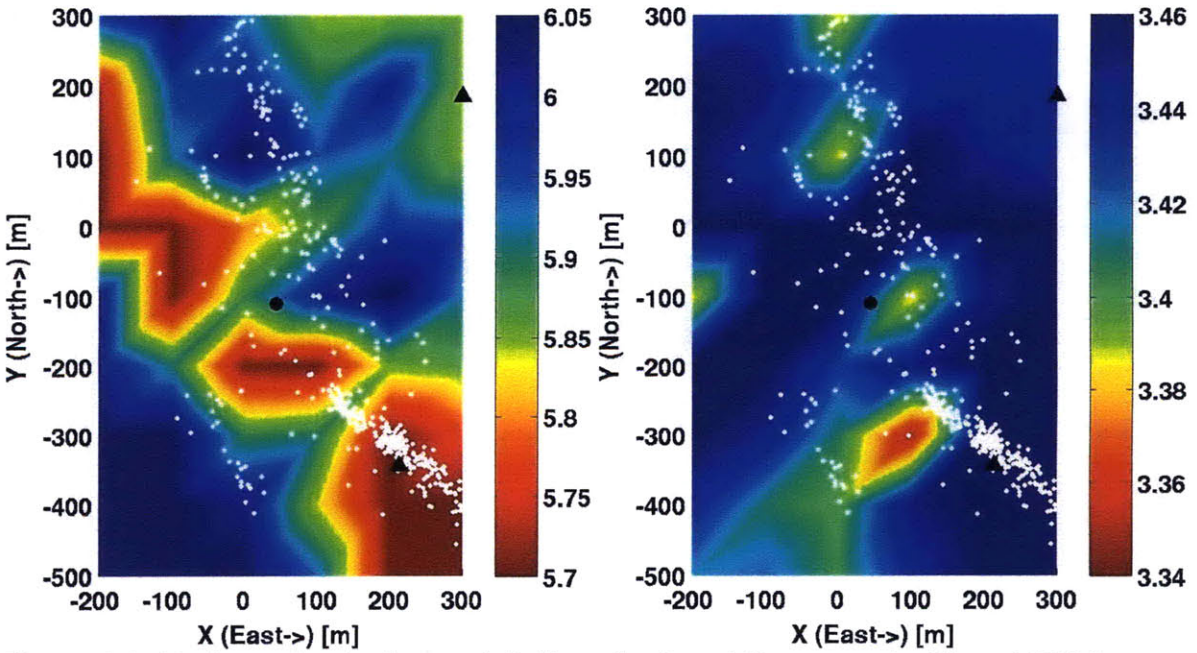

Figure A.2: Horizontal velocity model slices for P and S wave velocities at 2600 meters depth in km/sec. Black circle denotes the position of the injection well GPK1. Black triangles show the locations of station 4550 (upper right) and hyd1 (lower right). White dots denote final earthquake locations within fifty meters depth.

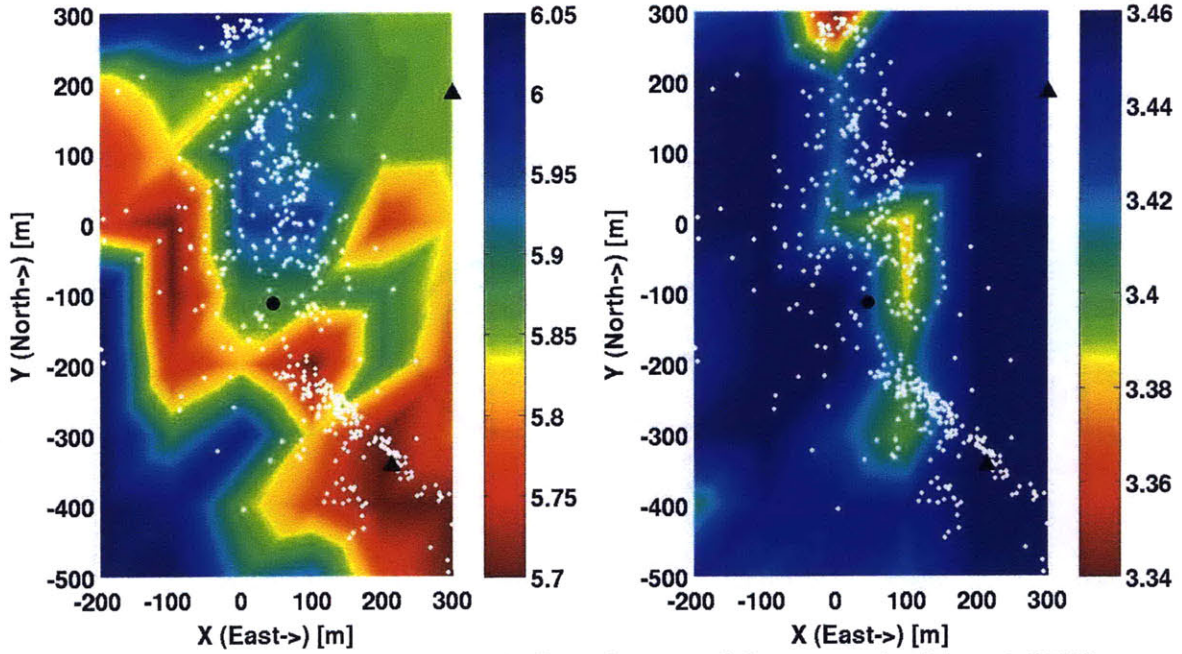

Figure A.3: Horizontal velocity model slices for P and S wave velocities at 2700 meters depth in km/sec. Black circle denotes the position of the injection well GPK1. Black triangles show the locations of station 4550 (upper right) and hyd1 (lower right). White dots denote final earthquake locations within fifty meters depth.

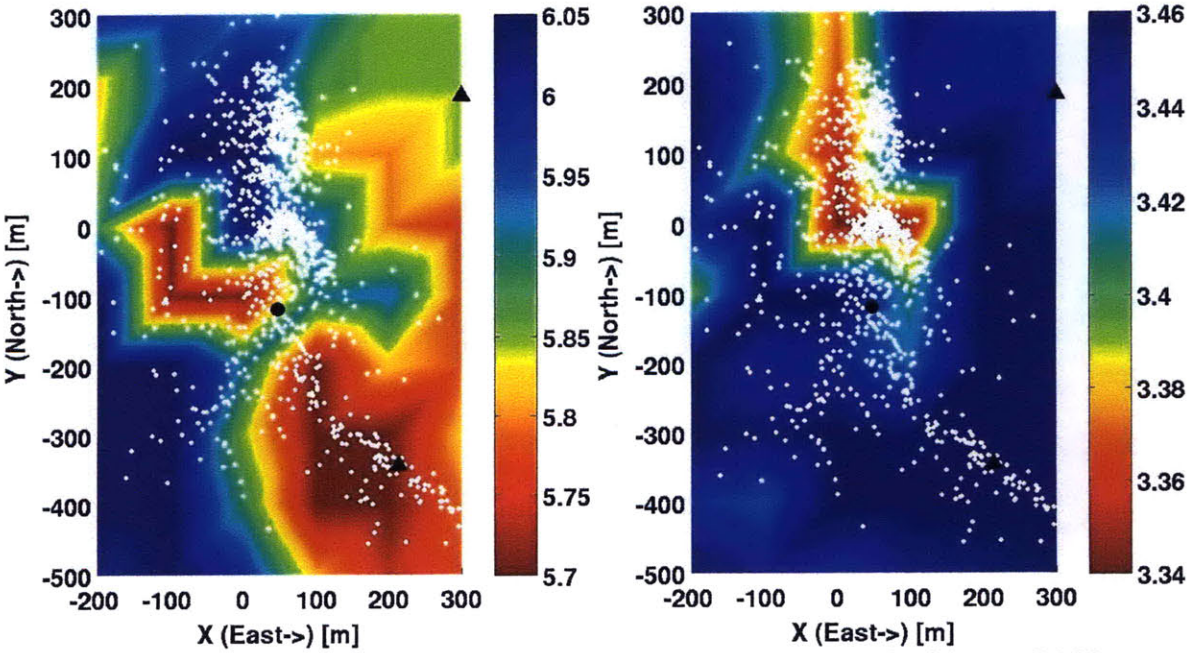

Figure A.4: Horizontal velocity model slices for P and S wave velocities at 2800 meters depth in km/sec. Black circle denotes the position of the injection well GPK1. Black triangles show the locations of station 4550 (upper right) and hyd1 (lower right). White dots denote final earthquake locations within fifty meters depth.

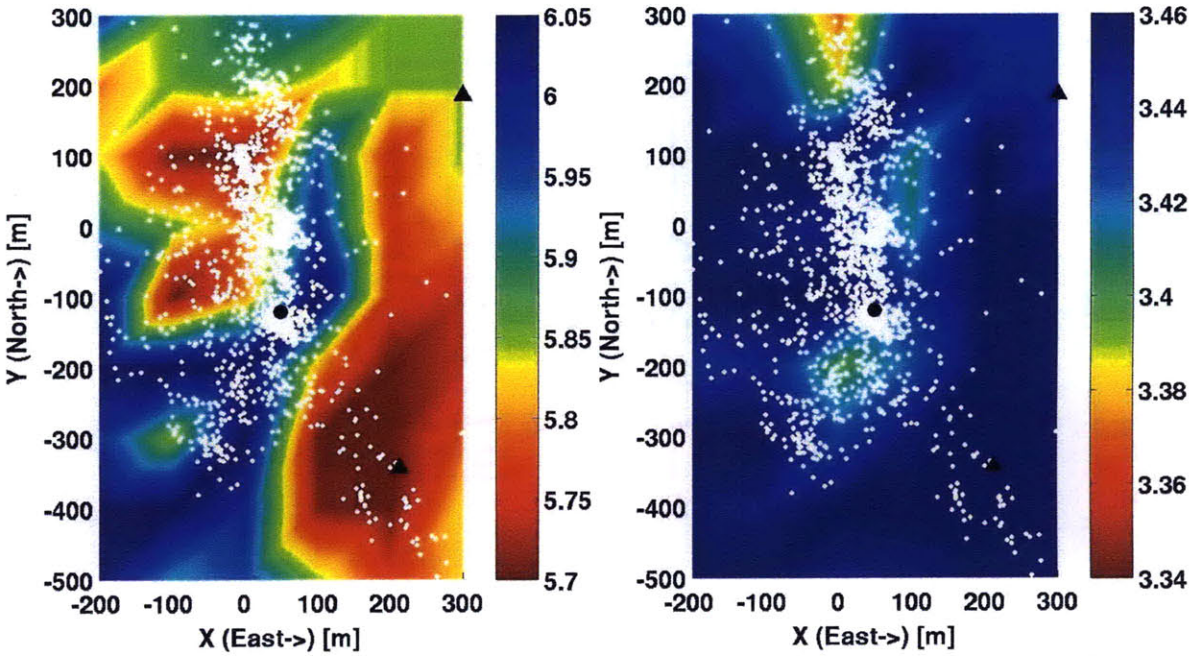

Figure A.5: Horizontal velocity model slices for P and S wave velocities at 2900 meters depth in km/sec. Black circle denotes the position of the injection well GPK1. Black triangles show the locations of station 4550 (upper right) and hyd1 (lower right). White dots denote final earthquake locations within fifty meters depth.

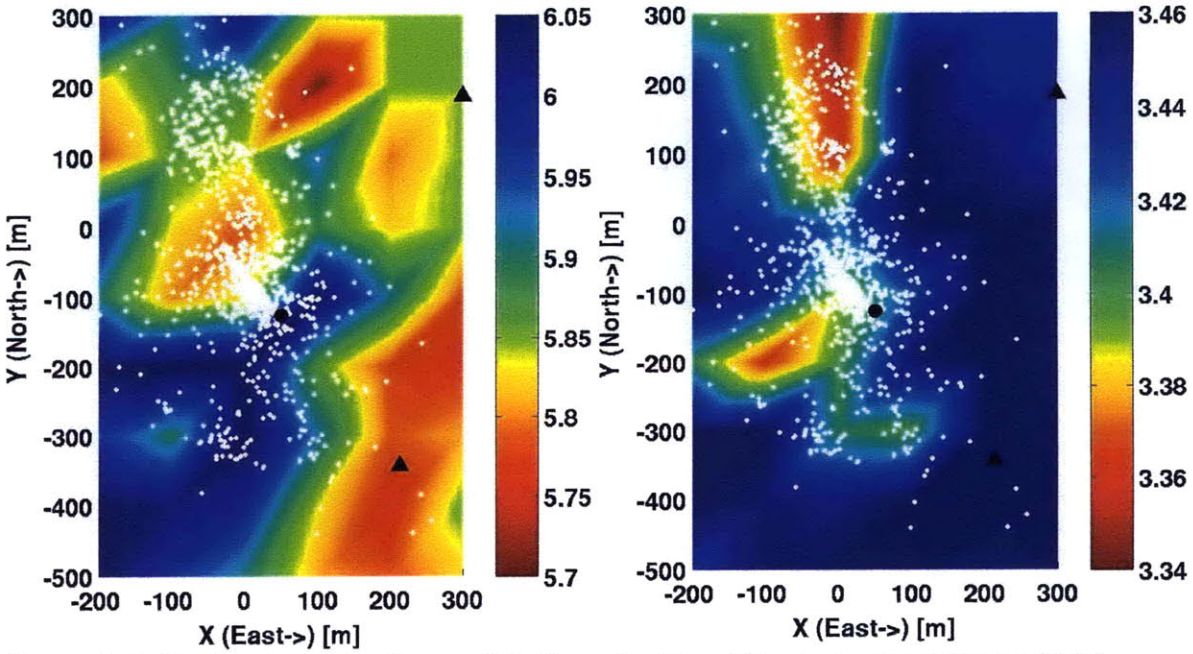

Figure A.6: Horizontal velocity model slices for P and S wave velocities at 3000 meters depth in km/sec. Black circle denotes the position of the injection well GPK1. Black triangles show the locations of station 4550 (upper right) and hyd1 (lower right). White dots denote final earthquake locations within fifty meters depth.

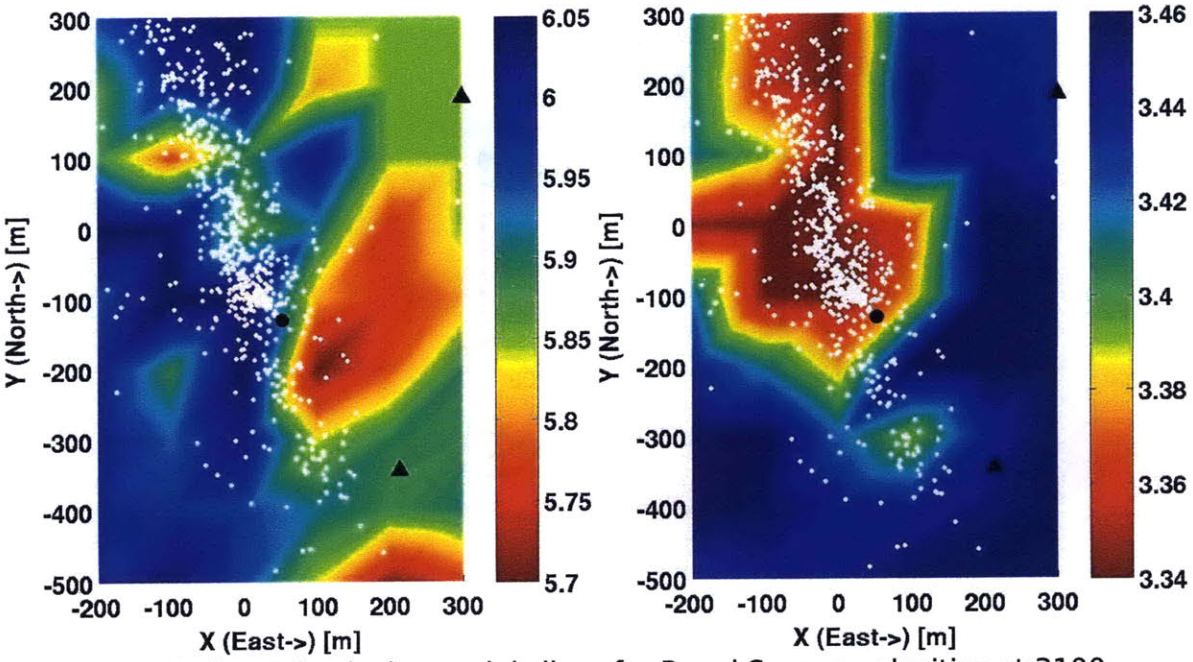

Figure A.7: Horizontal velocity model slices for P and S wave velocities at 3100 meters depth in km/sec. Black circle denotes the position of the injection well GPK1. Black triangles show the locations of station 4550 (upper right) and hyd1 (lower right). White dots denote final earthquake locations within fifty meters depth.

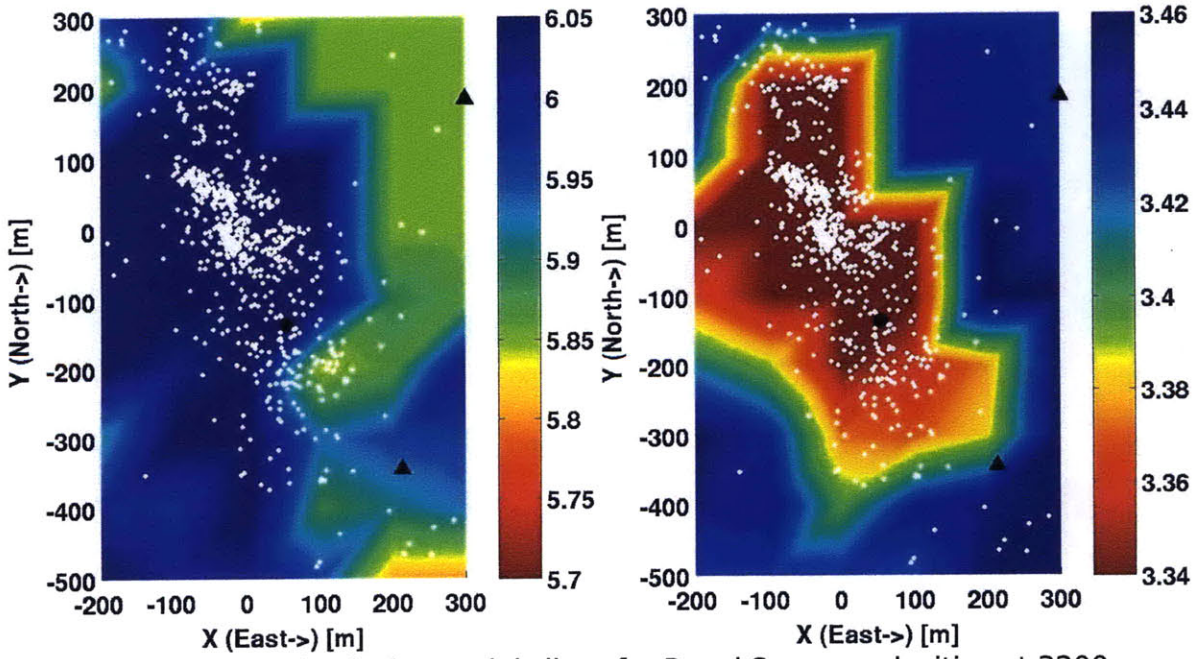

Figure A.8: Horizontal velocity model slices for P and S wave velocities at 3200 meters depth in km/sec. Black circle denotes the position of the injection well GPK1. Black triangles show the locations of station 4550 (upper right) and hyd1 (lower right). White dots denote final earthquake locations within fifty meters depth.

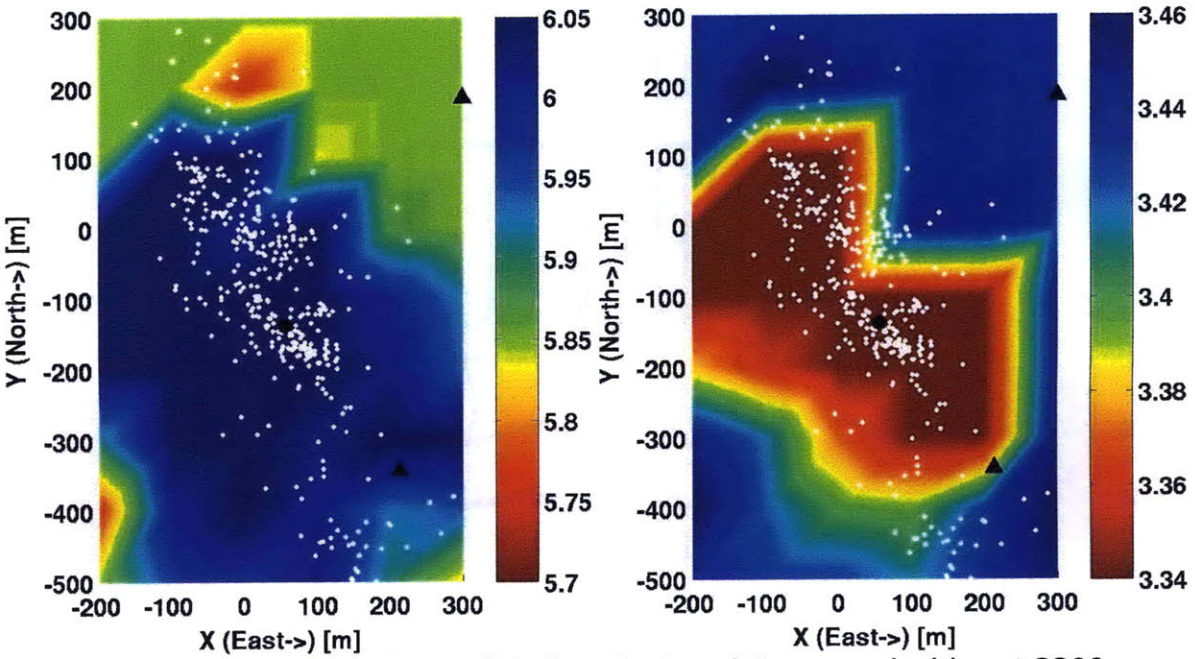

Figure A.9: Horizontal velocity model slices for P and S wave velocities at 3300 meters depth in km/sec. Black circle denotes the position of the injection well GPK1. Black triangles show the locations of station 4550 (upper right) and hyd1 (lower right). White dots denote final earthquake locations within fifty meters depth.

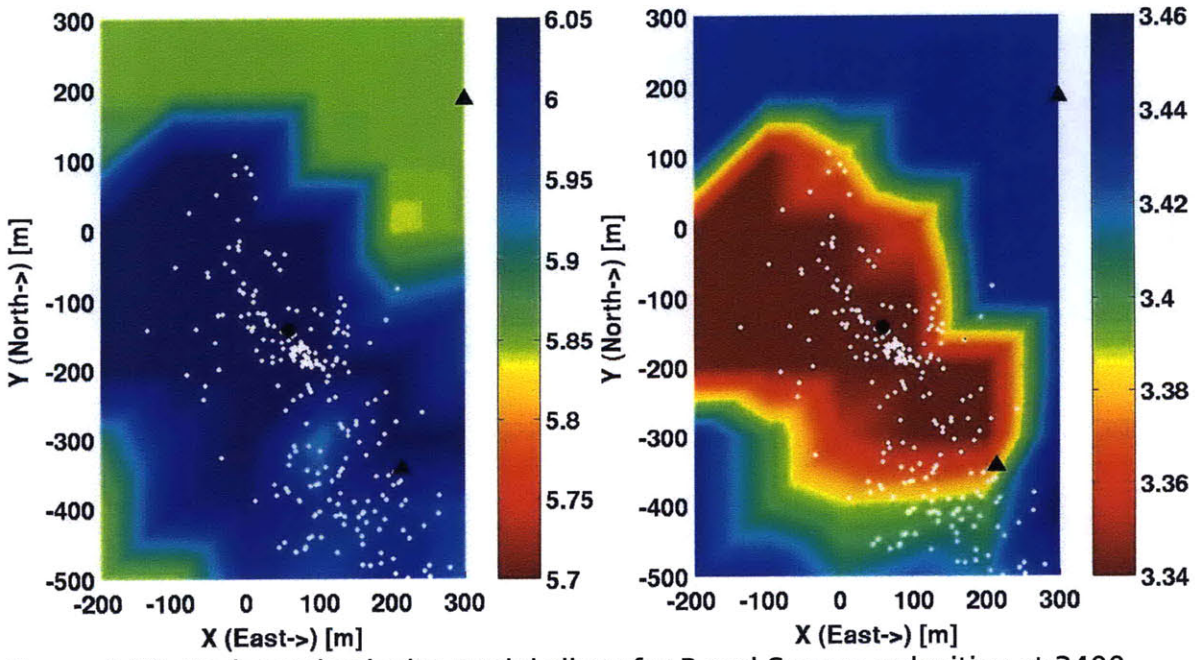

Figure A.10: Horizontal velocity model slices for P and S wave velocities at 3400 meters depth in km/sec. Black circle denotes the position of the injection well GPK1. Black triangles show the locations of station 4550 (upper right) and hyd1 (lower right). White dots denote final earthquake locations within fifty meters depth.

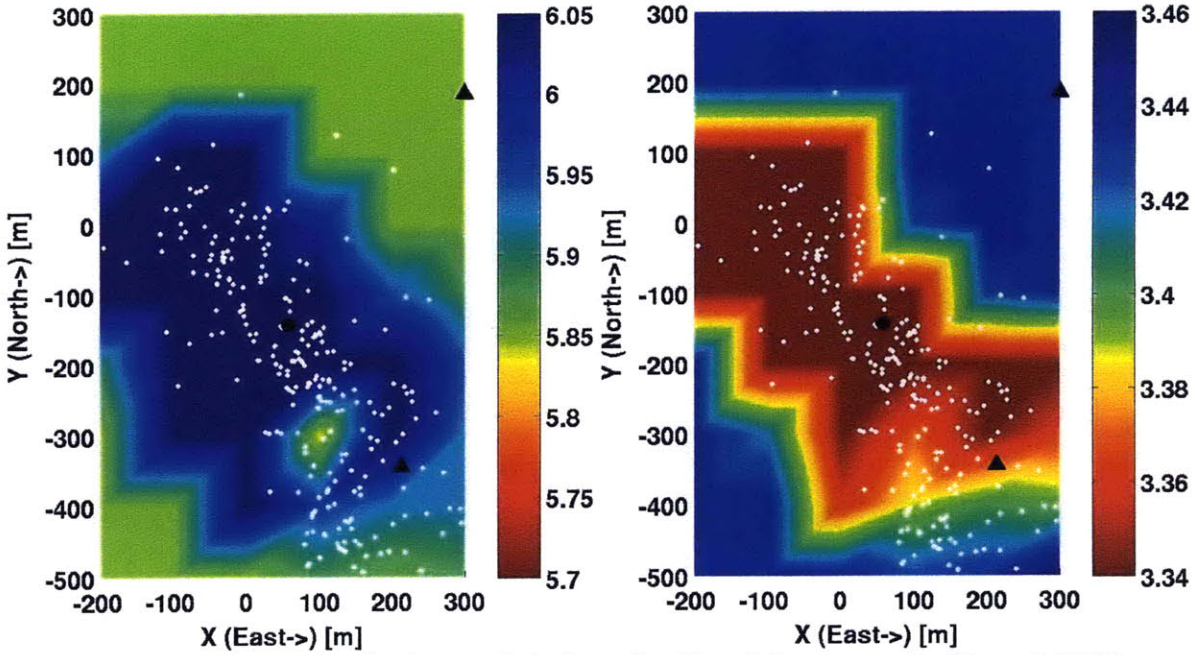

Figure A.11: Horizontal velocity model slices for P and S wave velocities at 3500 meters depth in km/sec. Black circle denotes the position of the injection well GPK1. Black triangles show the locations of station 4550 (upper right) and hyd1 (lower right). White dots denote final earthquake locations within fifty meters depth.

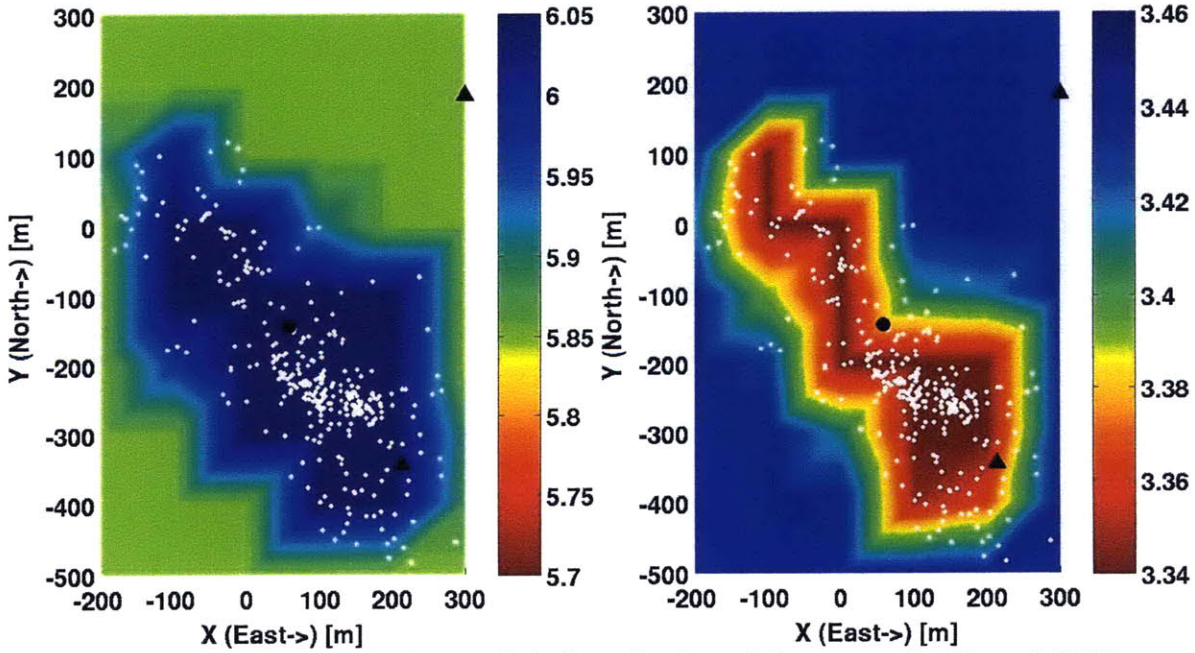

Figure A.12: Horizontal velocity model slices for P and S wave velocities at 3600 meters depth in km/sec. Black circle denotes the position of the injection well GPK1. Black triangles show the locations of station 4550 (upper right) and hyd1 (lower right). White dots denote final earthquake locations within fifty meters depth.

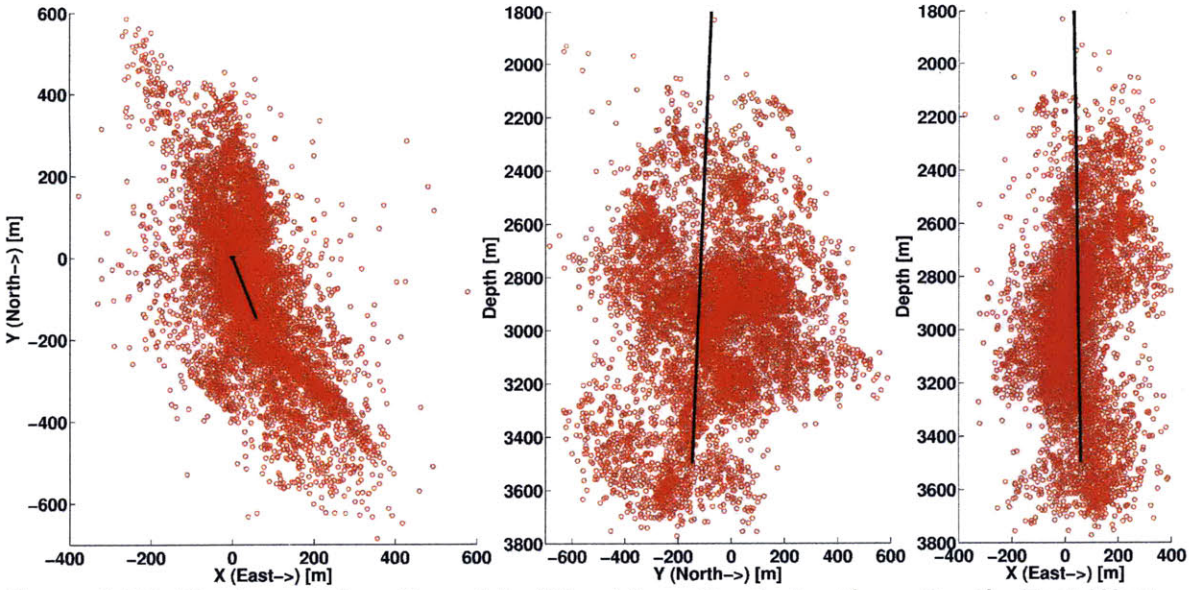

Figure A.13: Final event location plots (Plan View, North-South vs Depth, East-West vs Depth) with the path of GPK1 (black line) into the reservoir.

A.2 Data Results Using JHD Corrections

This set of results was calculated using all the available data (absolute times, differential catalog times, and differential cross-correlation times) and using station corrections, applied to the absolute times, obtained from Rowe *et al.* (2002) who in turn obtained the corrections from a Joint Hypocenter Determination (JHD) inversion. These station corrections are shown in Table A.2. Figures A.14 through A.25 show the tomograms for horizontal depth slices through the three-dimensional velocity model from 2500 to 3600 meters depth in 100 meter intervals for both P and S-waves variations. Figure A.26 shows the final event locations.

Sensor	P-Delay (ms)	S-Delay (ms)
4550	5.49	8.25
4601	16.4	18.9
4616	-0.5	-1.32
hyd1	-1.73	0

Table A.2: Delay times, also known as station corrections, from a JHD inversion (Rowe *et al.* 2002).

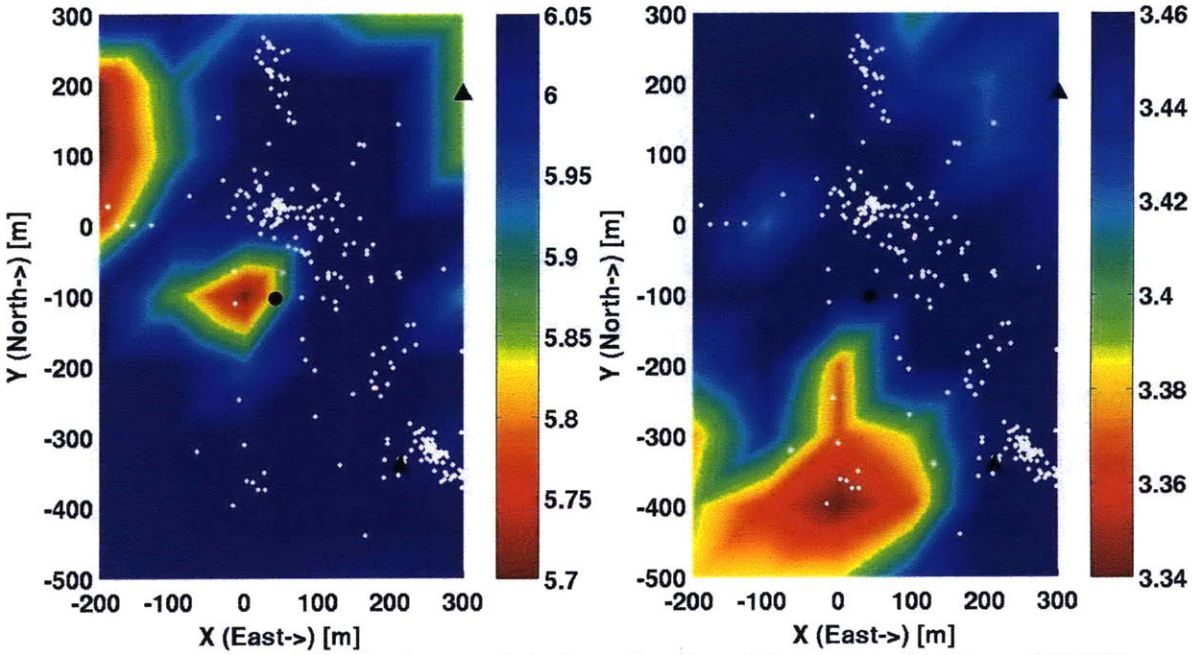

Figure A.14: Horizontal velocity model slices for P and S wave velocities at 2500 meters depth in km/sec. Black circle denotes the position of the injection well GPK1. Black triangles show the locations of station 4550 (upper right) and hyd1 (lower right). White dots denote final earthquake locations within fifty meters depth.

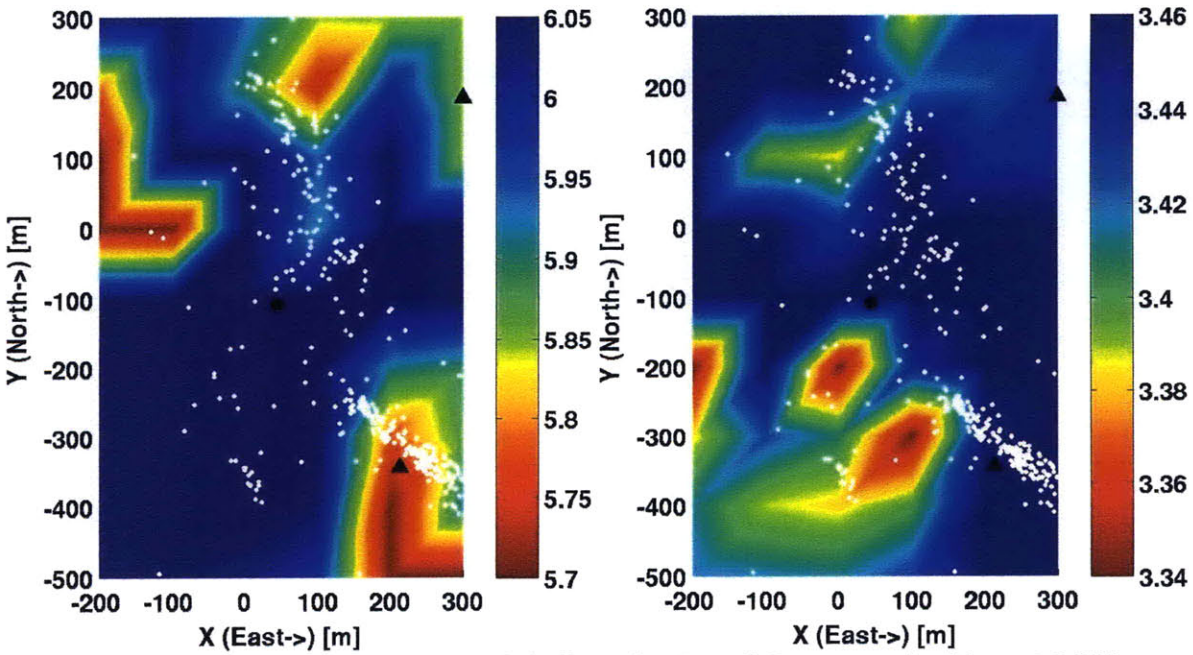

Figure A.15: Horizontal velocity model slices for P and S wave velocities at 2600 meters depth in km/sec. Black circle denotes the position of the injection well GPK1. Black triangles show the locations of station 4550 (upper right) and hyd1 (lower right). White dots denote final earthquake locations within fifty meters depth.

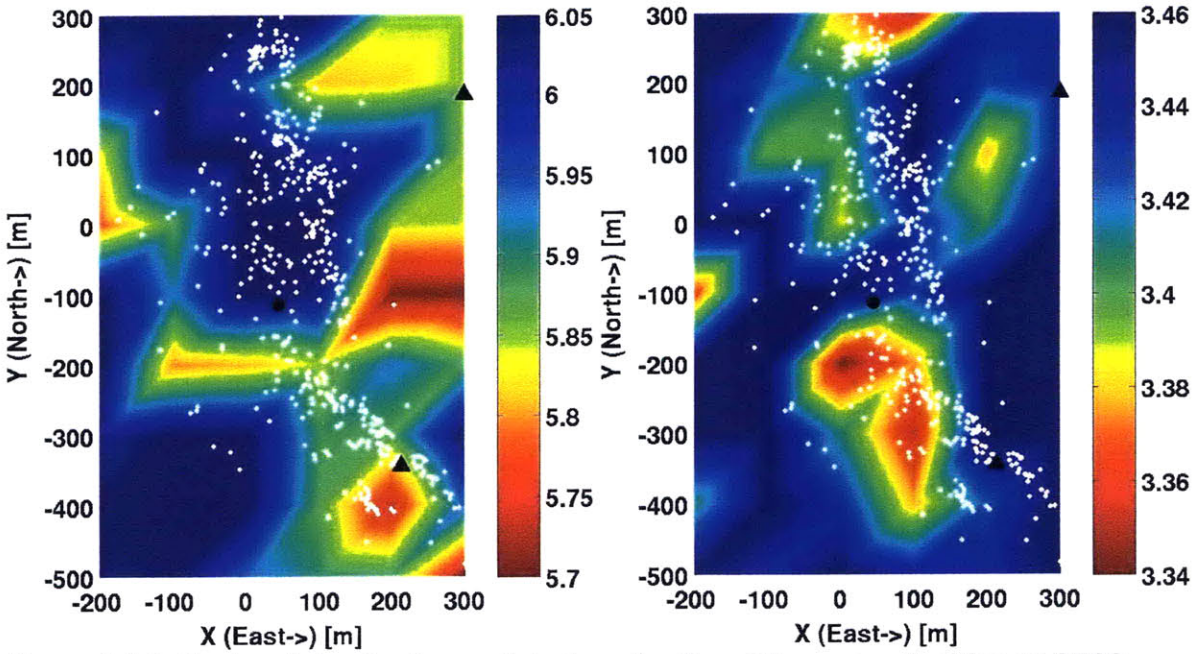

Figure A.16: Horizontal velocity model slices for P and S wave velocities at 2700 meters depth in km/sec. Black circle denotes the position of the injection well GPK1. Black triangles show the locations of station 4550 (upper right) and hyd1 (lower right). White dots denote final earthquake locations within fifty meters depth.

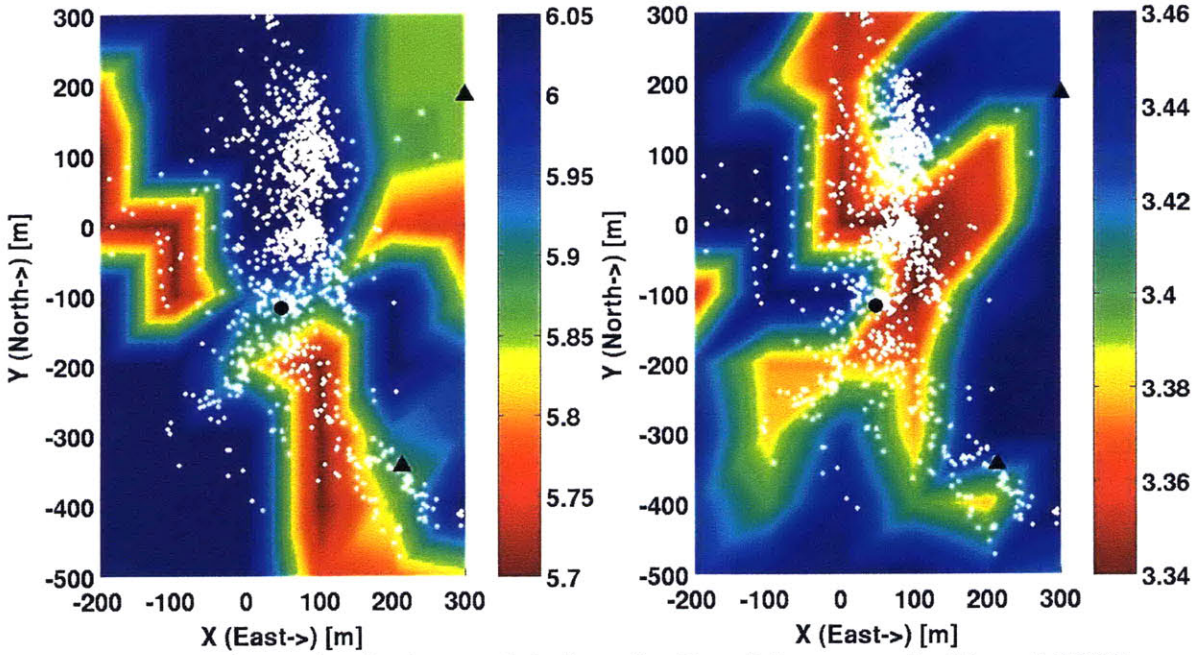

Figure A.17: Horizontal velocity model slices for P and S wave velocities at 2800 meters depth in km/sec. Black circle denotes the position of the injection well GPK1. Black triangles show the locations of station 4550 (upper right) and hyd1 (lower right). White dots denote final earthquake locations within fifty meters depth.

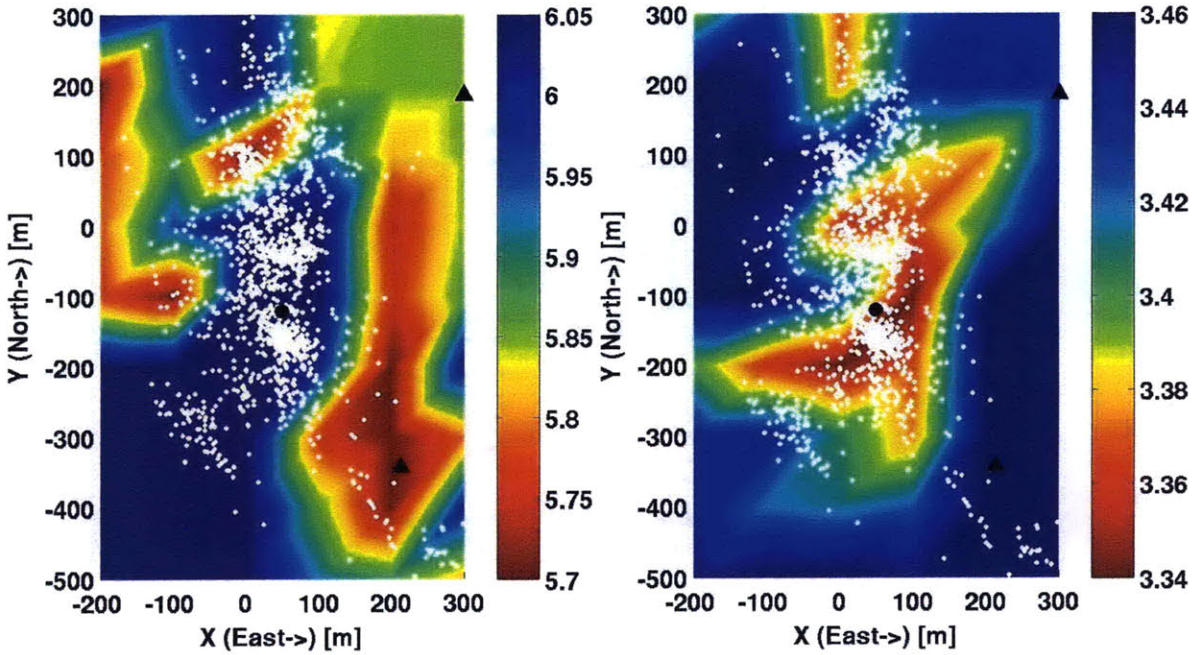

Figure A.18: Horizontal velocity model slices for P and S wave velocities at 2900 meters depth in km/sec. Black circle denotes the position of the injection well GPK1. Black triangles show the locations of station 4550 (upper right) and hyd1 (lower right). White dots denote final earthquake locations within fifty meters depth.

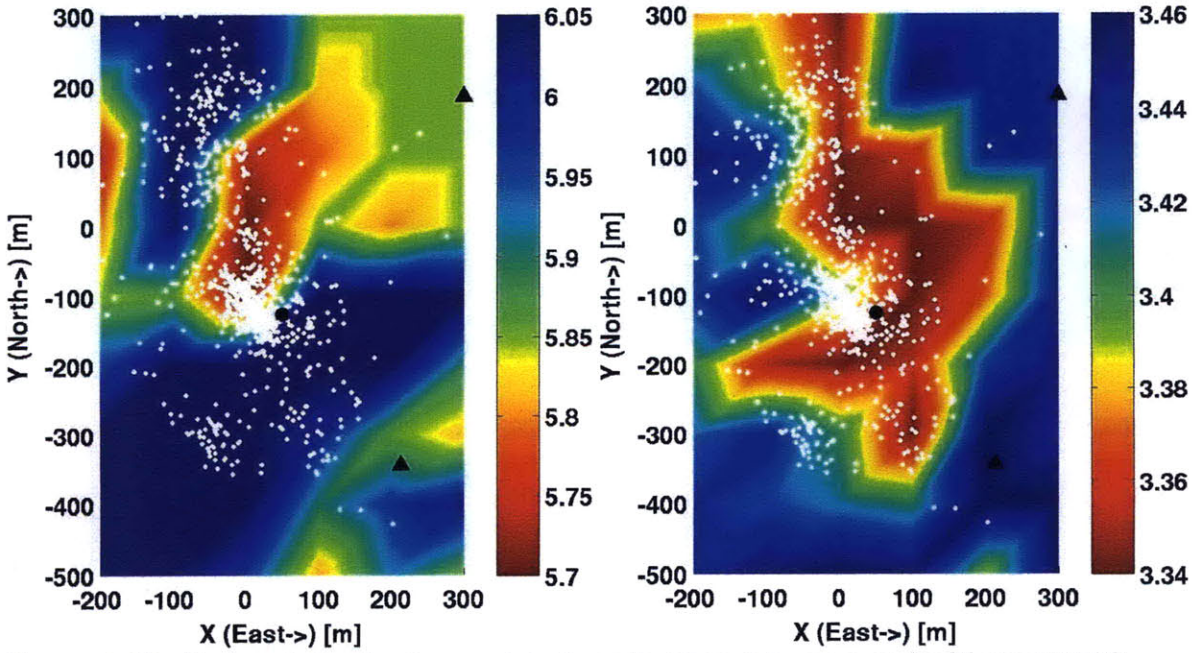

Figure A.19: Horizontal velocity model slices for P and S wave velocities at 3000 meters depth in km/sec. Black circle denotes the position of the injection well GPK1. Black triangles show the locations of station 4550 (upper right) and hyd1 (lower right). White dots denote final earthquake locations within fifty meters depth.

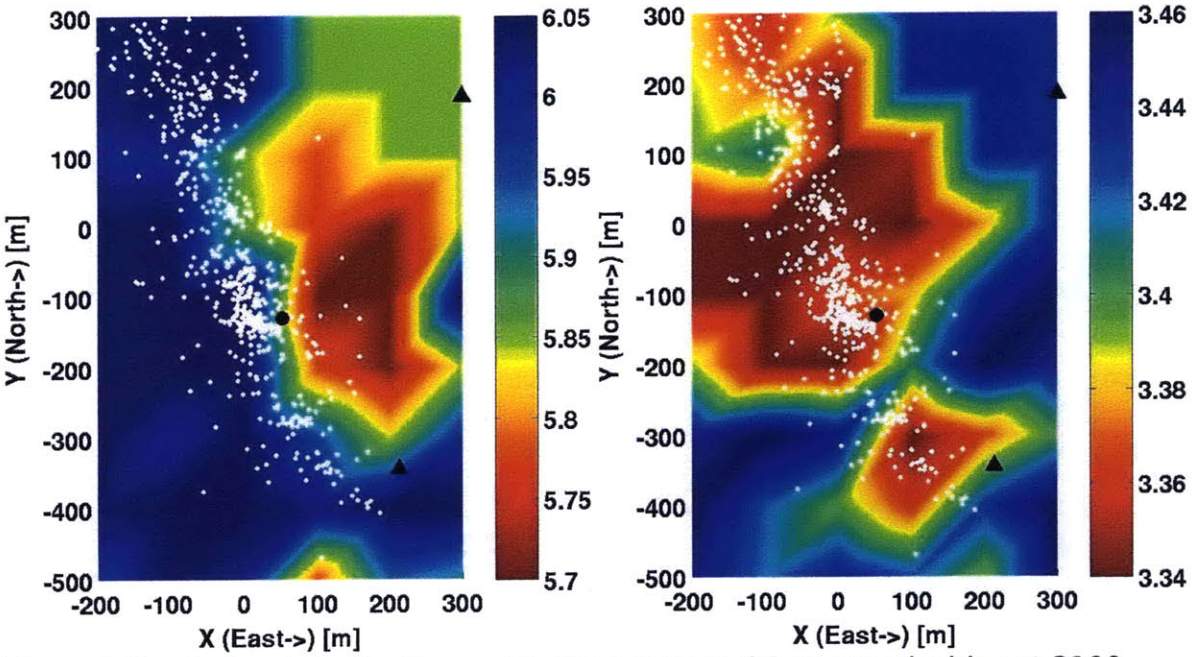

Figure A.20: Horizontal velocity model slices for P and S wave velocities at 3100 meters depth in km/sec. Black circle denotes the position of the injection well GPK1. Black triangles show the locations of station 4550 (upper right) and hyd1 (lower right). White dots denote final earthquake locations within fifty meters depth.

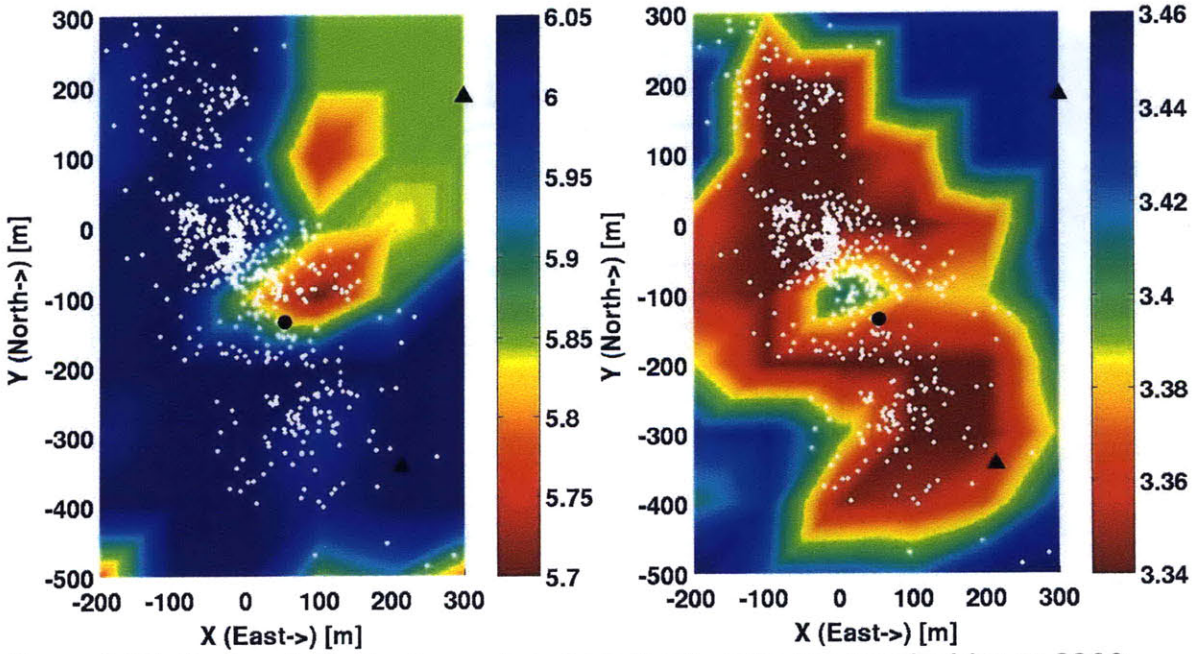

Figure A.21: Horizontal velocity model slices for P and S wave velocities at 3200 meters depth in km/sec. Black circle denotes the position of the injection well GPK1. Black triangles show the locations of station 4550 (upper right) and hyd1 (lower right). White dots denote final earthquake locations within fifty meters depth.

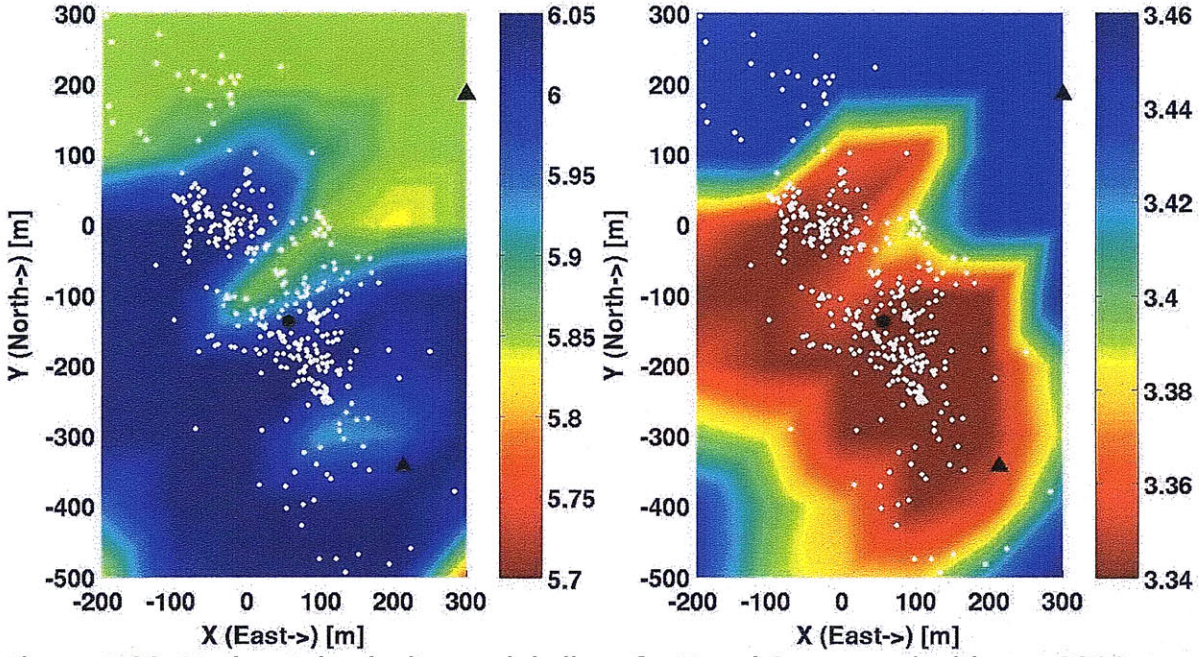

Figure A.22: Horizontal velocity model slices for P and S wave velocities at 3300 meters depth in km/sec. Black circle denotes the position of the injection well GPK1. Black triangles show the locations of station 4550 (upper right) and hyd1 (lower right). White dots denote final earthquake locations within fifty meters depth.

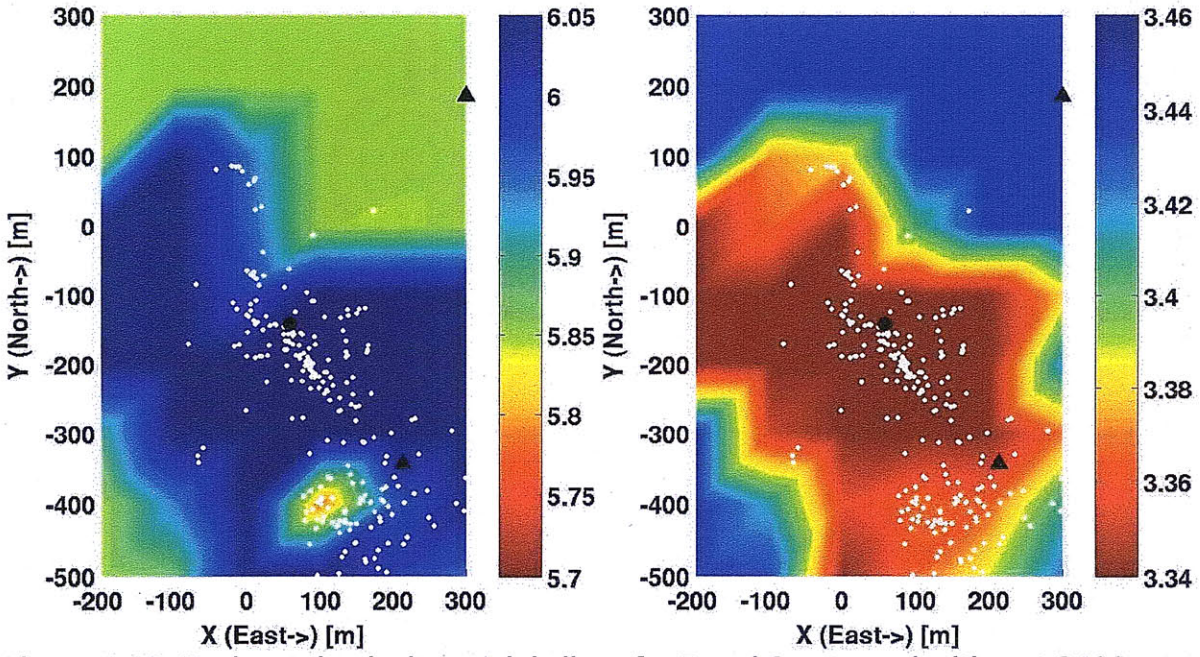

Figure A.23: Horizontal velocity model slices for P and S wave velocities at 3400 meters depth in km/sec. Black circle denotes the position of the injection well GPK1. Black triangles show the locations of station 4550 (upper right) and hyd1 (lower right). White dots denote final earthquake locations within fifty meters depth.

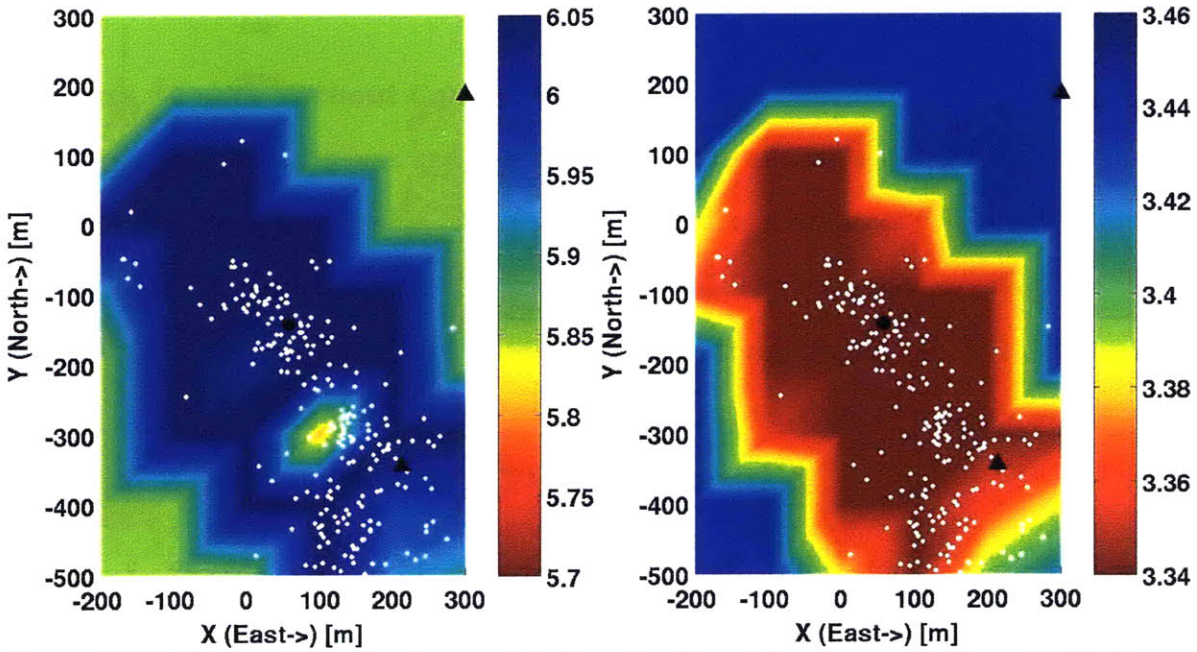

Figure A.24: Horizontal velocity model slices for P and S wave velocities at 3500 meters depth in km/sec. Black circle denotes the position of the injection well GPK1. Black triangles show the locations of station 4550 (upper right) and hyd1 (lower right). White dots denote final earthquake locations within fifty meters depth.

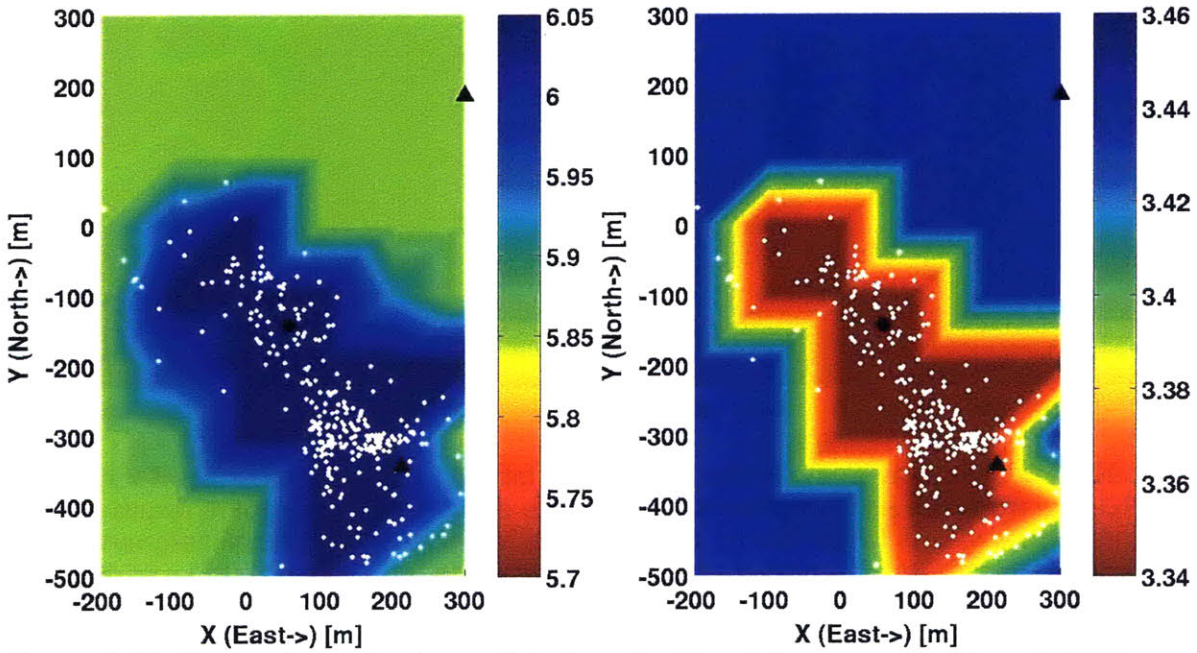

Figure A.25: Horizontal velocity model slices for P and S wave velocities at 3600 meters depth in km/sec. Black circle denotes the position of the injection well GPK1. Black triangles show the locations of station 4550 (upper right) and hyd1 (lower right). White dots denote final earthquake locations within fifty meters depth.

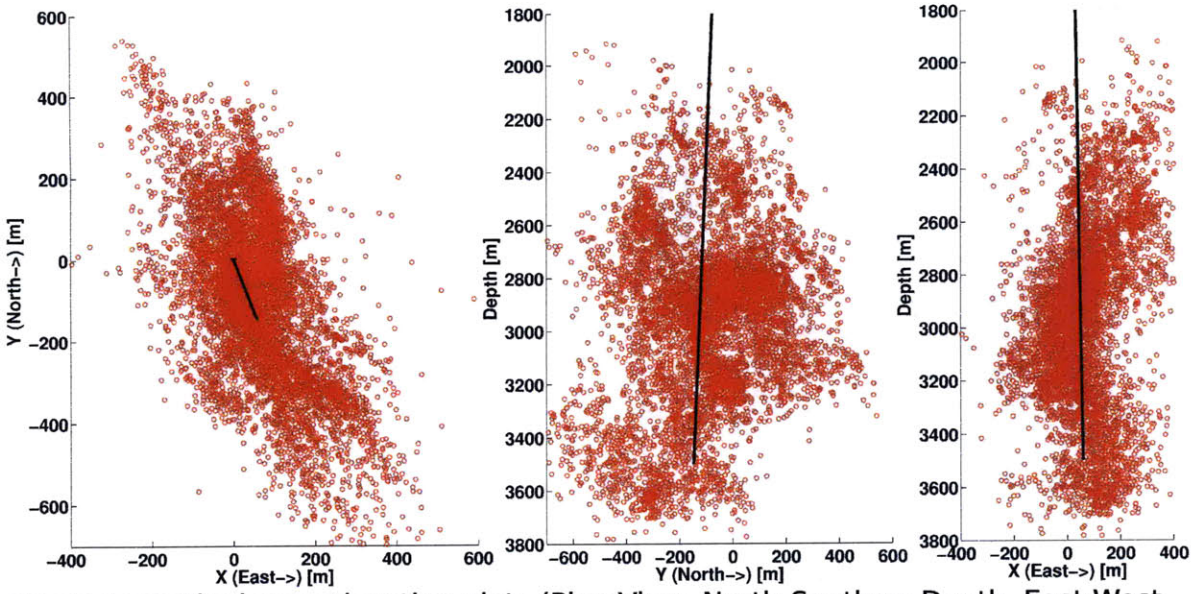

Figure A.26: Final event location plots (Plan View, North-South vs Depth, East-West vs Depth) with the path of GPK1 (black line) into the reservoir.

A.3 Data Results Without Corrections

This set of results was calculated using all the available data (absolute times, differential catalog times, and differential cross-correlation times) without station corrections applied to the absolute times. Figures A.27 through A.38 show the tomograms for horizontal depth slices through the three-dimensional velocity model from 2500 to 3600 meters depth in 100 meter intervals for both P and S-waves variations. Figure A.39 shows the final event locations.

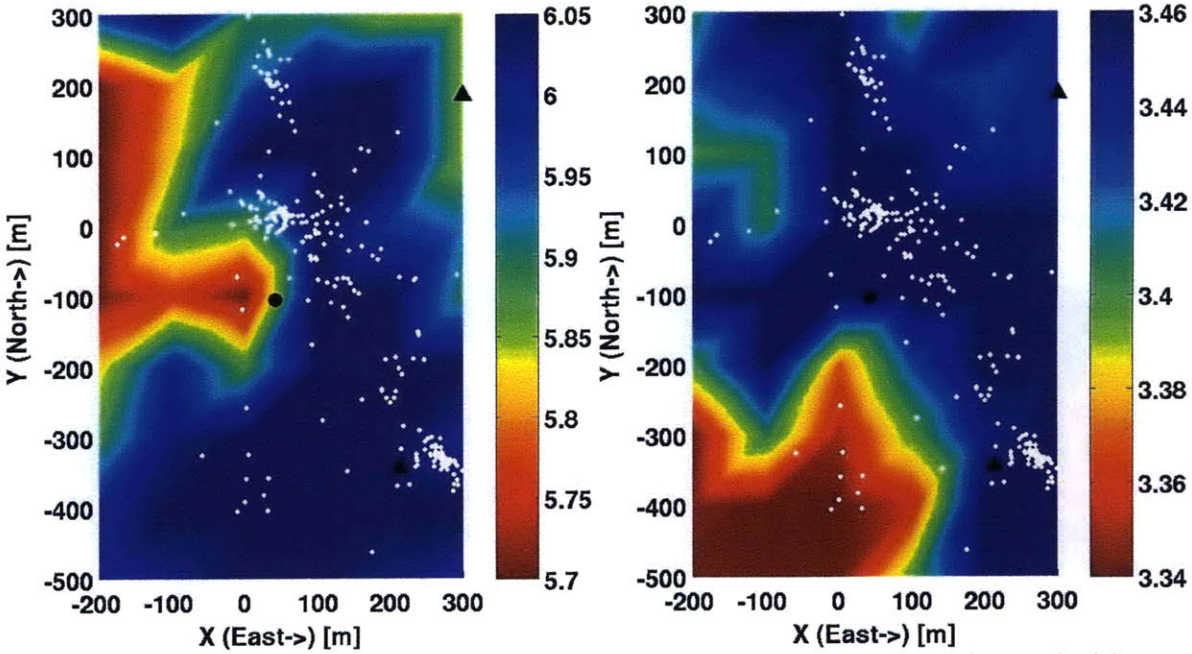

Figure A.27: Horizontal velocity model slices for P and S wave velocities at 2500 meters depth in km/sec. Black circle denotes the position of the injection well GPK1. Black triangles show the locations of station 4550 (upper right) and hyd1 (lower right). White dots denote final earthquake locations within fifty meters depth.

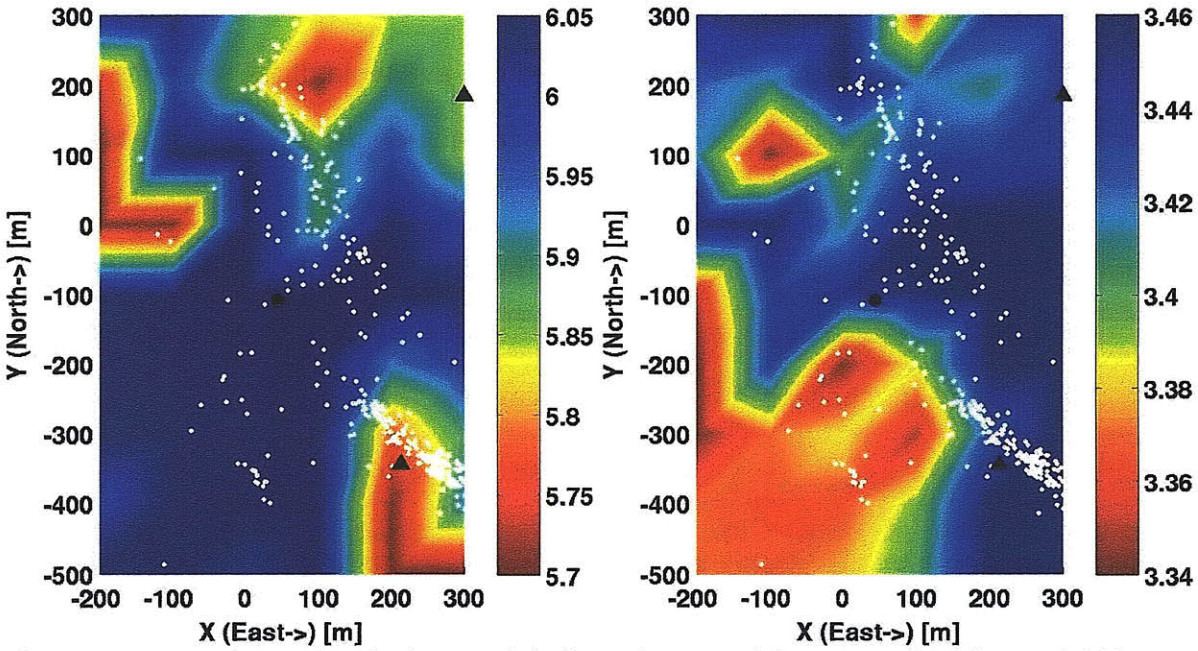

Figure A.28: Horizontal velocity model slices for P and S wave velocities at 2600 meters depth in km/sec. Black circle denotes the position of the injection well GPK1. Black triangles show the locations of station 4550 (upper right) and hyd1 (lower right). White dots denote final earthquake locations within fifty meters depth.

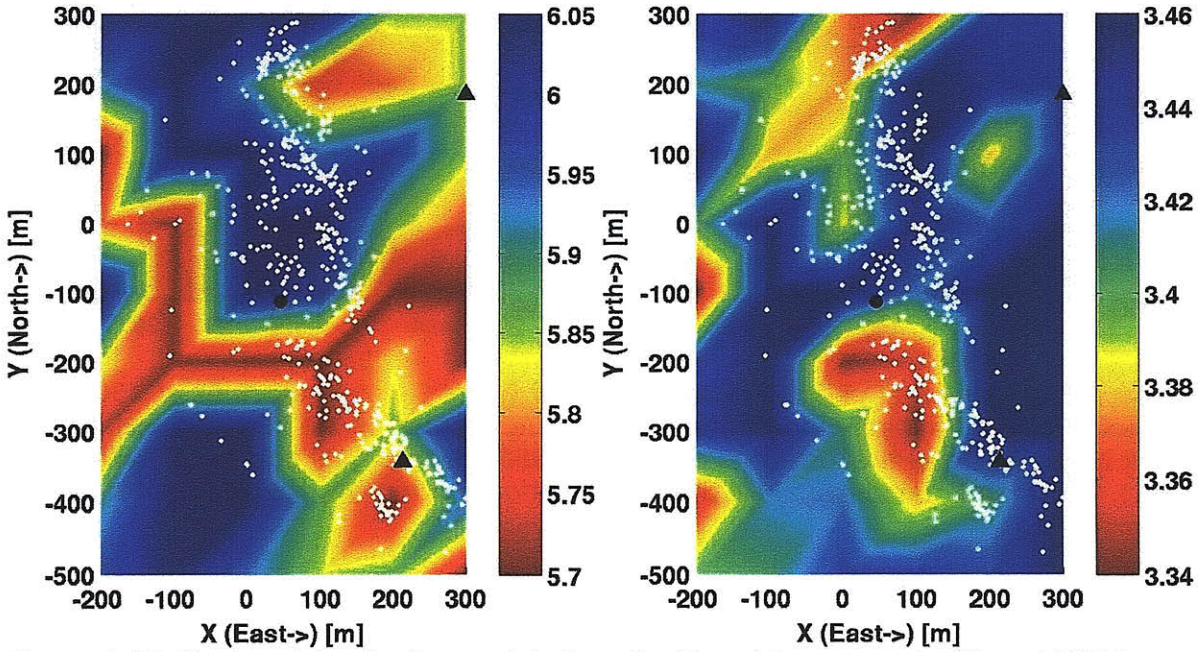

Figure A.29: Horizontal velocity model slices for P and S wave velocities at 2700 meters depth in km/sec. Black circle denotes the position of the injection well GPK1. Black triangles show the locations of station 4550 (upper right) and hyd1 (lower right). White dots denote final earthquake locations within fifty meters depth.

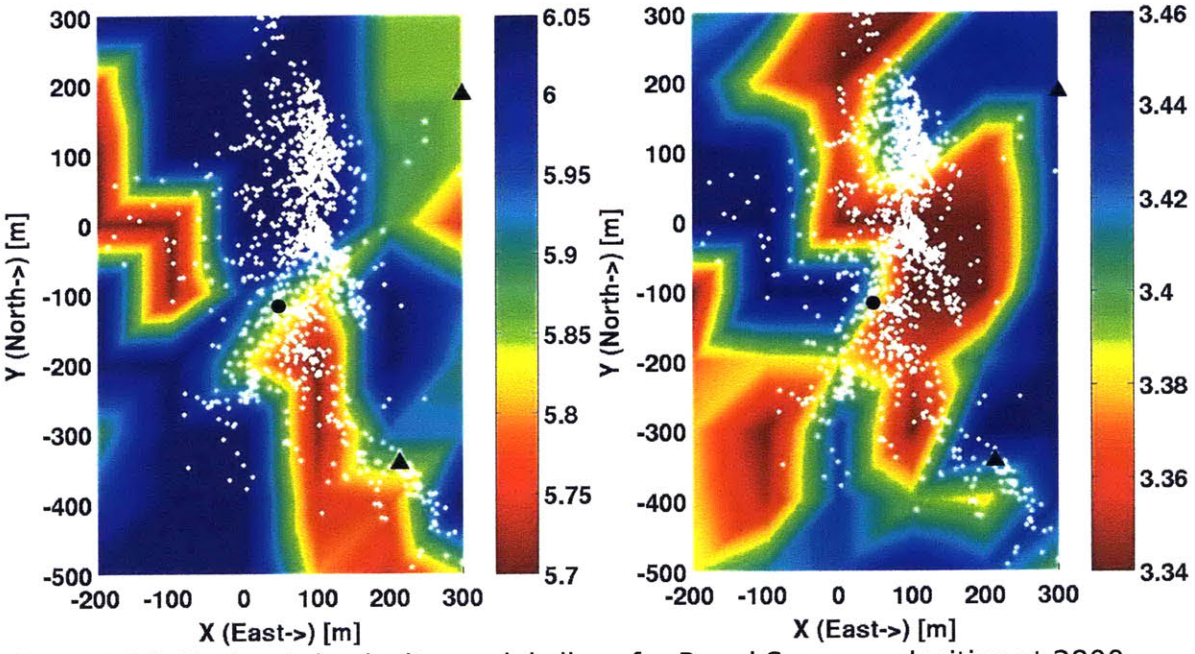

Figure A.30: Horizontal velocity model slices for P and S wave velocities at 2800 meters depth in km/sec. Black circle denotes the position of the injection well GPK1. Black triangles show the locations of station 4550 (upper right) and hyd1 (lower right). White dots denote final earthquake locations within fifty meters depth.

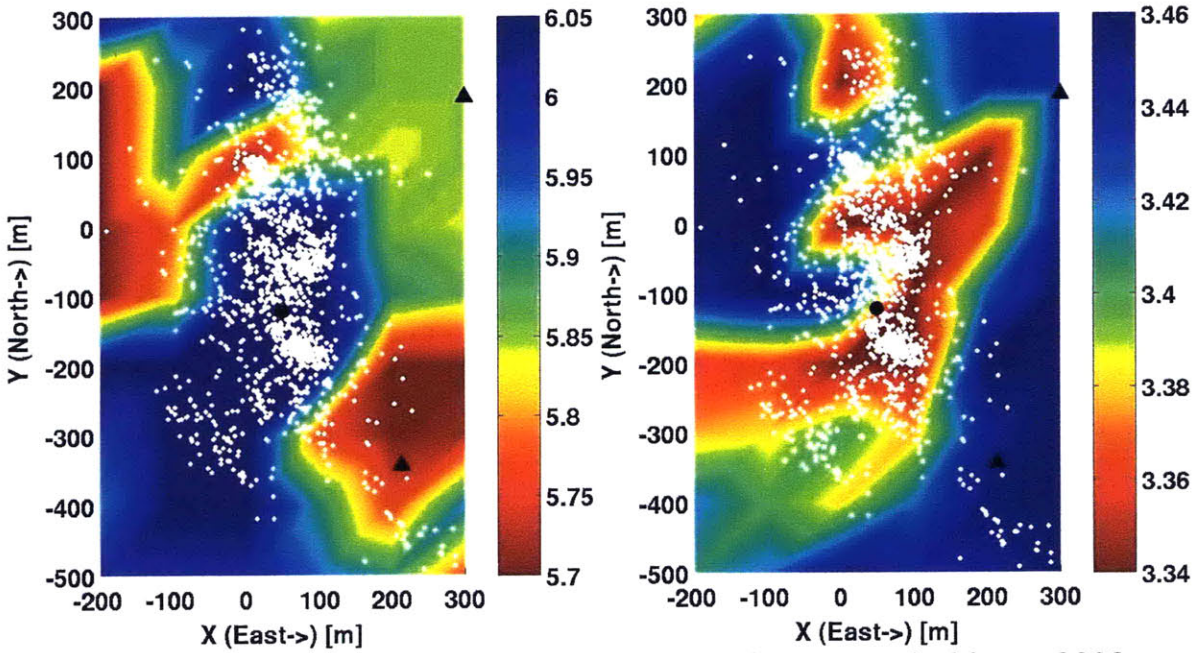

Figure A.31: Horizontal velocity model slices for P and S wave velocities at 2900 meters depth in km/sec. Black circle denotes the position of the injection well GPK1. Black triangles show the locations of station 4550 (upper right) and hyd1 (lower right). White dots denote final earthquake locations within fifty meters depth.

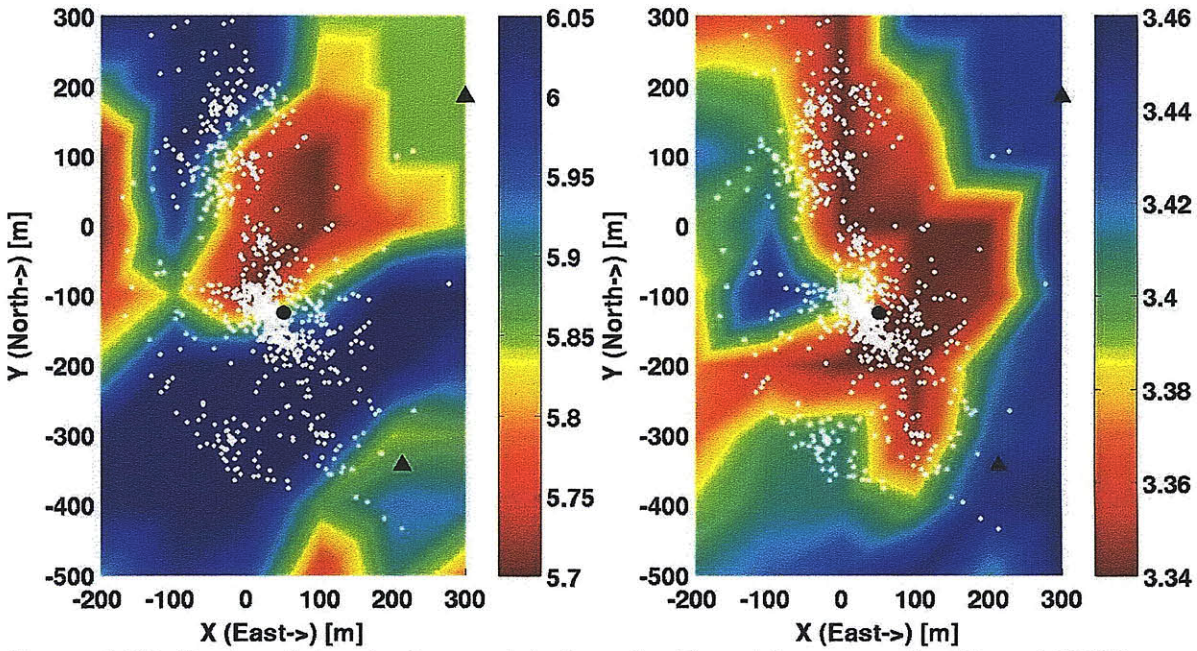

Figure A.32: Horizontal velocity model slices for P and S wave velocities at 3000 meters depth in km/sec. Black circle denotes the position of the injection well GPK1. Black triangles show the locations of station 4550 (upper right) and hyd1 (lower right). White dots denote final earthquake locations within fifty meters depth.

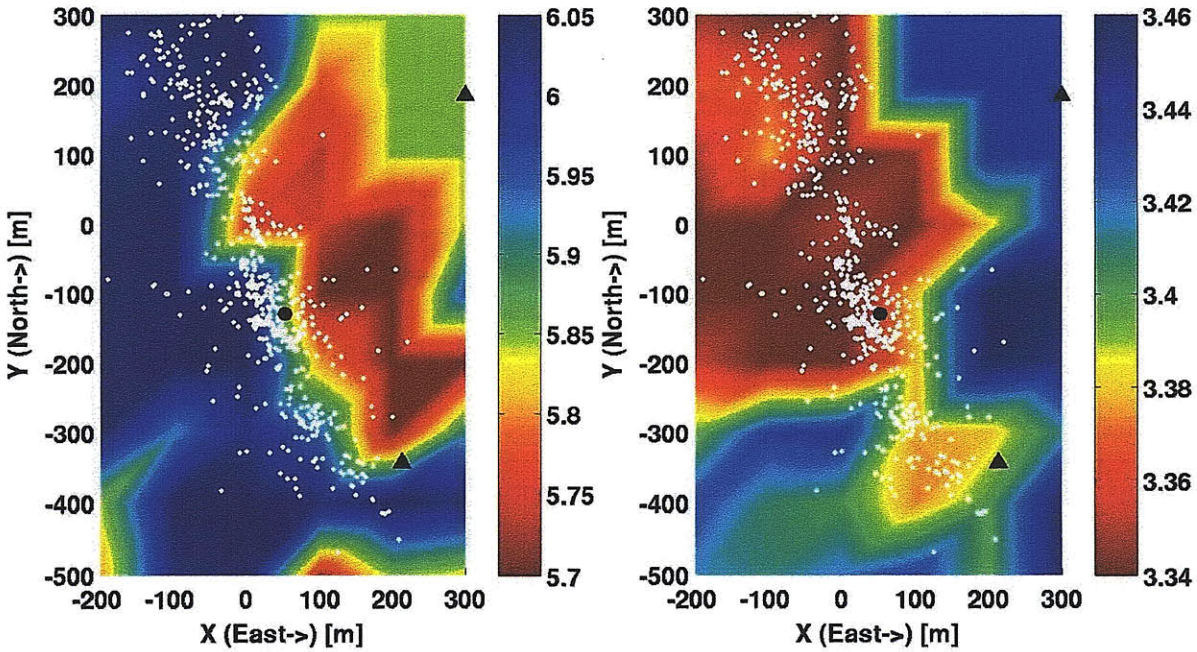

Figure A.33: Horizontal velocity model slices for P and S wave velocities at 3100 meters depth in km/sec. Black circle denotes the position of the injection well GPK1. Black triangles show the locations of station 4550 (upper right) and hyd1 (lower right). White dots denote final earthquake locations within fifty meters depth.

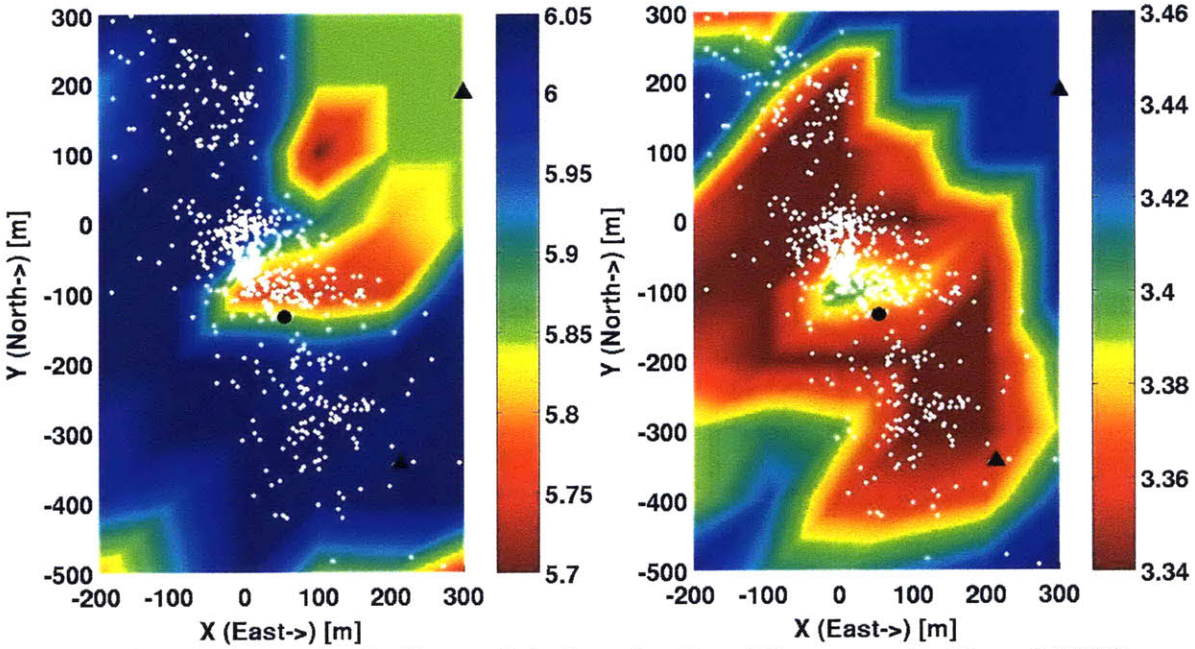

Figure A.34: Horizontal velocity model slices for P and S wave velocities at 3200 meters depth in km/sec. Black circle denotes the position of the injection well GPK1. Black triangles show the locations of station 4550 (upper right) and hyd1 (lower right). White dots denote final earthquake locations within fifty meters depth.

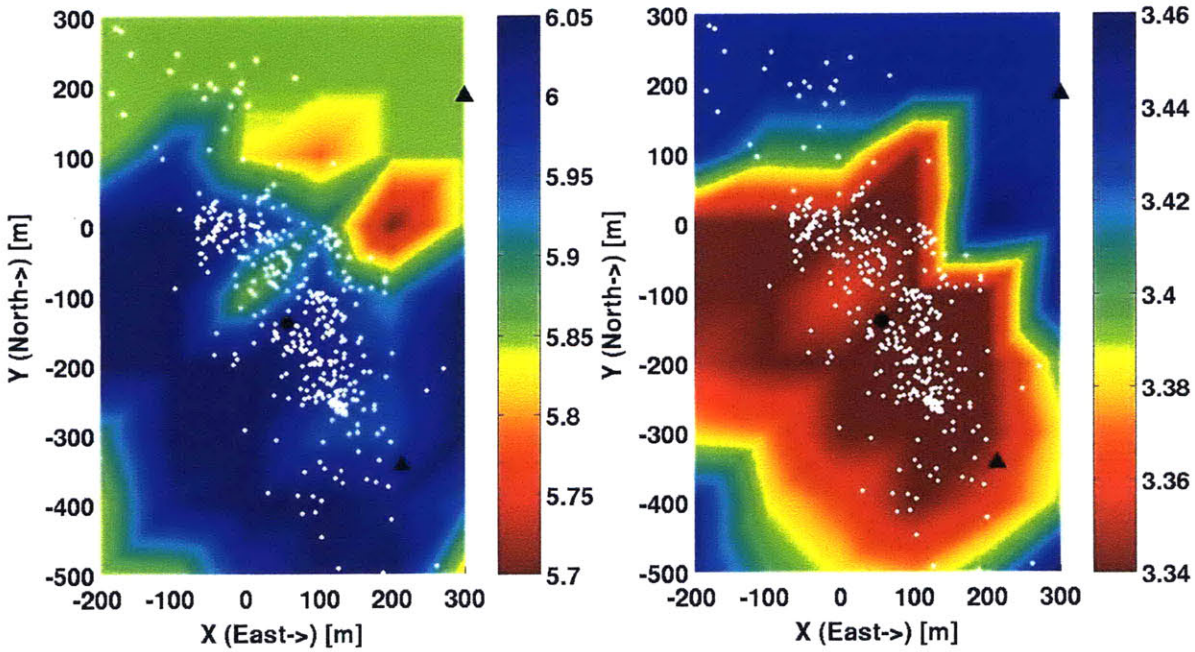

Figure A.35: Horizontal velocity model slices for P and S wave velocities at 3300 meters depth in km/sec. Black circle denotes the position of the injection well GPK1. Black triangles show the locations of station 4550 (upper right) and hyd1 (lower right). White dots denote final earthquake locations within fifty meters depth.

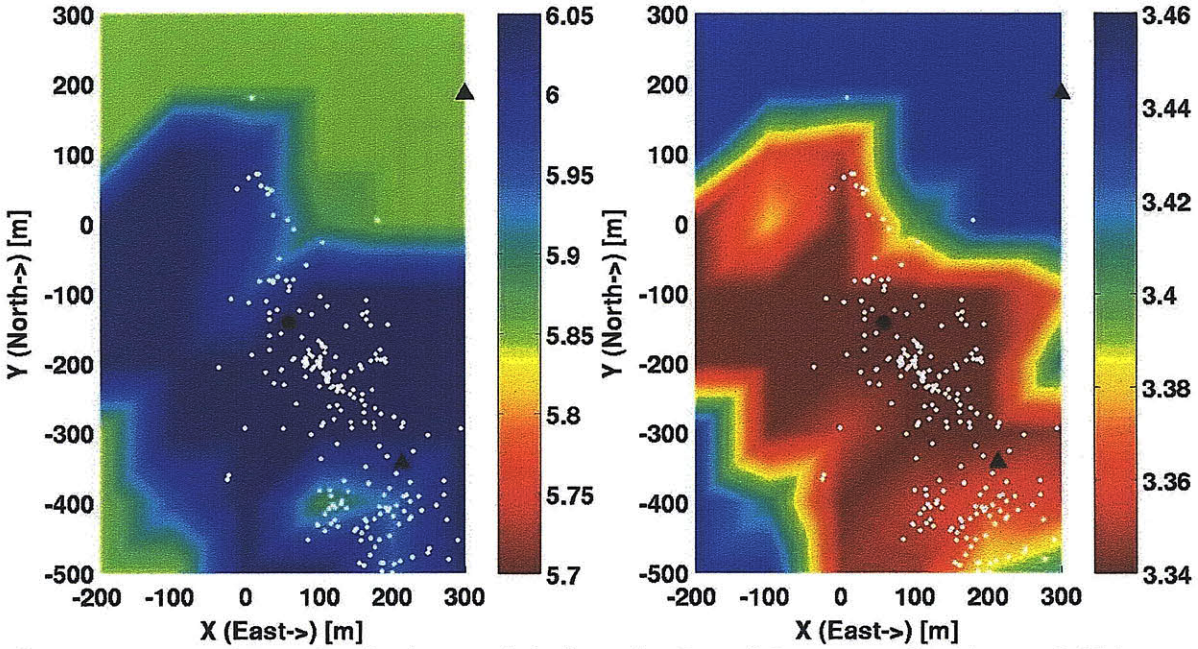

Figure A.36: Horizontal velocity model slices for P and S wave velocities at 3400 meters depth in km/sec. Black circle denotes the position of the injection well GPK1. Black triangles show the locations of station 4550 (upper right) and hyd1 (lower right). White dots denote final earthquake locations within fifty meters depth.

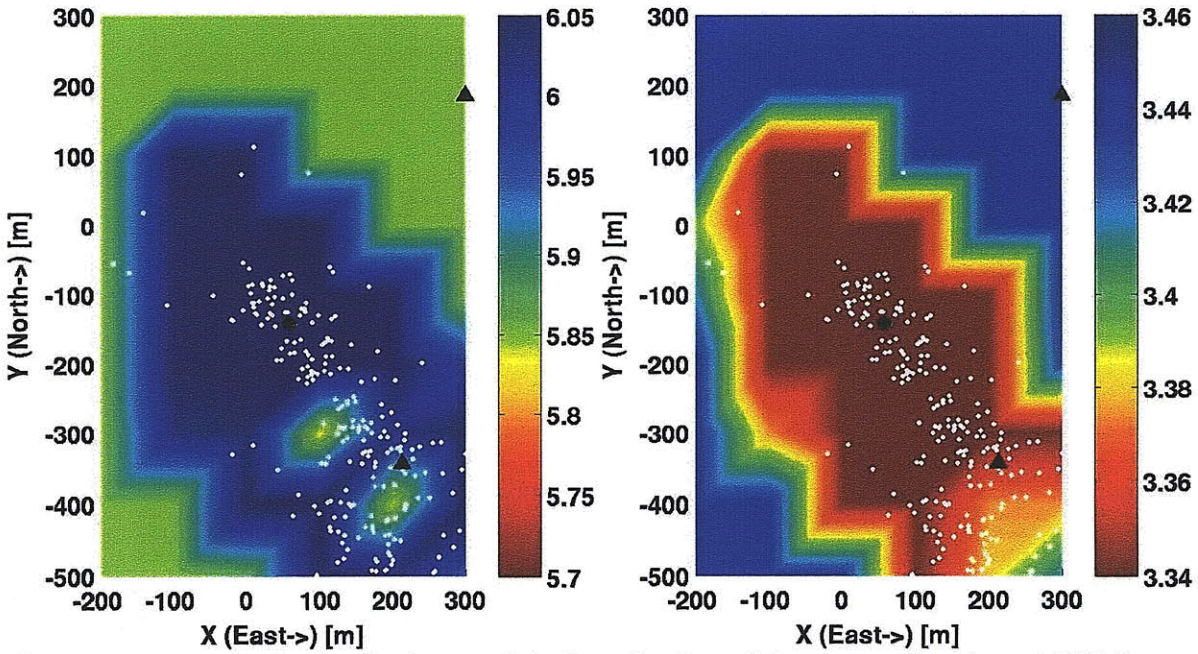

Figure A.37: Horizontal velocity model slices for P and S wave velocities at 3500 meters depth in km/sec. Black circle denotes the position of the injection well GPK1. Black triangles show the locations of station 4550 (upper right) and hyd1 (lower right). White dots denote final earthquake locations within fifty meters depth.

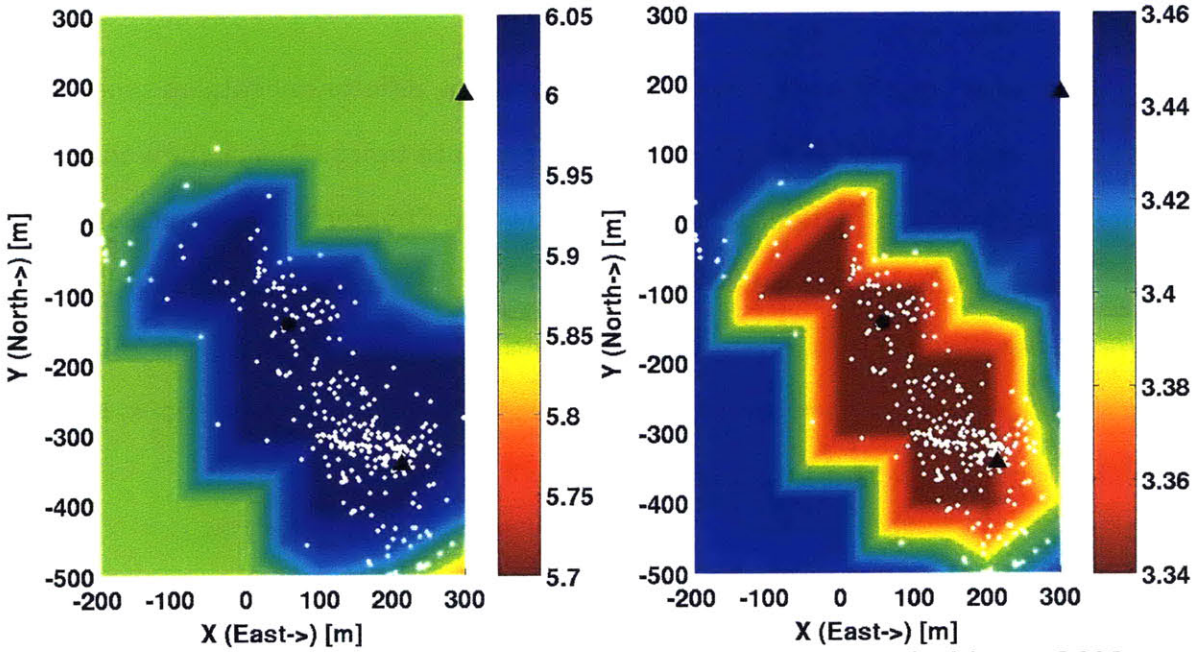

Figure A.38: Horizontal velocity model slices for P and S wave velocities at 3600 meters depth in km/sec. Black circle denotes the position of the injection well GPK1. Black triangles show the locations of station 4550 (upper right) and hyd1 (lower right). White dots denote final earthquake locations within fifty meters depth.

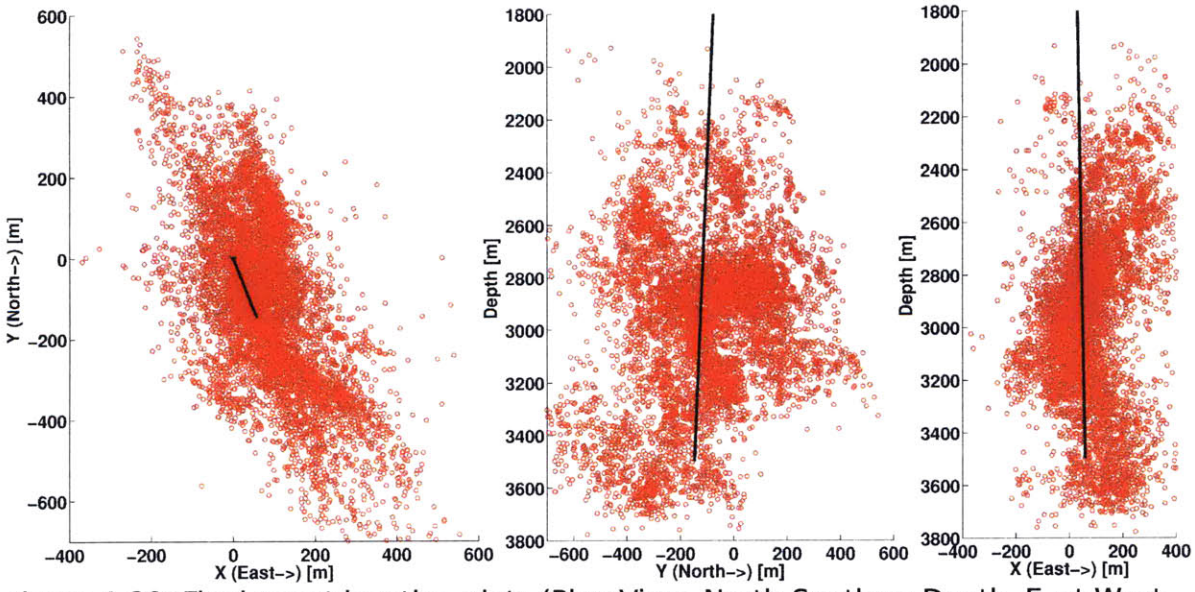

Figure A.39: Final event location plots (Plan View, North-South vs Depth, East-West vs Depth) with the path of GPK1 (black line) into the reservoir.

A.4 Differential Only Data Results

This set of results was calculated using only the differential catalog times and differential cross-correlation times without the absolute times. This circumvented the need for station corrections which were shown, in Chapter 2, to produce shifts in the final event locations. Figures A.40 through A.51 show the tomograms for horizontal depth slices through the three-dimensional velocity model from 2500 to 3600 meters depth in 100 meter intervals for both P and S-waves variations. Figure A.52 shows the final event locations.

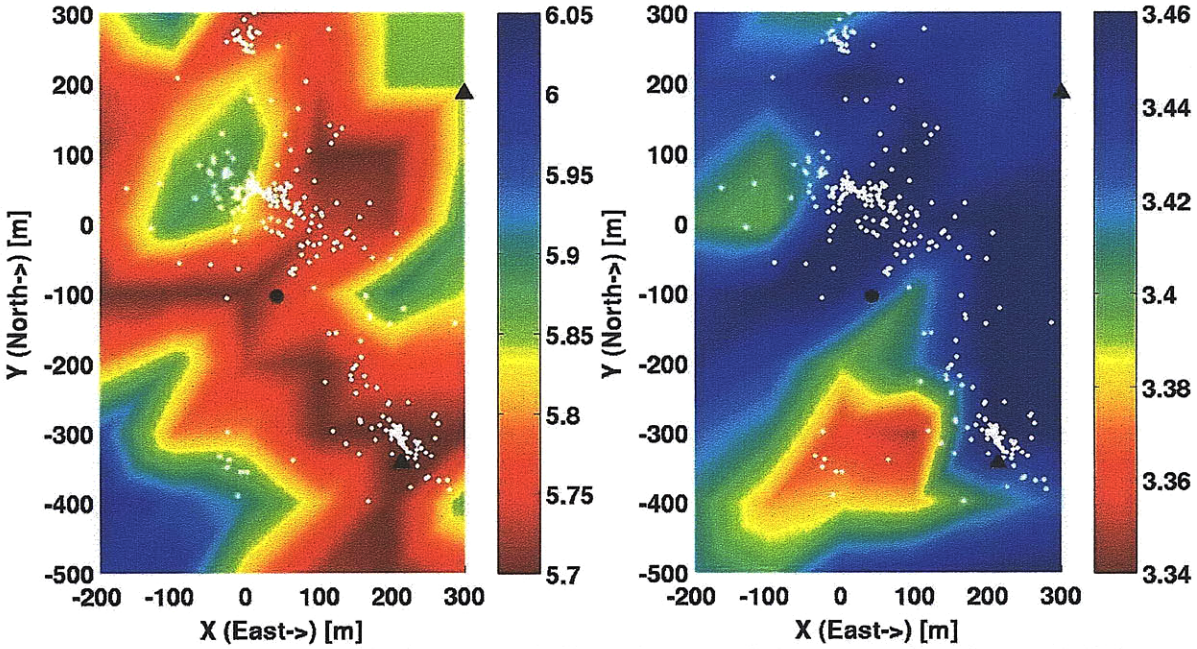

Figure A.40: Horizontal velocity model slices for P and S wave velocities at 2500 meters depth in km/sec. Black circle denotes the position of the injection well GPK1. Black triangles show the locations of station 4550 (upper right) and hyd1 (lower right). White dots denote final earthquake locations within fifty meters depth.

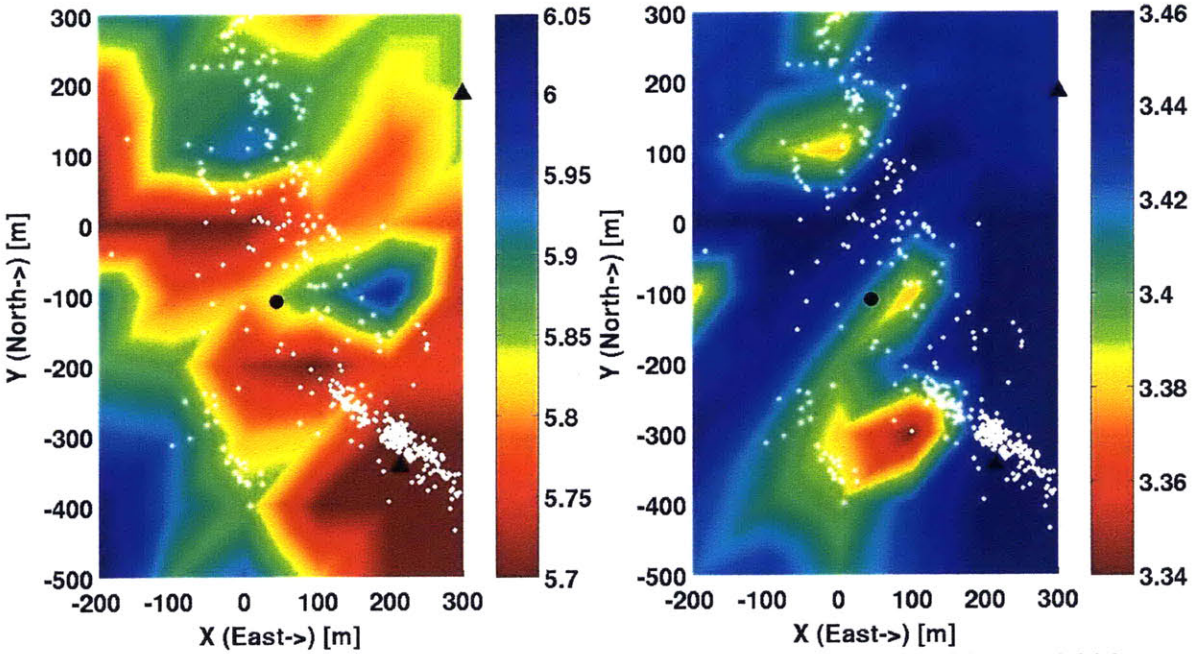

Figure A.41: Horizontal velocity model slices for P and S wave velocities at 2600 meters depth in km/sec. Black circle denotes the position of the injection well GPK1. Black triangles show the locations of station 4550 (upper right) and hyd1 (lower right). White dots denote final earthquake locations within fifty meters depth.

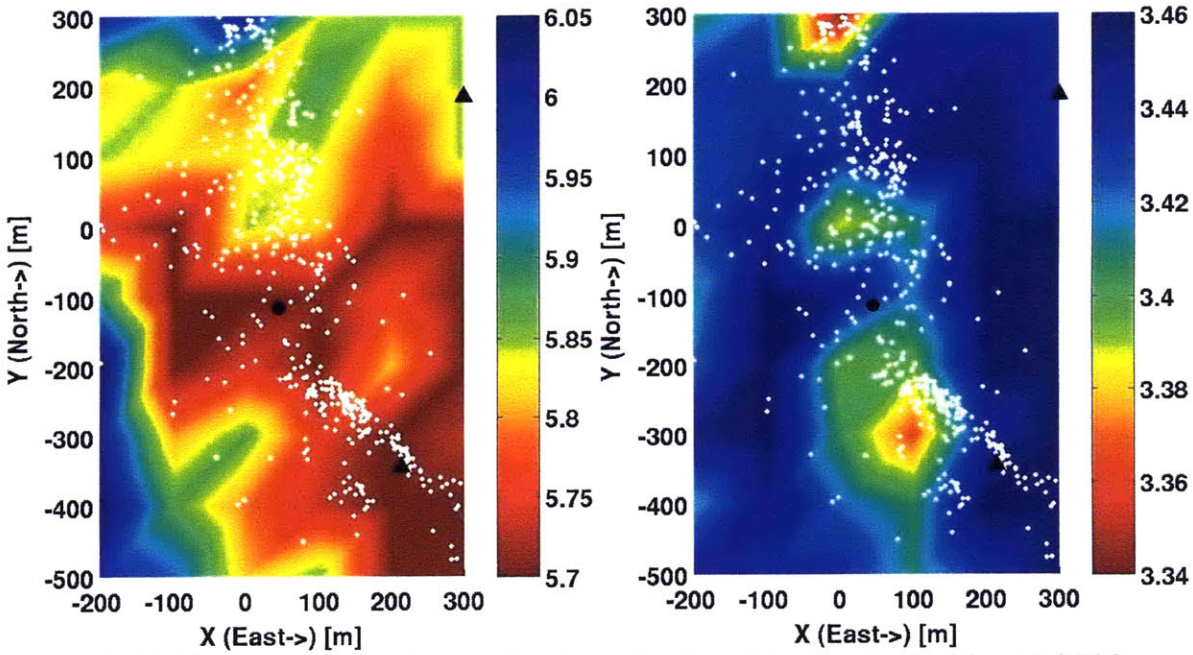

Figure A.42: Horizontal velocity model slices for P and S wave velocities at 2700 meters depth in km/sec. Black circle denotes the position of the injection well GPK1. Black triangles show the locations of station 4550 (upper right) and hyd1 (lower right). White dots denote final earthquake locations within fifty meters depth.

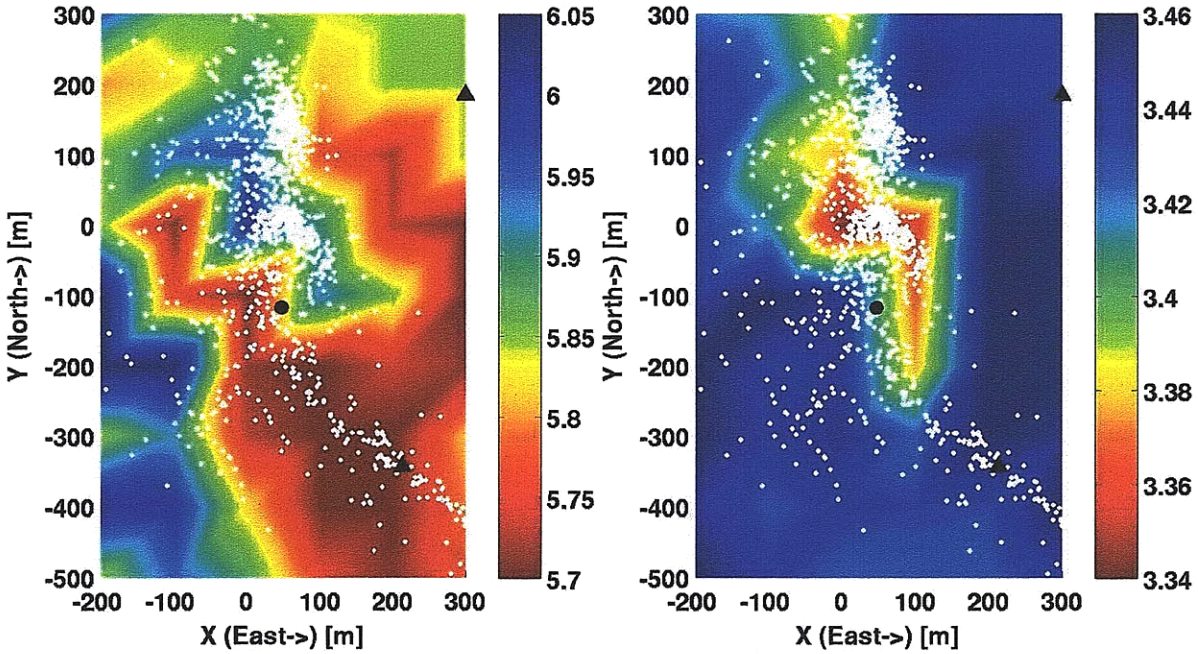

Figure A.43: Horizontal velocity model slices for P and S wave velocities at 2800 meters depth in km/sec. Black circle denotes the position of the injection well GPK1. Black triangles show the locations of station 4550 (upper right) and hyd1 (lower right). White dots denote final earthquake locations within fifty meters depth.

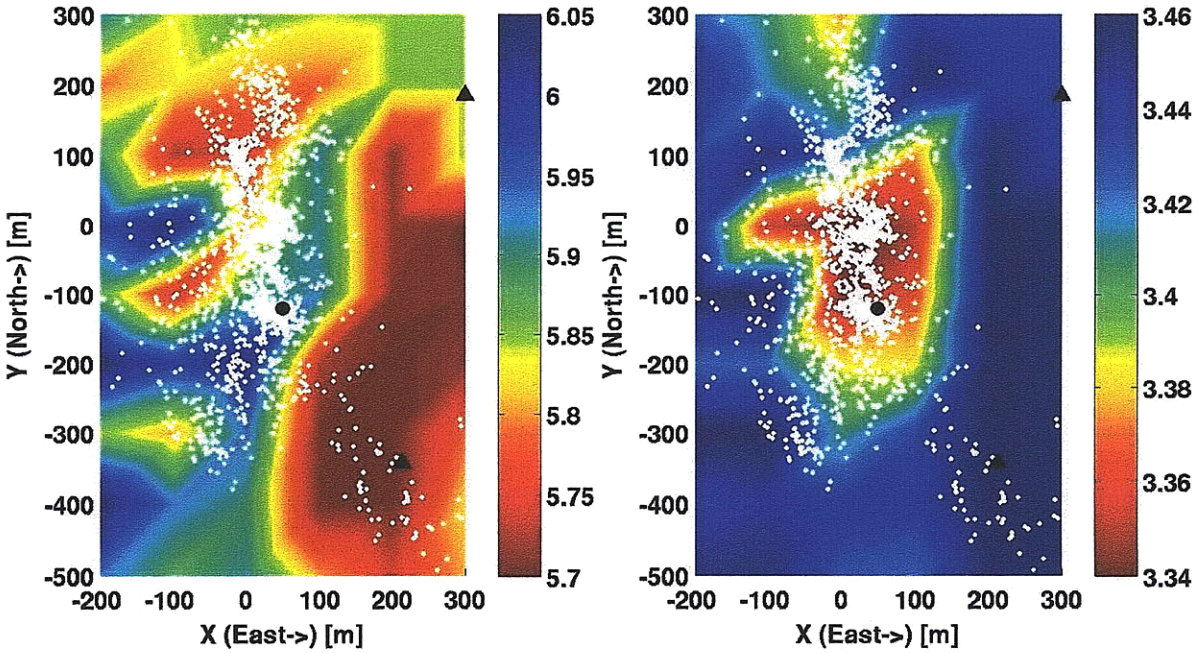

Figure A.44: Horizontal velocity model slices for P and S wave velocities at 2900 meters depth in km/sec. Black circle denotes the position of the injection well GPK1. Black triangles show the locations of station 4550 (upper right) and hyd1 (lower right). White dots denote final earthquake locations within fifty meters depth.

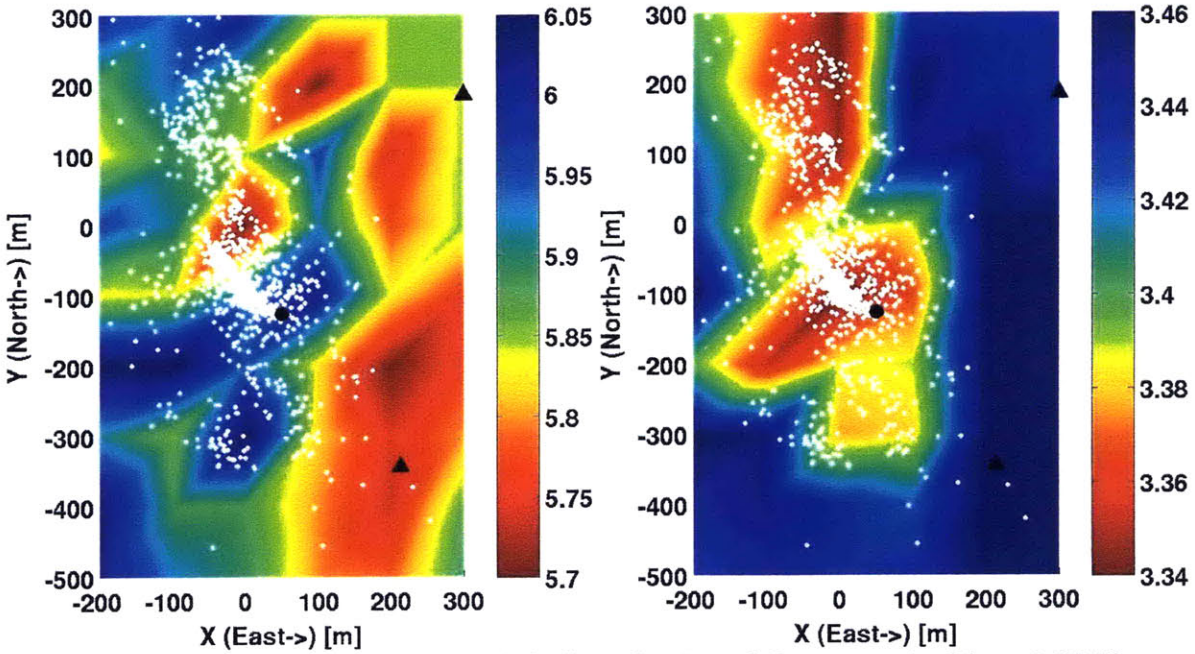

Figure A.45: Horizontal velocity model slices for P and S wave velocities at 3000 meters depth in km/sec. Black circle denotes the position of the injection well GPK1. Black triangles show the locations of station 4550 (upper right) and hyd1 (lower right). White dots denote final earthquake locations within fifty meters depth.

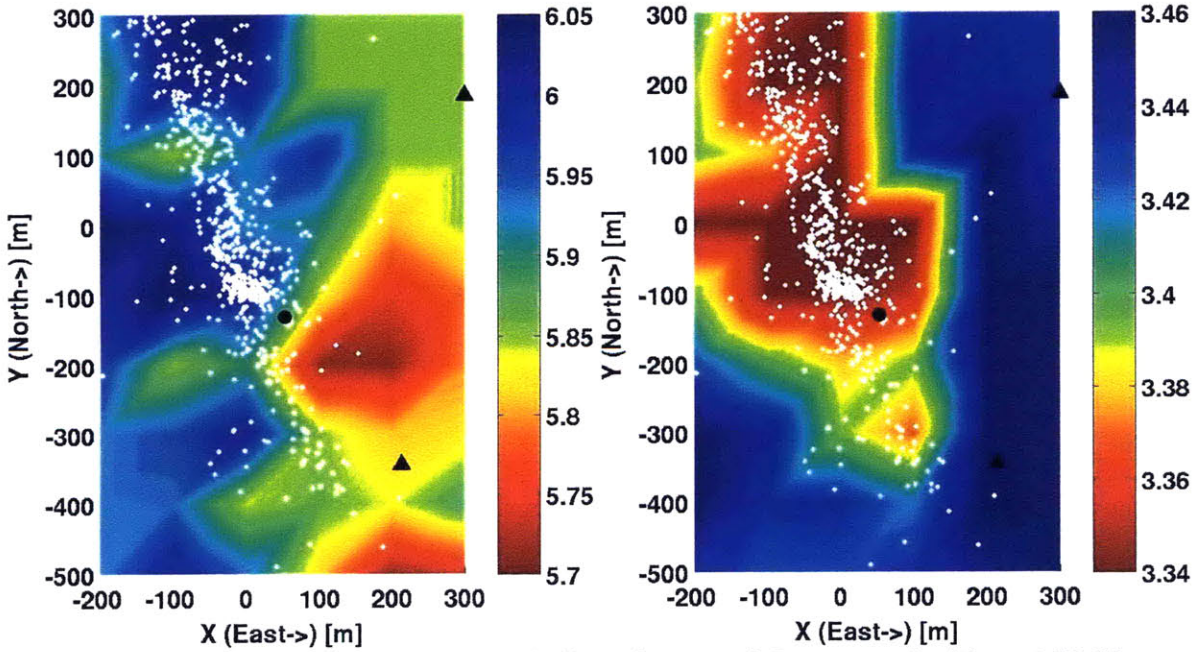

Figure A.46: Horizontal velocity model slices for P and S wave velocities at 3100 meters depth in km/sec. Black circle denotes the position of the injection well GPK1. Black triangles show the locations of station 4550 (upper right) and hyd1 (lower right). White dots denote final earthquake locations within fifty meters depth.

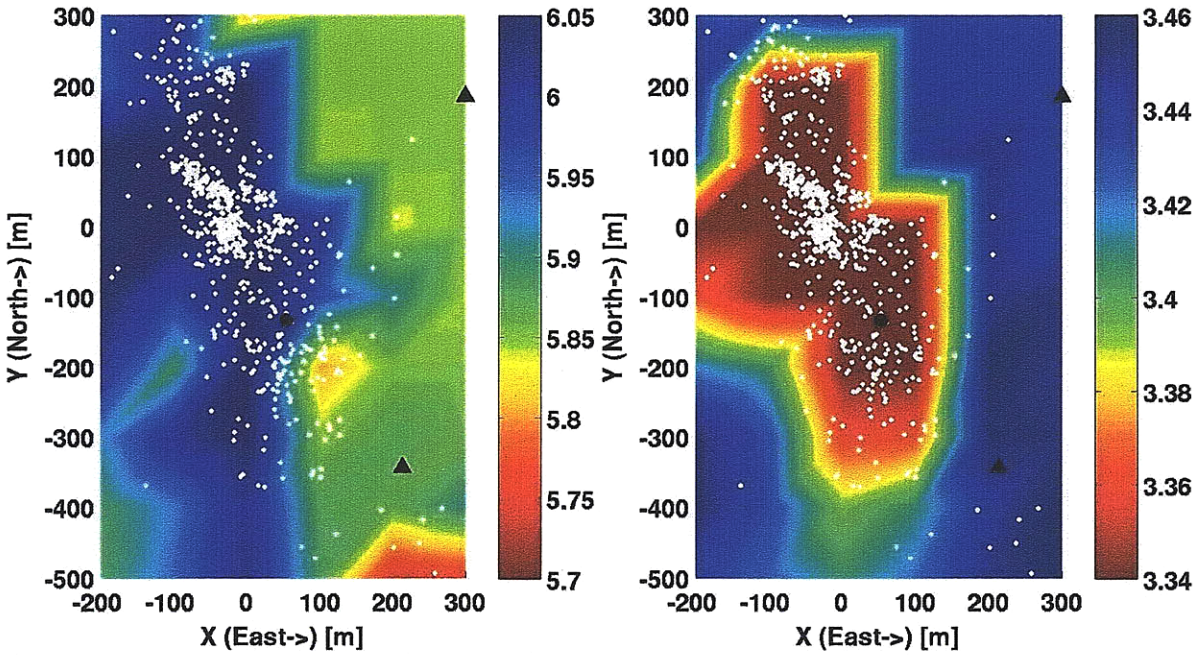

Figure A.47: Horizontal velocity model slices for P and S wave velocities at 3200 meters depth in km/sec. Black circle denotes the position of the injection well GPK1. Black triangles show the locations of station 4550 (upper right) and hyd1 (lower right). White dots denote final earthquake locations within fifty meters depth.

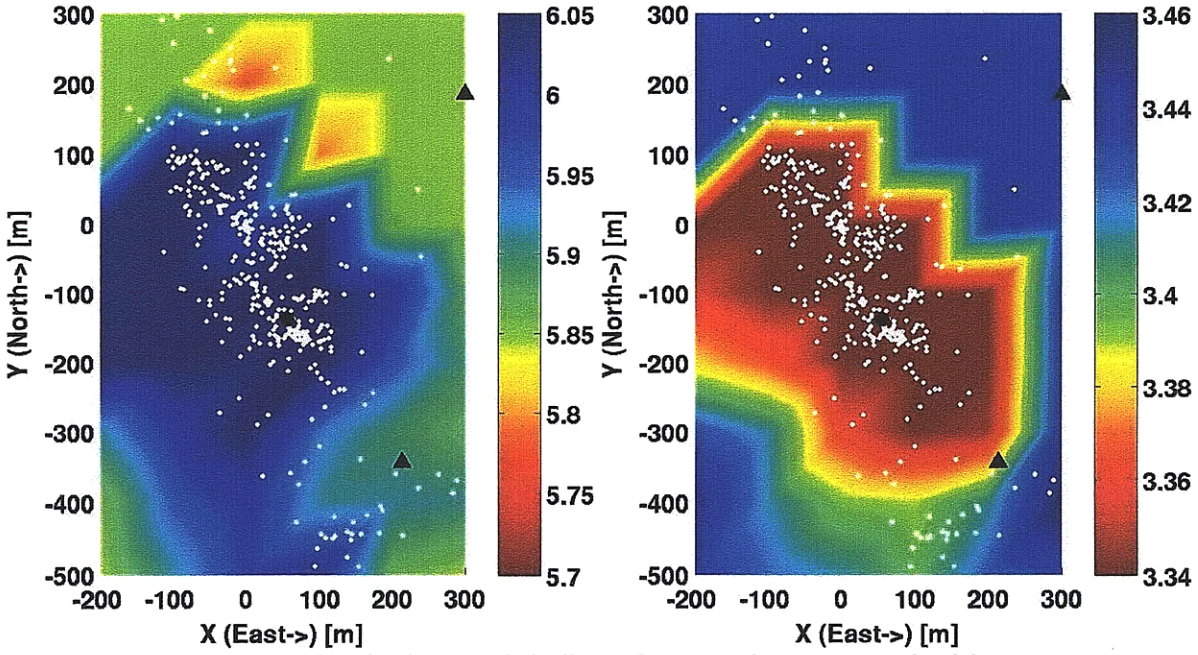

Figure A.48: Horizontal velocity model slices for P and S wave velocities at 3300 meters depth in km/sec. Black circle denotes the position of the injection well GPK1. Black triangles show the locations of station 4550 (upper right) and hyd1 (lower right). White dots denote final earthquake locations within fifty meters depth.

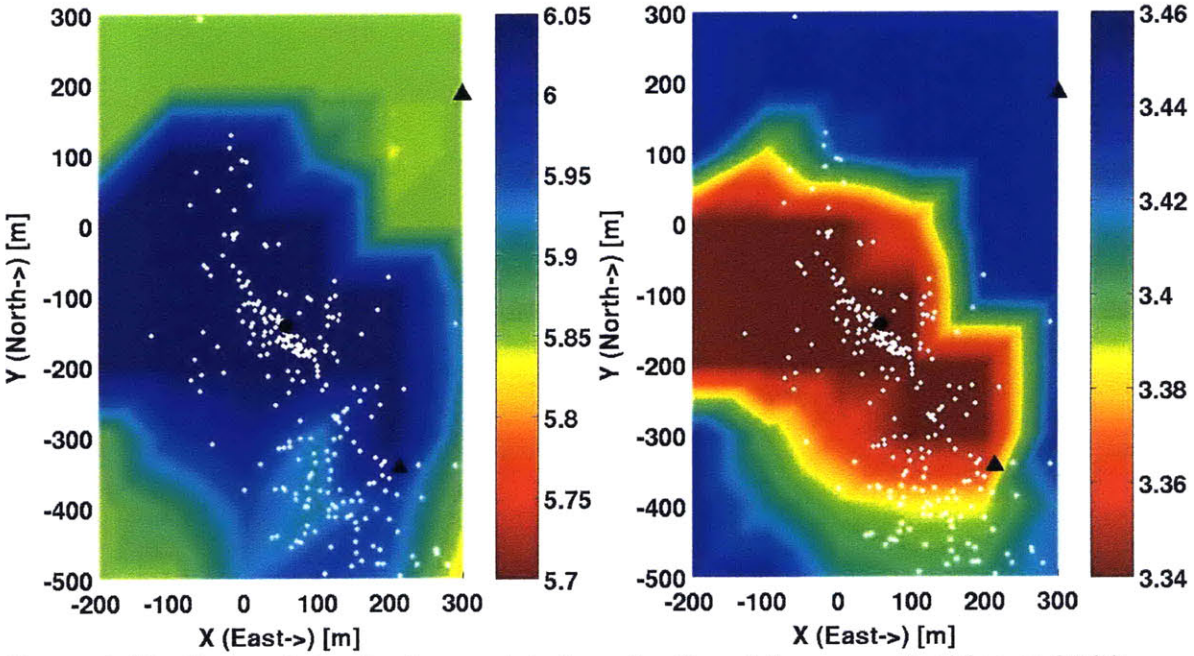

Figure A.49: Horizontal velocity model slices for P and S wave velocities at 3400 meters depth in km/sec. Black circle denotes the position of the injection well GPK1. Black triangles show the locations of station 4550 (upper right) and hyd1 (lower right). White dots denote final earthquake locations within fifty meters depth.

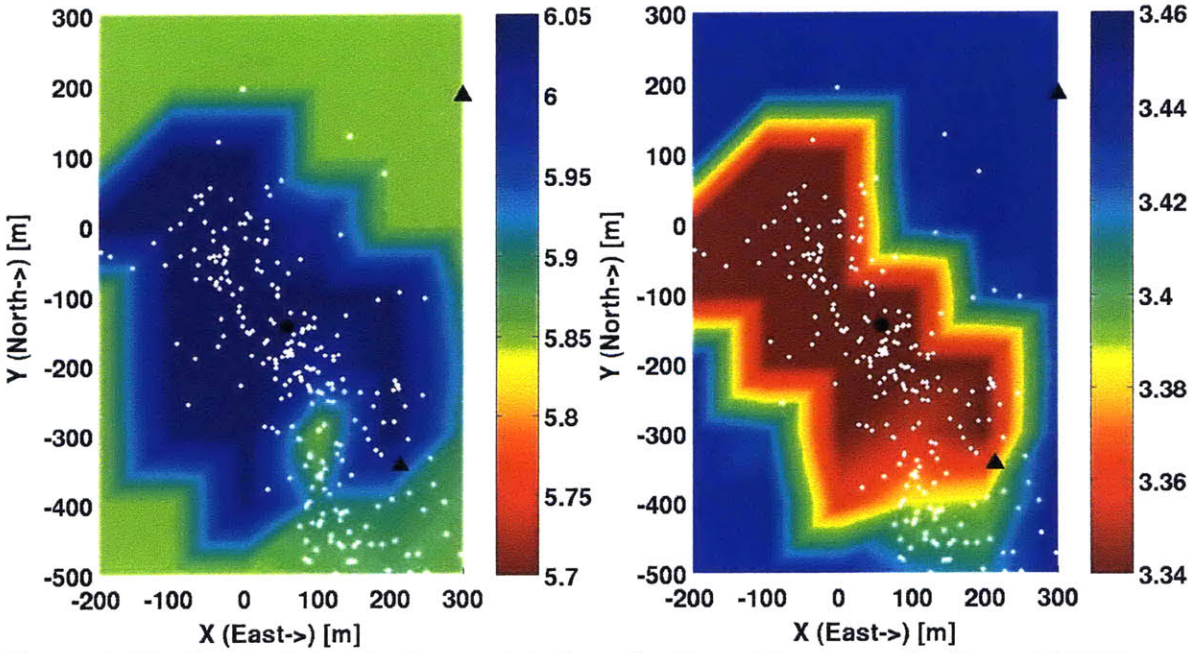

Figure A.50: Horizontal velocity model slices for P and S wave velocities at 3500 meters depth in km/sec. Black circle denotes the position of the injection well GPK1. Black triangles show the locations of station 4550 (upper right) and hyd1 (lower right). White dots denote final earthquake locations within fifty meters depth.

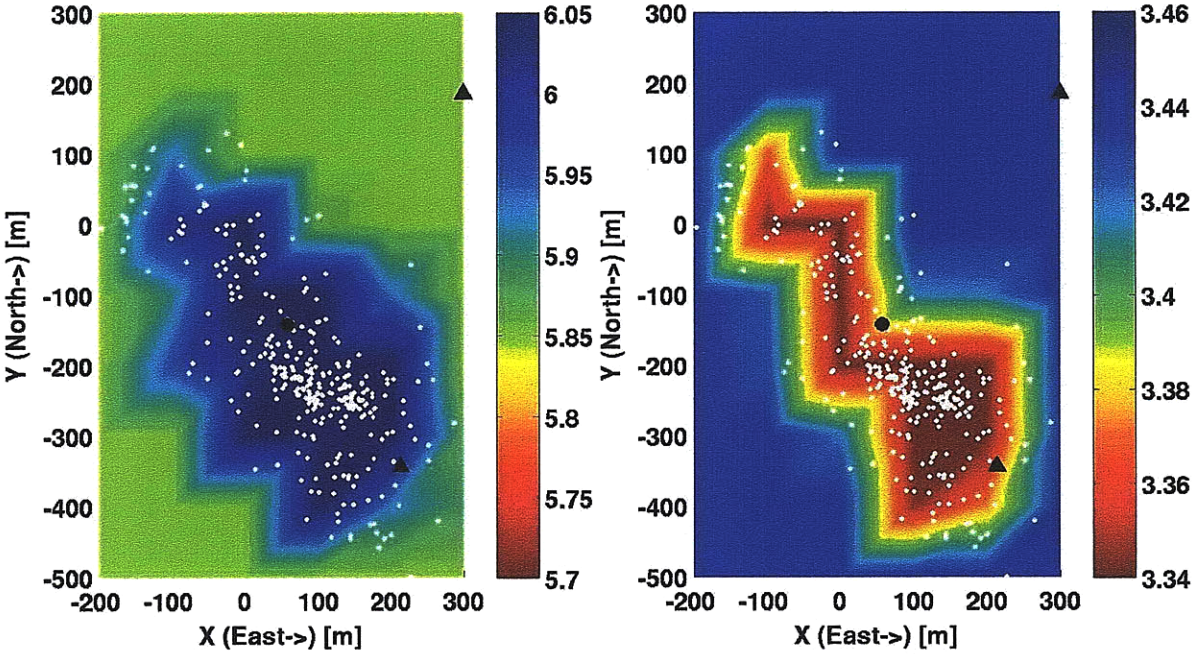

Figure A.51: Horizontal velocity model slices for P and S wave velocities at 3600 meters depth in km/sec. Black circle denotes the position of the injection well GPK1. Black triangles show the locations of station 4550 (upper right) and hyd1 (lower right). White dots denote final earthquake locations within fifty meters depth.

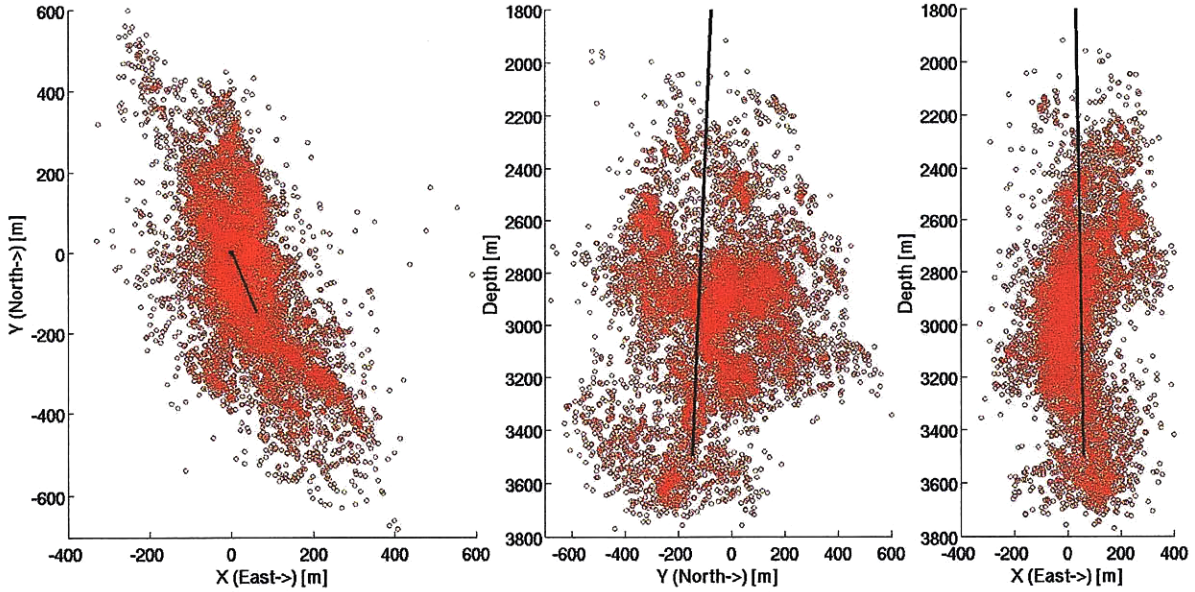

Figure A.52: Final event location plots (Plan View, North-South vs Depth, East-West vs Depth) with the path of GPK1 (black line) into the reservoir.

REFERENCES

Baria, R., J. Baumgartner, A. Gerard, J. Reinhard, and J. Garnish (1999). European HDR research programme at Soultz-sous-Foretz (France) 1987-1996, *Geothermics*, **28**, 655-669.

Butterworth, S. (1930). On the Theory of Filter Amplifiers, *Experimental Wireless & The Wireless Engineer*, **7**, 536–541.

Charlety, J., N. Cuenot, C. Dorbath, and L. Dorbath (2006). Tomographic study of the seismic velocity at the Soultz-sous-Forets EGS/HDR side, *Geothermics*, **35**, 532-543.

Du, W., C. Thurber, and D. Eberhart-Phillips (2004). Earthquake Relocation Using Cross-Correlation Time Delay Estimates Verified with the Bispectrum Method, *Bulletin of the Seismological Society of America*, **94**, 856-866.

Dyer, B. (2000). Soultz GPK2 stimulation June/July 2000. Seismic monitoring. Seismic field report. Semore Seismic.

Dyer, B., A. Jupe, R. H. Jones, T. Thomas, J. Willis-Richards, and P. Jacques (1994). Microseismic Results From The European HDR Geothermal Project, Soultz-sous-forets, Alsace, France - 1993, CSM Associates Ltd., Rosemanowes, Cornwall, U.K., IR03/24.

Evans, K., H. Moriya, H. Niitsuma, R. Jones, S. W. Phillips, A. Genter, J. Sasse, R. Jung, and R. Baria (2005). Microseismicity and Permeability Enhancement of Hydrogeologic Structures During Massive Fluid Injections into Granity at 3 km Depth at the Soultz HDR Site, *Geophysical Journal International*, **160**, 388-412.

Goldstein, P., D. Dodge, M. Firpo, and L. Minner (2003). SAC2000: Signal processing and analysis tools for seismologists and engineers, Invited contribution to The IASPEI International Handbook of Earthquake and Engineering Seismology, Edited by WHK Lee, H. Kanamori, P.C. Jennings, and C. Kisslinger, Academic Press, London.

Jones, R. H., and H. Asanuma (1997). Analysis of the four-component sensor configuration, MTC/NEDO Internal Report, Tohoku University, Sendai, Japan.

Jones, R. H., and R. Stewart (1997). A Method for Determining Significant Structures in a Cloud of Earthquakes, *Journal of Geophysical Research*, **102**, 8245-8254.

McLaughlin, S., A. Stogioglou, and J. Fackrell (1995). Introducing Higher Order Statistics (HOS) for the Detection of Nonlinearities, *UK Nonlinear News*, **2**, http://www.maths.leeds.ac.uk/applied/news.dir/issue2/hos_intro.html.

Nikias, C. L., and R. Pan (1988). Time Delay Estimation in Unknown Gaussian Spatially Correlated Noise, *IEEE Transactions On Accoustics*, **36**, no. 11, 1706-1714.

Paige, C. C., and M. A. Saunders (1982). LSQR: sparse linear equations and least squares problems, *ACM Trans. Math. Softw.*, **8**, no. 2, 195-209.

Rowe, C. A., R. C. Aster, M. C. Fehler, W. S. Phillips, R. H. Jones, and B. Borchers (2002). Using Automated, High-precision Repicking to Improve Delineation of Microseismic Structures at the Soultz Geothermal Reservoir, *Pure appl. Geophys.,* **159**, 563-596.

Toksöz, M. N., C. H. Cheng, and Aytekin Timur (1976). Velocities of Seismic Waves in Porous Rocks, *Geophysics*, **41**, no. 4, 621-645.

Toomey, D. R., and G. R. Foulger (1989). Tomographic inversion of local earthquake data from the Hengill-Grensdalur central volcano complex, Iceland, *J. Geophys. Res.*, **94**, 17497-17510.

Toomey, D. R., S. C. Solomon, and G. M. Purdy (1994). Tomographic imaging of the shallow crustal structure of the East Pacific Rise at 9°0'N, *J. Geophys. Res.*, **99**, no. 24, 135-24, 157.

Um J., and Thurber C. (1987). A fast algorithm for two-point seismic ray tracing, *Bulletin of the Seismological Society of America,* **132**, 972–986.

Waldhauser, F. (2001). HypoDD: a computer program to compute double-difference hypocenter locations, *U.S. Geol. Surv. Open File Report 01-113*.

Waldhauser, F., and W. L. Ellsworth (2000). A double-difference earthquake location algorithm: method and application to the northern Hayward Fault, California, *Bulletin of the Seismological Society of America*, **90**, 1353-1368.

Zhang, H., and Thurber, C. (2003). Double-Difference Tomography: The Method and Its Application to the Hayward Fault, California, *Bulletin of the Seismological Society of America*, **93**, 1875-1889.

Zhang, H., and Thurber, C. (2007). Estimating the model resolution matrix for seismic tomography problems based on Lanczos bidiagonalization with partial reorthogonalization, *Geophys. J. Int.* **170**, 337-345.

Zhang, H., P. Wang, R. D. van der Hilst, M. N. Toksöz, C. Thurber, and L Zhu (2009). Three-dimensional passive seismic waveform imaging around the SAFOD site, California, using the generalized Radon transform, *Geophysical Research Letters*, **36**, L233308.